WESE

WAVE ENERGY
IN SOUTHERN EUROPE

# DELIVERABLE 2.3
# Acoustic Monitoring

This project has been funded by the European Commission under the European Maritime and Fisheries Fund (EMFF), Call for Proposals EASME/EMFF/2017/1.2.1.1 – "Environmental monitoring of wave and tidal devices". This communication reflects only the author's view. EASME is not responsible for any use that may be made of the information it contains.

AZTI MEMBER OF BASQUE RESEARCH & TECHNOLOGY ALLIANCE · WavEC Offshore Renewables · IDOM · BiMEP Biscay Marine Energy Platform · CTN · WAVEROLLER® by AW-Energy · HIDROMOD

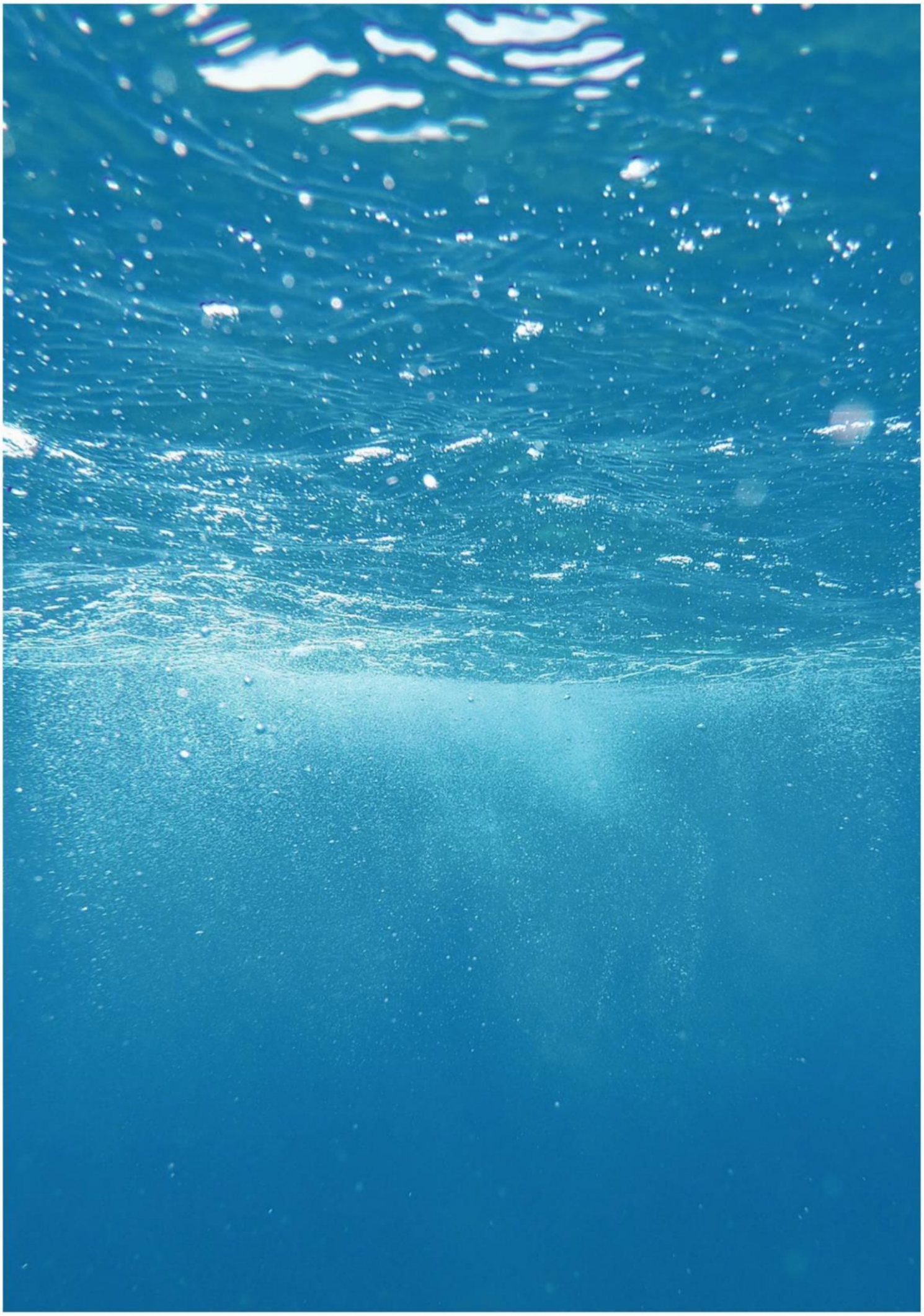

WP 2
Deliverable 2.3 (Acoustic Monitoring)

PROJECT COORDINATOR
AZTI

TASK LEADER
CTN

AUTHORS
Ivan Felis Enguix (CTN)
Eduardo Madrid Navarro (CTN)
Rosa Martínez Álvarez-Castellanos (CTN)
Juan Bald (AZTI)
Ainhize Uriarte (AZTI)
Erica Cruz (WAVEC)

SUBMISSION DATE
30 | November| 2020

CITATION

Felis, I., Madrid, E., Álvarez-Castellanos, R., Bald, J., Uriarte, A., Cruz, E., 2020. Deliverable 2.3 Acoustic Monitoring. Corporate deliverable of the WESE Project funded by the European Commission. Agreement number EASME/EMFF/2017/1.2.1.1/02/SI2.787640. 85 pp.

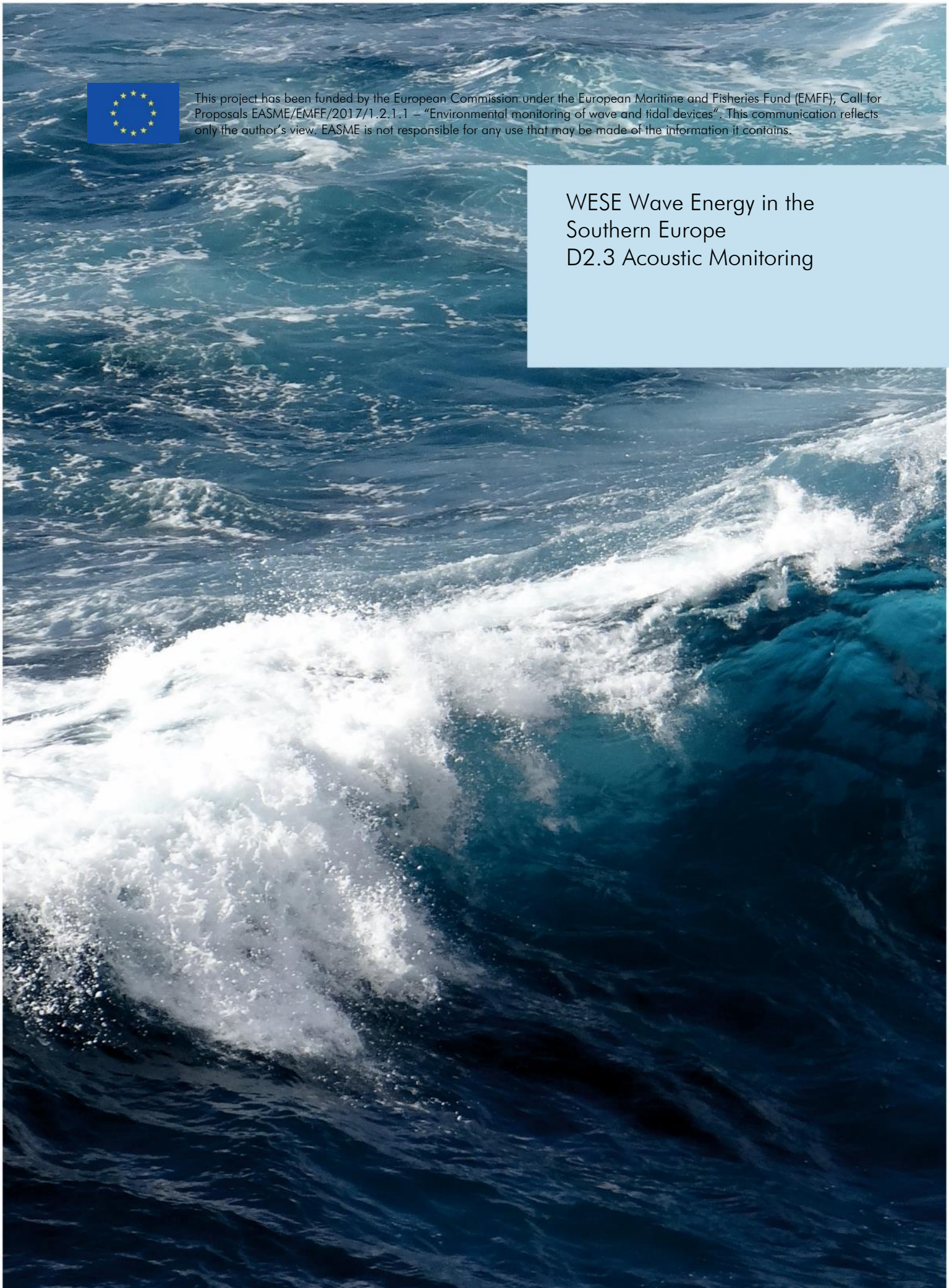

This project has been funded by the European Commission under the European Maritime and Fisheries Fund (EMFF), Call for Proposals EASME/EMFF/2017/1.2.1.1 – "Environmental monitoring of wave and tidal devices". This communication reflects only the author's view. EASME is not responsible for any use that may be made of the information it contains.

# WESE Wave Energy in the Southern Europe
# D2.3 Acoustic Monitoring

# CONTENTS

# 1. WESE project synopsis

The Atlantic seaboard offers a vast marine renewable energy (MRE) resource which is still far from being exploited. These resources include offshore wind, wave and tidal. This industrial activity holds considerable potential for enhancing the diversity of energy sources, reducing greenhouse gas emissions and stimulating and diversifying the economies of coastal communities. Therefore, the ocean energy development is one of the main pillars of the EU Blue Growth strategy. While the technological development of devices is growing fast, their potential environmental effects are not well-known. In a new industry like MRE, and Wave Energy (WE) in particular, there may be interactions between devices and marine organisms or habitats that regulators or stakeholders perceive as risky. In many instances, this perception of risk is due to the high degree of uncertainty that results from a paucity of data collected in the ocean. However, the possibility of real risk to marine organisms or habitats cannot be ignored; the lack of data continues to confound our ability to differentiate between real and perceived risks.

Due to the present and future demand for marine resources and space, human activities in the marine environment are expected to increase, which will produce higher pressures on marine ecosystems, as well as competition and conflicts among marine users. This context still continues to present challenges to permitting/consenting of commercial-scale development. Time-consuming procedures linked to uncertainty about project environmental impacts, the need to consult with numerous stakeholders and potential conflicts with other marine users appear to be the main obstacles to consenting WE projects. These are considered as non-technological barriers that could hinder the future development of WE in EU and Spain and Portugal in particular were, for instance, consenting approaches remain fragmented and sequential. Consequently, and in accordance with the Ocean Energy Strategic Roadmap published in November 2016, the main aim of the project consists of overcoming these non-technological barriers through the following specific objectives:

- Development of environmental monitoring around wave energy converters (WECs) operating at sea, to analyse, share and improve the knowledge of the positive and negative environmental pressures and impacts of these technologies and consequently a better knowledge of real risks.
- The resulting data collection will be used to apply and improve existing modelling tools and contribute to the overall understanding of potential cumulative pressures and impacts of larger scale, and future, wave energy deployments.

- Development of efficient guidance for planning and consenting procedures in Spain and Portugal for WE projects, to better inform decision-makers and managers on environmental real risks and reduce environmental consenting uncertainty of ocean WE introducing the Risk Based Approach suggested by the RiCORE, a Horizon 2020 project, which underline the difficulties for developers with an existing fragmented and sequential consenting approaches in these countries;
- Development and implementation of innovative maritime spatial planning (MSP) Decision Support Tools (DSTs) for Portugal and Spain for site selection of WE projects. The final objective of such tools will be the identification and selection of suitable areas for WE development, as well as to support decision makers and developers during the licensing process. These DSTs will consider previous findings (both environmental and legal, found in RiCORE) and the new knowledge acquired in WESE in order to support the development of the risk-based approach mentioned in iii);
- Development of a Data Sharing Platform that will serve data providers, developers and regulators. This includes the partners of the project. WESE Data Platform will be made of a number of ICT services in order to have: (i) a single web access point to relevant data (either produced within the project or by others); (ii) Generation of OGC compliant requests to access data via command line (advanced users); (iii) a dedicated cloud server to store frequently used data or data that may not fit in existing Data Portals; (iv) synchronized biological data and environmental parameters in order to feed models automatically.

# 2. Executive summary

In the WESE project scope, Work Package 2 aims to collect, process, analyse and share environmental data collected in sites where Wave Energy Converters (WEC) are operating in real sea conditions in Spanish and Portuguese coastal waters, representing different types of technology, sites and, therefore, types of marine environment (onshore, nearshore and offshore) that can potentially be affected by wave energy projects: (i) Idom-Oceantec MARMOK-A-5, installed in the Biscay Marine Energy Platform (BiMEP) in Spain; (ii) Mutriku Wave Power Plant, in operation in the Mutriku (Spain); and (iii) WaveRoller (AW-Energy), installed in Peniche (Portugal).

This specific deliverable presents the results of the task 2.3, that is, the reports of the acoustic monitorization campaigns and, most significant, the characterization of the wave energy converters through analysis of the acquired data by the monitorization plans designed in deliverable D2.1. To this end, acoustic signal processing techniques were applied to the raw audio data gathered from the monitoring campaigns, and mean sound pressure levels were obtained for all third octave frequency bands between 10 and 1000 Hz, taking into account sea state conditions.

In general, the contribution of the devices operation to the ambient soundscape is not very significative. Starting with the MARMOK-A-5 device, the most significative contribution to its surrounding soundscape appears between 40 and 120 Hz, with increments of 14 dB re $\mu$Pa ($H_w < 1$ m), 13 dB re $\mu$Pa ($1\,m \leq H_w < 2\,m$) and 6 dB re $\mu$Pa ($H_w > 2$ m), even though the variability is relevant. Another sources of noise, most relevant with high wave heights, are the mooring chains, which can be perceived at frequencies beyond 2500 Hz, with SPL values approximately ranging from 90 (for lower wave heights) to 105 (higher wave heights) dB re 1 µPa. It should be noted that this metrics have been calculated at a distance of 90 meters away from the converter.

Following with the Mutriku Power Plant, there is no clear indication of an increase in the sound pressure levels when the plant is operating, at least at a distance of 1000 meters away from the central. As it corresponds to a shallow water environment, the lower frequencies are shown to be filtered out, therefore being the higher frequencies those with more acoustic energy. In any case, the higher difference (between background noise and the sound with the plant working) of sound pressure levels is just about 5 dB re 1 µPa, at 80 Hz, below typical deviations.

# 3. Introduction

In this deliverable we present the work carried out in the acoustic monitorization plans (explained in full detail in the previous deliverable D2.1) for the three test sites studied in the WESE project: BiMEP (MARMOK-A-5, offshore oscillating water column WEC), Mutriku (Mutriku, onshore oscillating water column WEC), and Peniche (WaveRoller, off-shore surge WEC).

Noise is defined according to the Marine Strategy Framework Directive (MSFD) as an "anthropogenic sound that has the potential to cause negative impacts on the marine environment, including component biota but not necessarily the whole environment". It is considered one of the main impacts of marine renewable energy converters operation (Boehlert & Gill, 2010), given the acute importance of sound for marine life, especially for cetaceans (Weilgart, 2007).

Given the necessary uprising of renewable energy technologies, in which marine energy promises (despite being still in testing phase of development) to be a solid support to already established technologies (photovoltaic, wind), a good understanding of the impacts associated to these technologies must be achieved (Melikoglu, 2018) (Khan, Kalair, Abas, & Haider, 2017). Among these impacts, we focus here on the acoustics, which is one of the main possible concerning impacts of ocean renewable technologies (Boehlert & Gill, 2010).

It should be noted that WESE focuses on one of the main types of marine energy technology: Wave Energy Converters (WEC); that is, devices that obtain energy from the movement of sea waves, but there are also different types within this group. In fact, WaveRoller is a surge-based WEC, meaning that it exploits the horizontal displacement of water as a consequence of wave dynamics in shallow waters, while MARMOK-A-5 and Mutriku are oscillating water column WEC, so they ultimately rely on the vertical movement of the sea surface to produce energy.

In this study, there are two clear distinct types of monitorization (for every WEC): a spatial monitorization and a temporal monitorization, depending on the number and duration of the measurements. The spatial monitorization has little resolution in time but covers a significant area around the WEC (high resolution in space), while the temporal monitorization has good temporal resolution (e.g., measurements taken during more than one month), with null spatial resolution (single monitoring location). For the sake of completeness, these are briefly reviewed in the following section 4 and more details can be also found in the deliverable 2.1.

Also, as explained in the deliverable D2.1, complementary data were acquired to ensure a good analysis of the acoustic data, such as sea state variables, WEC operation regimes and bathymetry. Visualization and details of all these data is seen in section 5.

The results of the processing can be consulted in section 6, where an analysis for each device is done.

Lastly, in section 7 the main conclusions of this work are presented, some of the limitations are acknowledged, and some suggestions for improvement of future similar studies.

# 4. Monitoring

## 4.1 Spatial monitoring

The spatial acoustic monitorization is based on the "mobile survey vessel" method, in which noise measurements are undertaken in different locations during a short period of time using a vessel. This technique, therefore, may provide the required spatial resolution to assess the acoustic directivity and empirical acoustic propagation loss of the possible noise generated by the WECs. Here, there is a low temporal resolution since it does not allow to measure for long time periods.

### 4.1.1 Equipment

**Hydrophone**: SoundTrap 300HF (by Ocean Instruments) (Figure 1):

- Sampling frequency: 288 kHz.
- Bit depth: 16-bit SAR.
- Preamplification gain: 176 dB (177 for Mutriku).

**Figure 1.** SoundTrap 300HF.

**CTD**: CTD SEABIRD SBE-25 (by Sea-Bird Scientific) (Figure 2): this device allows to sample temperature, salinity, density, concentration, and saturation of $O_2$ and pH in the water column. These data will allow us to calculate the sound speed profile.

**Figure 2.** CTD SEABIRD SBE-25.

### 4.1.2 Methodology

The measurements will be taken in points on concentric circles around the WEC (source) of increasing radii, as following:

1. Position the vessel according to the distribution of the sampling sites indicated in the maps shown of section 4.1.4.
2. Stop the boat engines.
3. Carry out a CTD cast (Figure 3).
4. Deploy the equipment into water.
5. One minute after releasing the equipment, start acquiring data for 5 minutes. Record the absolute position, the start and end time and possible incidents of the measurement.

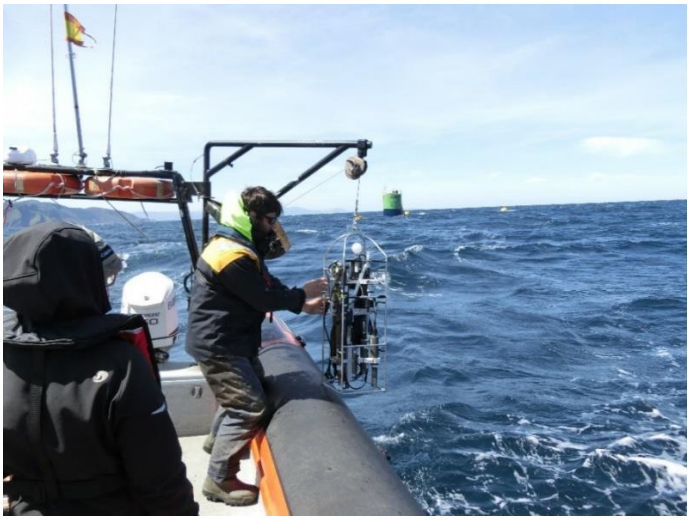

**Figure 3.** Photograph taken from the vessel during the acoustic spatial monitoring of the MARMOK-A-5 OWC, which can be seen in the background.

### 4.1.3 Auxiliary measurements

#### *4.1.3.1 Conductivity, temperature, and depth*

During static measurements, CTD cast will take place before the deployment and after equipment recovery. From the information taken by the CTD (conductivity and temperature), density and sound speed profiles can be calculated using standard equations. In the context of the WESE project, the international standard algorithm, often known as the UNESCO algorithm (Chen and Millero, 1977), will be used[1].

[1] http://resource.npl.co.uk/acoustics/techguides/soundseawater/content.html#UNESCO, accessed on the 01/02/2019.

#### *4.1.3.2 GPS location*

GPS positions should be stated in WGS84, in decimal degrees (minimum of four decimals). GPS locations will be collected before and after each deployment. Before the deployment it will be considered the GPS location at the time the surface yellow buoy is released. After deployment, the GPS location will correspond to the moment that the white surface buoy is collected.

### 4.1.4 Cases

Table 1 and Figure 4 shows the geographic coordinates (WGS84, decimal degrees) of the original sampling points for mobile measurements at the MARMOK-A-5 test site.

**Table 1.** Geographic coordinates (WGS84, decimal degrees) of the original sampling points for mobile measurements at the Marmok-A-5 test site.

| Location ID | Latitude (°) | Longitude (°) |
|---|---|---|
| MA-1 | 43.4694 | -2.8686 |
| MA-2 | 43.4693 | -2.8624 |
| MA-3 | 43.4713 | -2.8672 |
| MA-4 | 43.4757 | -2.8611 |
| MA-5 | 43.4703 | -2.8698 |
| MA-6 | 43.4748 | -2.8698 |
| MA-7 | 43.4964 | -2.8698 |
| MA-8 | 43.4713 | -2.8724 |
| MA-9 | 43.4757 | -2.8785 |

| Location ID | Latitude (°) | Longitude (°) |
|---|---|---|
| MA-10 | 43.4694 | -2.8711 |
| MA-11 | 43.4694 | -2.8772 |
| MA-12 | 43.4674 | -2.8724 |
| MA-13 | 43.4630 | -2.8786 |
| MA-14 | 43.4685 | -2.8698 |
| MA-15 | 43.4640 | -2.8698 |
| MA-16 | 43.4674 | -2.8672 |
| MA-17 | 43.4630 | -2.8611 |

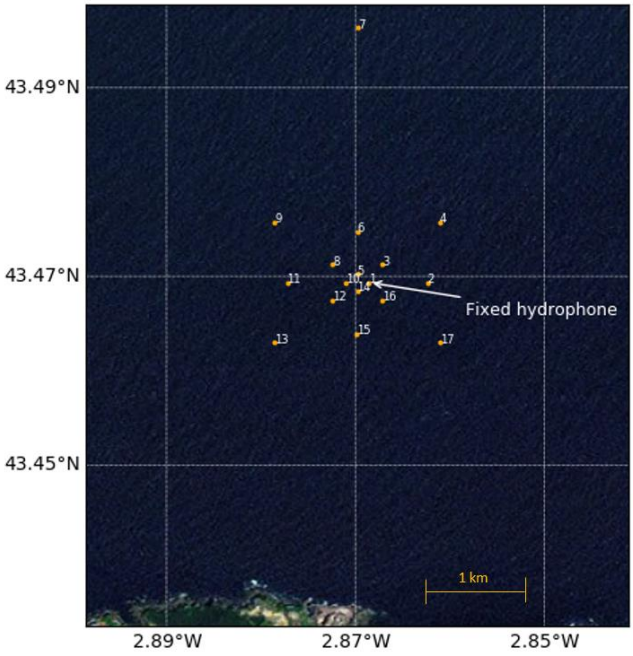


**Figure 4.** Schematic map of sampling sites for MARMOK-A-5.

#### 4.1.4.1 MARMOK-A-5

Due of time considerations, measurements were eventually carried out in 17 sampling stations (instead of the 20 initially proposed in the D2.1 deliverable). All measurements were made at 10 m depth. In this way, it is assured that the measurements are all referenced to the same depth.

The spatial monitorization consisted in two vessel surveys carried out in successive days: 06-05-2019 and 07-05-2019. As shown in Table 2, the sea conditions were very different for each day, with an almost extreme sea state for the first day.

**Table 2.** Sea conditions during the spatial monitorization of MARMOK-A-5.

| Date | $v_{wind}$ (km/h) | Wind direction | Sea state (Beaufort) | $H_w$ | Wave direction |
|---|---|---|---|---|---|
| 06-05-2019 | 51.8 | 90° N | 7 | 1.5 | 80° N |
| 07-05-2019 | 5.5 | 90° N | 1 | 0.5 | 350° N |

For this reason, the eventual monitorization locations for that day were quite different to those initially proposed in Table 1. In fact, a noticeable drift appears in almost every monitoring site, as is deduced from the final and initial coordinates shown in Table 3.

**Table 3.** Mobile monitorization in BiMEP for 06-05-2019. $\varphi$ stands for latitude [°N] and $\lambda$ for longitude [°E] (subindex $i$ denotes "initial", $f$ denotes "final"), while $D_{max}$ and $D_h$ denote maximum depth and hydrophone depth.

| ID | $t_i$ | $t_f$ | $\varphi_i$ | $\lambda_i$ | $\varphi_f$ | $\lambda_f$ | $D_{max}$ [m] | $D_h$ [m] | $T$ [°C] |
|---|---|---|---|---|---|---|---|---|---|
| MA-17 | 10:44 | 10:47 | 43.4630 | -2.8611 | 43.4642 | -2.8676 | 68 | 10 | 16.1 |
| MA-2 | 11:07 | 11:12 | 43.4701 | -2.8624 | 43.4706 | -2.8678 | 76 | 10 | 13.4 |
| MA-4 | 11:21 | 11:26 | 43.4761 | -2.8607 | 43.4766 | -2.8657 | 92 | 10 | 12.0 |
| MA-7 | 11:40 | 11:46 | 43.4963 | -2.8707 | 43.4966 | -2.8751 | 117 | 10 | 11.4 |
| MA-9 | 12:00 | 12:05 | 43.4759 | -2.8793 | 43.4767 | -2.8669 | 92 | 10 | 11.4 |
| MA-6 | 12:18 | 12:23 | 43.4748 | -2.8704 | 43.4749 | -2.8748 | 89 | 10 | 11.5 |
| MA-8 | 12:33 | 12:38 | 43.4713 | -2.8731 | 43.4721 | -2.8777 | 85 | 10 | 11.5 |
| MA-3 | 12:50 | 12:55 | 43.4717 | -2.8674 | 43.4727 | -2.8721 | 84 | 10 | 11.4 |
| MA-5 | 13:03 | 13:08 | 43.4704 | -2.8699 | 43.4717 | -2.8753 | 82 | 10 | 11.5 |
| MA-1 | 13:19 | 13:24 | 43.4699 | -2.8688 | 43.4710 | -2.8735 | 80 | 10 | 11.7 |
| MA-14 | 13:35 | 13:41 | 43.4687 | -2.8698 | 43.4691 | -2.8750 | 79 | 10 | 11.6 |
| MA-10 | 13:50 | 13:55 | 43.4694 | -2.8713 | 43.4703 | -2.8764 | 81 | 10 | 11.6 |
| MA-11 | 14:04 | 14:10 | 43.4694 | -2.8778 | 43.4691 | -2.8821 | 82 | 10 | 11.6 |
| MA-12 | 14:21 | 14:26 | 43.4680 | -2.8736 | 43.4687 | -2.8780 | 80 | 10 | 11.9 |
| MA-16 | 14:38 | 14:48 | 43.4676 | -2.8679 | 43.4669 | -2.8723 | 75 | 10 | 12.2 |
| MA-15 | 14:51 | 14:57 | 43.4641 | -2.8705 | 43.4633 | -2.8749 | 68 | 10 | 11.7 |
| MA-13 | 15:05 | 15:10 | 43.4636 | -2.8798 | 43.4641 | -2.8679 | 71 | 10 | 11.6 |

In the latter day (07-05-2019) was found that the device was under maintenance and, thus, not working (Table 4). For that reason, as soon as the team realized, the monitorization was stopped.

**Table 4.** Mobile monitorization in BiMEP for 07-05-2019.

| ID | $t_i$ | $t_f$ | $\varphi_i$ | $\lambda_i$ | $\varphi_f$ | $\lambda_f$ | $D_{max}$ [m] | $D_h$ [m] | $T$ [ºC] |
|---|---|---|---|---|---|---|---|---|---|
| MA-17 | 09:45 | 09:50 | 43.4631 | -2.8613 | 43.4632 | -2.8627 | 67 | 10 | 18.0 |
| MA-2 | 09:53 | 09:58 | 43.4696 | -2.8628 | 43.4698 | -2.8642 | 78 | 10 | 16.1 |
| MA-4 | 10:00 | 10:05 | 43.4758 | -2.8613 | 43.4762 | -2.8627 | 93 | 10 | 14.3 |
| MA-7 | 10:11 | 10:16 | 43.4694 | -2.8699 | 43.4966 | -2.8709 | 117 | 10 | 13.5 |
| MA-9 | 10:20 | 10:25 | 43.4756 | -2.8788 | 43.4756 | -2.8798 | 93 | 10 | 12.9 |
| MA-6 | 10:28 | 10:33 | 43.4749 | -2.8696 | 43.4751 | -2.8707 | 92 | 10 | 12.7 |
| MA-8 | 12:35 | 10:40 | 43.4712 | -2.8726 | 43.4713 | -2.8739 | 87 | 10 | 12.7 |

### *4.1.4.2 Mutriku*

Similarly to the previous case, because of time considerations, measurements were eventually carried out in 17 sampling stations (instead of the 22 initially proposed) (Table 5 and Figure 5).

Only one day of spatial monitorization was carried out in Mutriku (07-05-2019). The conditions were those of a calmed sea, characterized by a sea state of 2 in the Beaufort scale (Table 6), allowing a safe and precise monitorization.

All related data to the monitorization can be consulted in Table 7, where it can be seen that there is very little to no drift at all.

**Table 5.** Geographic coordinates (WGS84, decimal degrees) of the sampling points for mobile measurements at the Mutriku test site.

| Location ID | Latitude (º) | Longitude (º) |
|---|---|---|
| MT-1 | 43.3122 | -2.3757 |
| MT-2 | 43.3117 | -2.3746 |
| MT-3 | 43.3103 | -2.3715 |
| MT-4 | 43.3131 | -2.3744 |
| MT-5 | 43.3137 | -2.3708 |
| MT-6 | 43.3149 | -2.3648 |
| MT-7 | 43.3139 | -2.3761 |
| MT-8 | 43.3142 | -2.3755 |
| MT-9 | 43.3165 | -2.3737 |

| Location ID | Latitude (º) | Longitude (º) |
|---|---|---|
| MT-10 | 43.3204 | -2.3705 |
| MT-11 | 43.3359 | -2.3580 |
| MT-12 | 43.3144 | -2.3774 |
| MT-13 | 43.3170 | -2.3783 |
| MT-14 | 43.3213 | -2.3799 |
| MT-15 | 43.3131 | -2.3778 |
| MT-16 | 43.3135 | -2.3789 |
| MT-17 | 43.3149 | -2.3821 |

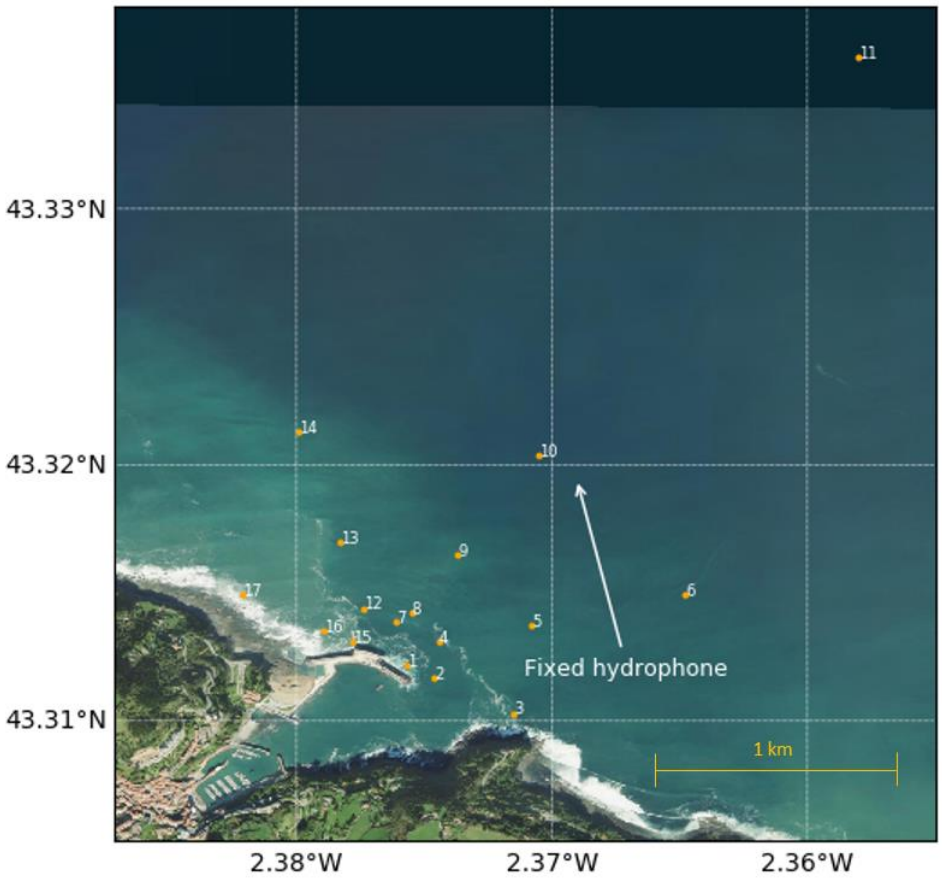


**Figure 5.** Schematic map of sampling sites for the Mutriku campaign.

**Table 6.** Sea conditions during Mutriku campaign.

| Date | $v_{wind}$ (km/h) | Wind direction | Sea state | $H_w$ | Wave direction |
|---|---|---|---|---|---|
| 07-05-2019 | 5 | 0° N | 2 | 0.5 | 0° N |

For this site as well, the default hydrophone depth was set to 10 meters, but this could not be achieved for some locations (e.g., MT-1, MT-16, MT-17…), where the sea depth (denoted as $D_{max}$ in Table 7). In these cases, the hydrophone was set as deep as possible.

**Table 7.** Mobile monitorization in Mutriku for 06-05-2019. $\varphi$ stands for latitude [ºN] and $\lambda$ [ºE] (subindex $i$ denotes "initial", $f$ denotes "final"), while $D_{max}$ and $D_h$ denote maximum depth and hydrophone depth, respectively.

| ID | $t_i$ | $t_f$ | $\varphi_i$ | $\lambda_i$ | $\varphi_f$ | $\lambda_f$ | $D_{max}$ [m] | $D_h$ [m] | $T$[ºC] |
|---|---|---|---|---|---|---|---|---|---|
| MT-2 | 13:08 | 13:13 | 43.3117 | -2.3747 | 43.3114 | -2.3751 | 16 | 10 | 17.8 |
| MT-1 | 13:15 | 13:19 | 43.3121 | -2.3758 | 43.3121 | -2.3761 | 7 | 5 | 17.0 |
| MT-4 | 13:21 | 13:26 | 43.3131 | -2.3743 | 43.3130 | -2.3745 | 9 | 8 | 15.5 |
| MT-7 | 13:27 | 13:32 | 43.1467 | -2.3762 | 43.3133 | -2.3764 | 7 | 4 | 14.6 |
| MT-8 | 13:34 | 13:39 | 43.3143 | -2.3756 | 43.3142 | -2.3756 | 8 | 5 | 14.0 |
| MT-12 | 13:41 | 13:46 | 43.3143 | -2.3775 | 43.3139 | -2.3775 | 6 | 4 | 13.7 |
| MT-15 | 13:47 | 13:52 | 43.3131 | -2.3779 | 43.3129 | -2.3780 | 5 | 2 | 13.5 |
| MT-16 | 13:54 | 13:59 | 43.3136 | -2.3790 | 43.3134 | -2.3794 | 2 | 1 | 13.4 |
| MT-17 | 14:03 | 14:07 | 43.3149 | -2.3821 | 43.3148 | -2.3821 | 1.5 | 1 | 13.5 |
| MT-13 | 14:09 | 14:15 | 43.3170 | -2.3784 | 43.3170 | -2.3786 | 10 | 9 | 13.7 |
| MT-14 | 14:17 | 14:22 | 43.3212 | -2.3801 | 43.3211 | -2.3811 | 18 | 10 | 13.5 |
| MT-10 | 14:24 | 14:29 | 43.3204 | -2.3707 | 43.3205 | -2.3718 | 23 | 10 | 13.3 |
| MT-11 | 14:33 | 14:39 | 43.3359 | -2.3583 | 43.3361 | -2.3596 | 52 | 10 | 13.1 |
| MT-9 | 14:43 | 14:48 | 43.3165 | -2.3736 | 43.3164 | -2.3744 | 13 | 10 | 13.2 |
| MT-6 | 14:50 | 14:56 | 43.3148 | -2.3649 | 43.3148 | -2.3656 | 22 | 10 | 13.1 |
| MT-5 | 14:57 | 15:03 | 43.3137 | -2.3710 | 43.3135 | -2.3718 | 17 | 10 | 13.0 |
| MT-3 | 15:04 | 15:10 | 43.3105 | -2.3714 | 43.3104 | -2.3720 | 7 | 5 | 13.0 |

#### *4.1.4.3 WaveRoller*

Even though monitoring plans were initially planned the COVID outbreak has prevented the implementation of the field works around the AW Energy device. This information will be lately incorporated in an update of the present Deliverable.

## 4.2 Temporal monitorization

This method is based on the deployment of a passive acoustic sensor moored in a specific location for a long time. This way we achieve a high temporal resolution for it allows to register variations due to environmental changes in different cycles of operation of the WEC. This is at the cost of a null spatial resolution. The hydrophone can be set up to register signal periodically during such period of time.

### 4.2.1 Equipment

The same hydrophone, a SoundTrap 300HF was used in the spatial monitorization (one for each device) for this campaign (see section 4.1.1 for additional features).

### 4.2.2 Methodology

A static sampling station was installed close to each of the Mutriku and MARMOK-A-5 devices under study to acquire acoustic data with a good temporal resolution. Since the devices are positioned in shallow waters a bottom mounted system was used. The configuration is different at each test site and according to Figure 6. It is important to notice that in all connecting points for both schemes metal pieces were avoided. The anchor weight and shape were adjusted to the bottom type and the expected drag of the system (shown in Figure 6).


**Figure 6.** Left: hydrophone mooring scheme. Middle: detail of the hydrophone. Right: deployment of the anchor.

During the sampling period the hydrophone will be recording 10 minutes every hour, at a sampling frequency of 288 kHz, from the 7th of May of 2019 to the 18th of June of that same year (that is, continuously for 42 days). The total number of different

signals is a bit higher than 1000 for each station, amounting to a total storage size close to the terabyte of data.

### 4.2.3 Auxiliary measurements

Additionally, we have gathered information during the campaigns of the following auxiliary variables.

#### *4.2.3.1 Sea state*

Time series regarding sea state conditions have been also used to characterize the background ambient noise of the sea. In particular, we focused on significant wave height as the main correlator of noise, as well as wave period. They are further detailed in section 5.2.

#### *4.2.3.2 WEC operation parameters*

Time series of parameters describing the converters working conditions have been obtained from the respective WEC users. These datasets contain important information about the regime of the converters (and are specific to each one). The most relevant parameters for our study are output power and turbines rpm. They are detailed in section 5.3.

#### *4.2.3.3 Meteorologic conditions*

We have also added to the analysis data relative to precipitation as a complementary support parameter to sea state variables. In section 4.2.3.3 these time series are shown. It is stated there the similarity between wave height and precipitation time series, as extreme cases of sea states are often accompanied by storms and rain.

### 4.2.4 Cases

#### *4.2.4.1 MARMOK-A-5*

The static measuring station was at almost 100 m from the device (Table 8). Notice that the static station location approximately matches with one of the mobile locations (MA-1) shown in Figure 4.

**Table 8.** Coordinates (WGS84, decimal degrees) of the moored hydrophone at the BiMEP test site.

| Location ID | Latitude (°) | Longitude (°) | Column water depth (m) | Hydrophone depth |
|---|---|---|---|---|
| MA-1 | 43.4700 | -2.8691 | 78 | 70 |

#### *4.2.4.2 Mutriku*

In the case of Mutriku, because of the larger dimensions of the source (multiples turbines), the static measuring station was installed at 1 km from the centre of the plant, to ensure far-field radiation condition, as can be shown in Figure 5 and Table 9.

**Table 9.** Coordinates (WGS84, decimal degrees) of the moored hydrophone at the Mutriku test site.

| Location ID | Latitude (°) | Longitude (°) | Column water depth (m) | Hydrophone depth |
|---|---|---|---|---|
| MT-9 | 43.3195 | -2.3690 | 21 | 10 |

## 4.3 Airborne monitorization

As a complementary acoustic monitorization, airborne noise measurements were carried out for both MARMOK-A-5 and Mutriku.

### 4.3.1 Equipment

The instrumentation used was a portable system designed by CTN (Figure 7) which integrated all necessary elements to acquire digital acoustic signals.


**Figure 7.** Left: Airborne acoustic monitoring system. Right: photograph of the microphone inside Mutriku Power Plant.

### 4.3.2 Methodology

This campaign was carried out in parallel with the spatial monitoring campaign, to be able to compare between both types (airborne, underwater) of noise recordings. These measurements were acquired, during a time interval of two days, 6$^{th}$ and 7$^{th}$ of May 2019.

### 4.3.3 Cases

#### *4.3.3.1 MARMOK-A-5*

In the case of MARMOK-A-5, the airborne monitoring was made on board the vessel. However, the harsh meteorologic conditions had made the analysis of the acquired signals quite irrelevant, as the amount of extraneous noise present in the recordings was very high. For that reason, there are no further results concerning this case.

#### *4.3.3.2 Mutriku*

The methodology differs here in the fact that the airborne monitorization was carried out inside the chambers of the Mutriku power plant (see Figure 7, right), in parallel to those of the vessel, as a means of validating the underwater acoustic signatures acquired by the latter.

# 5. Collected data

## 5.1 Acoustic data

Acquired data by the hydrophone must be converted to pressure units to be physically relevant, as indicated in Figure 8.

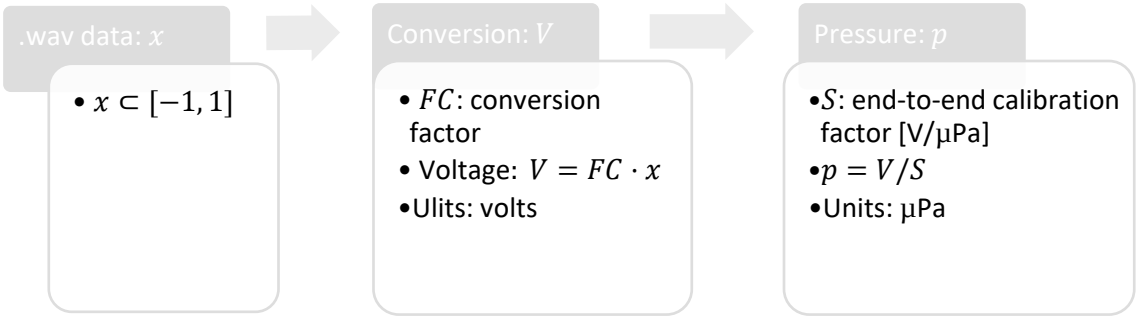


**Figure 8.** Conversion from raw .wav format data (as acquired by the sound card of the hydrophone) to pressure data.

In contrast to traditional hydrophone systems, with SoundTraps there is no need to be concerned with sensitivity in voltage terms, because they integrate the recorder and hydrophone in a single package, there is a fixed relationship between sound pressure and the resultant .wav file data, thereby simplifying calibration and eliminating the need for voltage calculations.

This procedure is used in the signals acquired in both kind of campaigns (temporal and spatial) to obtain the correct units of pressure for the subsequent analysis of the acoustic measurements.

### 5.1.1 MARMOK-A-5

#### *5.1.1.1 Temporal monitorization*

For the case of the BiMEP test site, we have two sets of acoustic data with temporal resolution at our disposal: the one obtained by means of the monitoring campaign discussed previously, and previous data dating from 2012, before the deployment of any of the components of the device. In the other hand, acoustic data from the spatial monitoring is also available. In the following sections these datasets will be detailed.

**WESE campaign data**

After having analysed the acoustic data, we eventually consider 1032 .wav files, corresponding to intervals of 10 minutes acquired hourly starting from the 08:34:09

GTM +02:00 at 07-05-2019, and thus ending at 07:34:09 GTM +02:00 at 19-06-2019.

In Figure 9 and 10 we can see the shape of a typical signal as recorded by the fixed hydrophone in BiMEP. It is expected to encounter high enough variability in the sea conditions during these 40+ days to characterize the converter in different regimes, as it will be shown in Section 5.2.

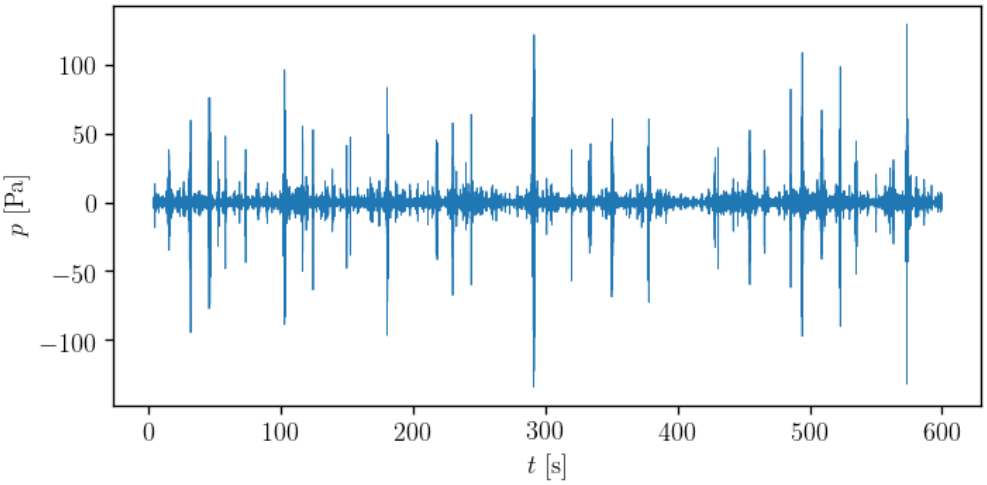


**Figure 9.** Typical acoustic signal once converted to appropriate units.

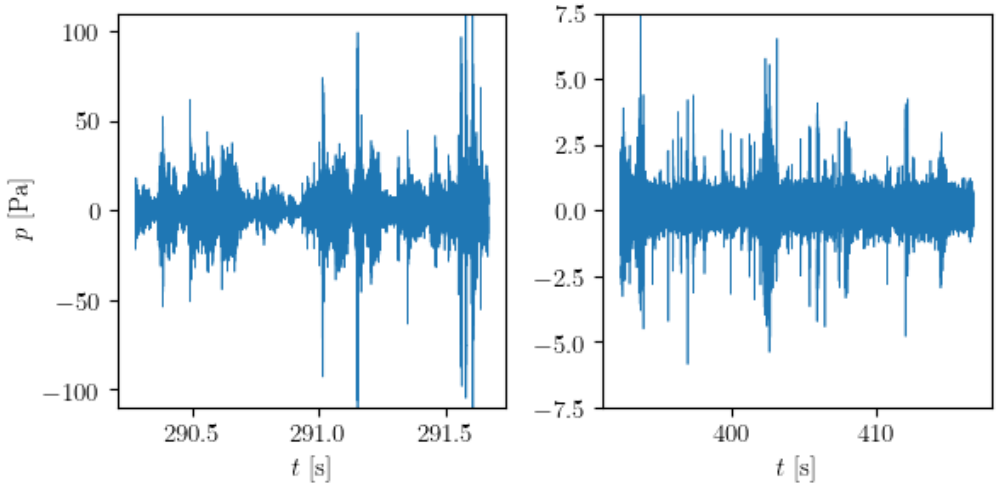


**Figure 10.** Detail of the acoustic signal. Left:high peak-to-peak portion. Right: low peak-to-peak portion.

## Previous data

During the pre-operational phase in 2012, a sonobuoy designed by Universidad Politécnica de Cataluña was moored at 40 m depth. It was able to detect and classify automatically all the acoustic events above the ambient noise (presence of cetaceans

and noise) and store the information. It was moored on the 6 of June 2012 and for 5 months the presence of marine mammals and underwater ambient noise was monitored and later analysed for 1/3 octave bands 63 Hz and 125 Hz as recommended by the Marine Strategy Framework Directive (MSFD, 2008). The mean value recorded during the sampling period for the 1/3 octave bands of 63 Hz and 125 Hz was about 90 dB re 1 µPa and 85 dB re 1 µPa, respectively.

These levels (for one month) are shown in Figure 11. Although not directly comparable, these values can serve us well in the assessment of whether sound levels are higher or not after deployment of the device.

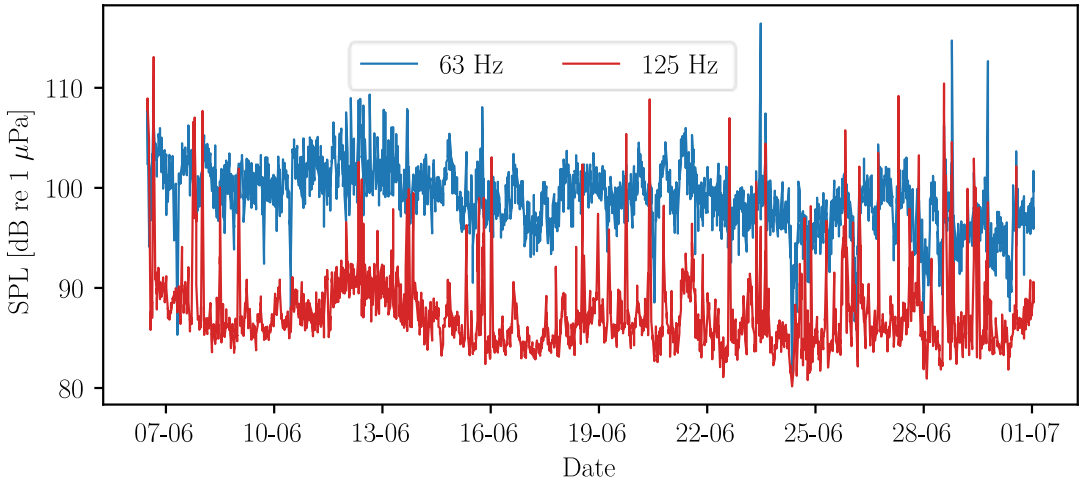


**Figure 11.** SPL values in the 1/3 octave bands of 63 and 125 Hz in the BiMEP test site during June of year 2012.

According to how usual ambient noise sound pressure level curves behave (Urick, 1983), the 63 Hz curve has a mean value higher (about 10 dB) than the one of 125 Hz, which is coherent with the results of this 2012 campaign.

#### *5.1.1.2 Spatial monitorization*

Acoustic data from the spatial monitoring campaign consisted of 17 *.wav files for the 06-05-2019 and 7 *.wav files for the 07-05-2019, of 5 minutes each, sampled at the locations described in the section 4.1.4.1.

### 5.1.2 Mutriku

#### *5.1.2.1 Temporal monitorization*

In the case of Mutriku, we do not have at our disposal more acoustic data than that acquired in the WESE campaigns, although earlier acoustic characterizations have

been studied; in particular, a study from 2017 carried out by AZTI and CTN concluded that there was no evidence of impulsive neither continuous sound emission coming from the OWC Plant of Mutriku (Bald, Uriarte, Ruiz, Cervantes, & Ortega, 2017).

The definitive campaign data consist of 1021 *.wav files, corresponding to hourly acquired intervals of 10 minutes starting from the 11:00:21 GTM+02:00 at 07-05-2019, and thus ending at 23:00:21 GTM+02:00 at 18-06-2019.

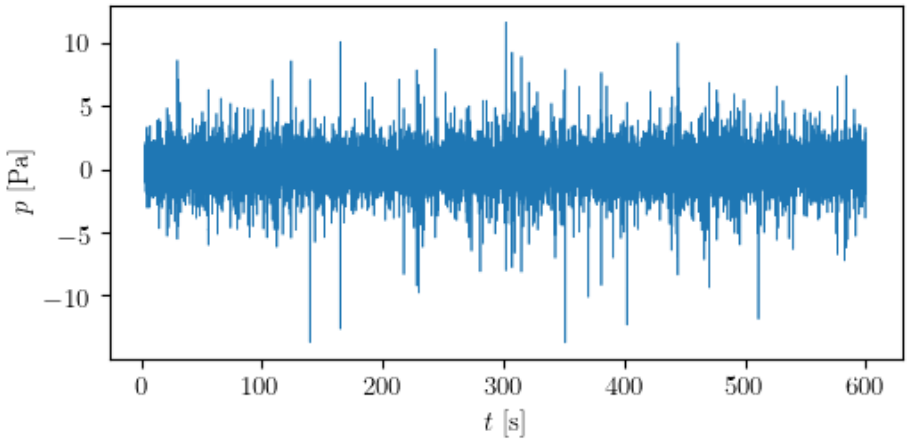


**Figure 12.** Typical acoustic signal once converted to appropriate units from the Mutriku temporal monitorization.

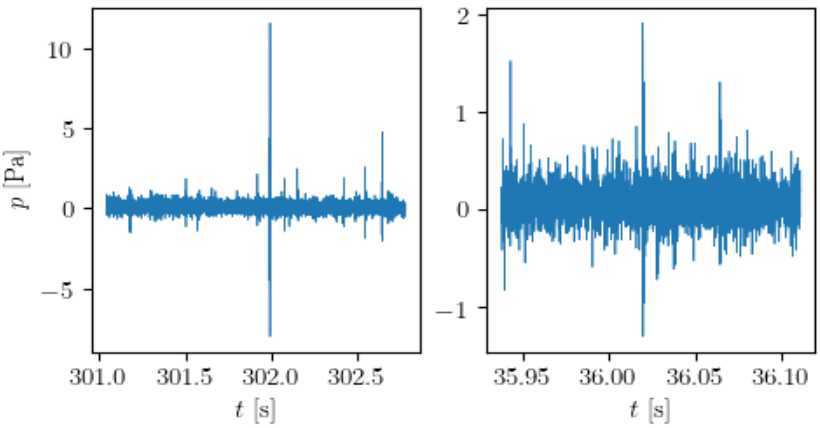


**Figure 13.** Detail of the acoustic signal. Left:high peak-to-peak. Right: low peak-to-peak.

### *5.1.2.2 Spatial monitorization*

In the other hand, acoustic data from the spatial acoustic monitorization in Mutriku consisted in 17 *.wav files sampled by the indications of the section 4.2.4.2, during the 07-05-2019. Their analysis is presented in section 6.3.2.

## 5.2 Sea state data

We gathered data characterizing sea state conditions (i.e. significant wave height and wave period) with the purpose of obtaining useful correlations to assess the intrinsic

acoustic signature of the converter. From these two parameters, we expect significant wave height to be of most importance since it is the main driver of power generation in the OWC technology (MARMOK-A-5 and Mutriku). It will allow us to characterize the background noise (when the device is not working) as a function of wave height and frequency.

### 5.2.1 MARMOK-A-5

Regarding these variables, they come from two different sources for the case of MARMOK-A-5: (i) From the BiMEP data platform; (ii) From a Triaxys wave buoy from IDOM.

As we can see in the Figure 14, the time series correspond between themselves almost perfectly for the wave height variable, but not so for wave period. In any case, we eventually chose to use exclusively the data from the Triaxys wave buoy, as it was sampled exactly at the same times as the acoustic recordings from the temporal monitoring campaign and also present better temporal resolution.

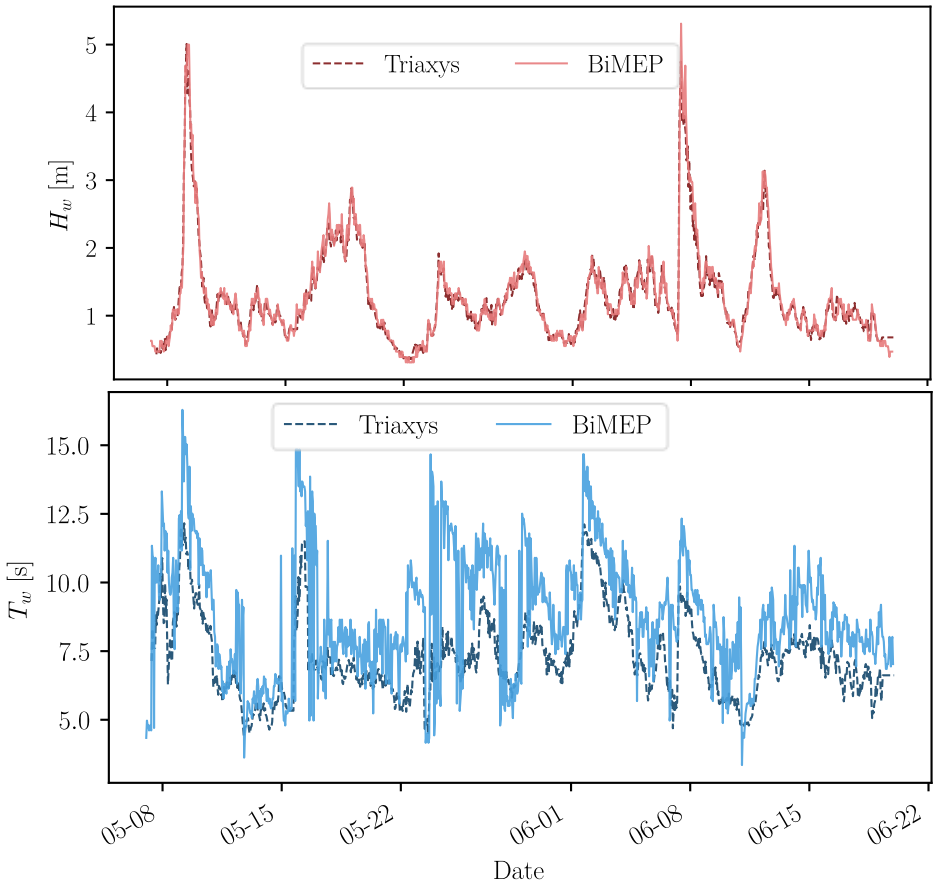


**Figure 14.** Significant wave height and wave period during the temporal monitorization in the MARMOK-A-5 site.

### 5.2.2 Mutriku

Our only dataset of significant wave height was provided by Pasaia's AZTI station (see 28). Wave period was missing, although in any case, as expected and indeed demonstrated in section 6.2.1.1 for the case of MARMOK-A-5, it carried little to no information regarding correlations with SPL or WEC power.

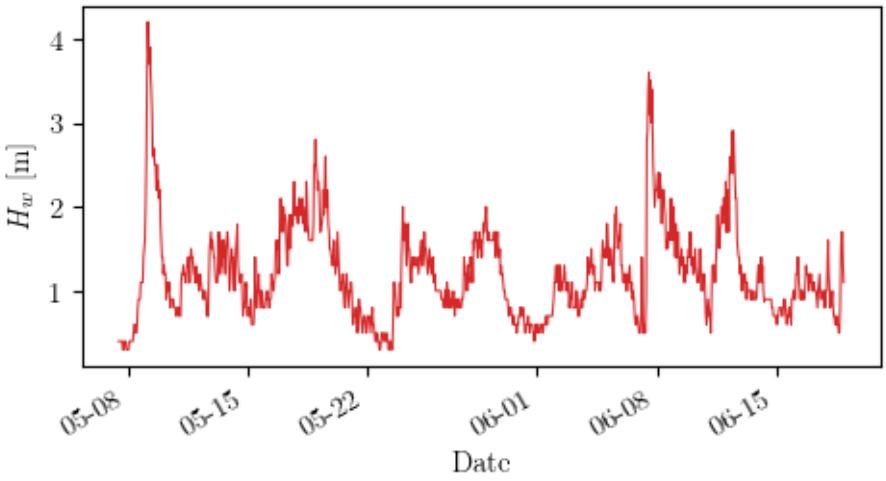


**Figure 15.** Significant wave height during the temporal monitorization in the Mutriku OWC Plant site.

Given its proximity to the BiMEP test site, both significant wave height time series are quite similar, although in the case of Mutriku the maximum values are smaller (by one unit).

## 5.3 WEC operation

The last essential parameter consists of some measure of the power generated by the WECs. This information will let us classify all the other data into two groups: "WEC off" and "WEC on" (e.g., instants of time when the device was not operating and inversely, respectively), which, eventually, will discern the difference in sound levels for both scenarios. In the following sections, datasets of these variables matching the period of temporal monitoring are presented and explained.

### 5.3.1 MARMOK-A-5

For the case of MARMOK-A-5, data of the WEC regime of operation (power, $P$, and revolutions per minute, $\Omega$) during the acoustic temporal monitorization period was gathered. In this case, these variables come binned and normalized in a scale from 0 (minimum value) to 5 (maximum value), as can be seen in the Figure 16.

As mentioned before, for posterior analysis of acoustical recordings, we identify the times when the device was in the lowest activity regime[2], which we define as states with $\Omega < 0.1$; these timestamps will identify the instants when the MARMOK-A-5 turbines were effectively stopped (in grey in Figure 16).

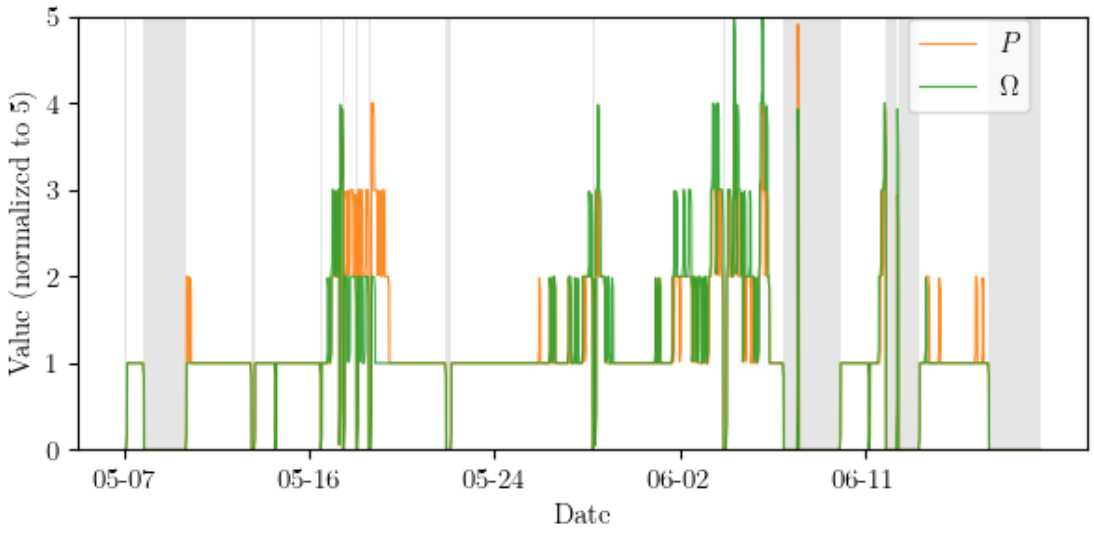


**Figure 16.** Turbine operation variables of MARMOK-A-5. In grey are the "off" time intervals.

Although most of the time the converter was operating, these off time periods consist of a decent number of different sub-signals (10858). Most importantly, there was enough variability in sea states to characterize the background noise in different scenarios.

Figure 17 and Figure 18 show that most states are characterized by low power output and angular velocity, and wave heights lower than 2 meters.

Naturally, as the turbine variables are rounded to the integer, there is a lot of overlap between points; in this case, the opacity of such overlaps indicates the prevalence of the corresponding states.

[2] Even though the original power time series were normalized and binned to integers from 0 to 5, small deviations are found after the necessary interpolation to match the timestamps of every time series. This is the reason we are not using the condition $\Omega = 0$.

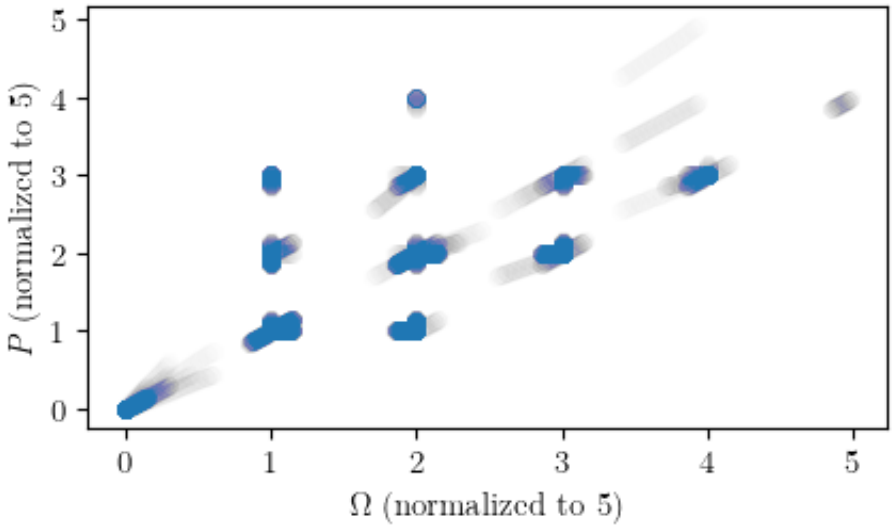


Figure 17. Scatter plot of $P$-Ω for MARMOK-A-5.

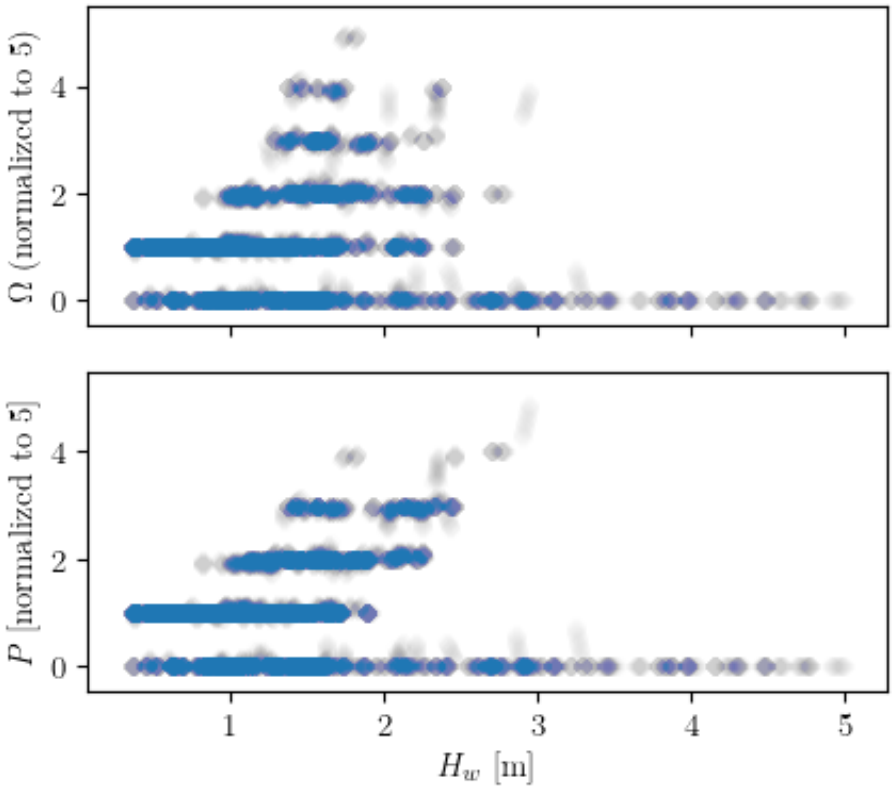


Figure 18. Scatter plots of $P$-$H_w$ and Ω-$H_w$.

### 5.3.2 Mutriku

Detailed WEC operation data during the time period of the temporal monitorization was given by the Basque administration (EVE): power (kW), rpm, valve angle[3] and pressure in chamber (Pa), for every turbine in the plant, with a resolution of 1 second. Although in the period of this study there were 13 installed turbines in the plant, only 11 were functioning, and usually not for the whole temporal monitoring interval, as can be seen in the Figure 19. Besides, there is a noticeable gap in the time series that corresponds to a blackout occurred the 8th and 9th of June, in which none of the turbines were operating.

The electric power is usually negative (that is, the turbines generate energy), but there are times in which it is positive; this occurs when wave activity is so low that efficient operation is unachievable, so the turbines are forced to work as motors, consuming energy and rotating at a fixed rate of 180 rpm.

In Figure 20, the turbine parameters time series are displayed for every turbine of the Mutriku facility (in different colours). The blackout is visible (technically, not visible, as a gap) in every series, as well as the prevalent states of the turbines. Most of the time the turbines generate power in the interval ranging from $-0.5$ to $-5$ kW. The valves are usually open, although some moments in which they are closed can be detected, which also correspond to times when the angular velocity is fixed to $180$ rpm and the power is positive.

As already mentioned, a key part of the acoustic characterization is the identification of non-working regimes of operation intervals of time. In this regard, the case of Mutriku is more complex than the others because we must consider 11 turbines (possibly) working simultaneously. We again focus on the angular velocity $\Omega$ (rpm) variable (most representative of the actual rotation of the machines, which ultimately drives sound generation, and mark 200 rpm as the delimiting value separating non-working and working regimes. Because of the heterogeneous behaviour of the turbines, we find that apart from the aforementioned blackout, there was only another interval of time in which no turbine was working (highlighted dark grey shaded bands in Figure 19). That will mark the times corresponding to background noise (as in no significant sound from the converters is generated).

[3] Valve can be in between 0° (completely closed) and 90° (completely open).

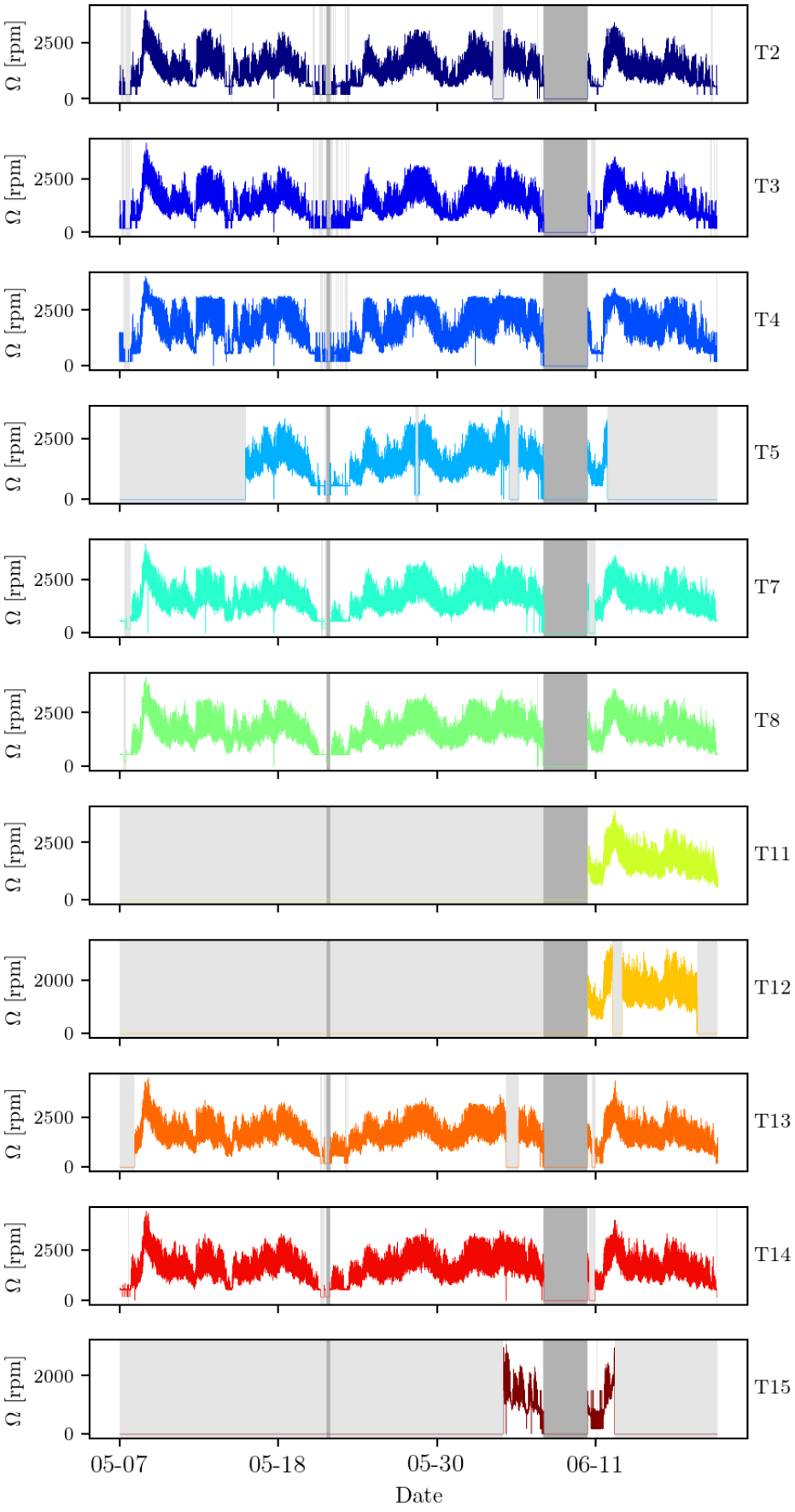


Figure 19. Angular velocity time series for each turbine. In grey $\Omega < 200$ rpm are highlighted; in a darker shade, the time intervals in which every turbine satisfied the $\Omega < 200$ rpm condition.

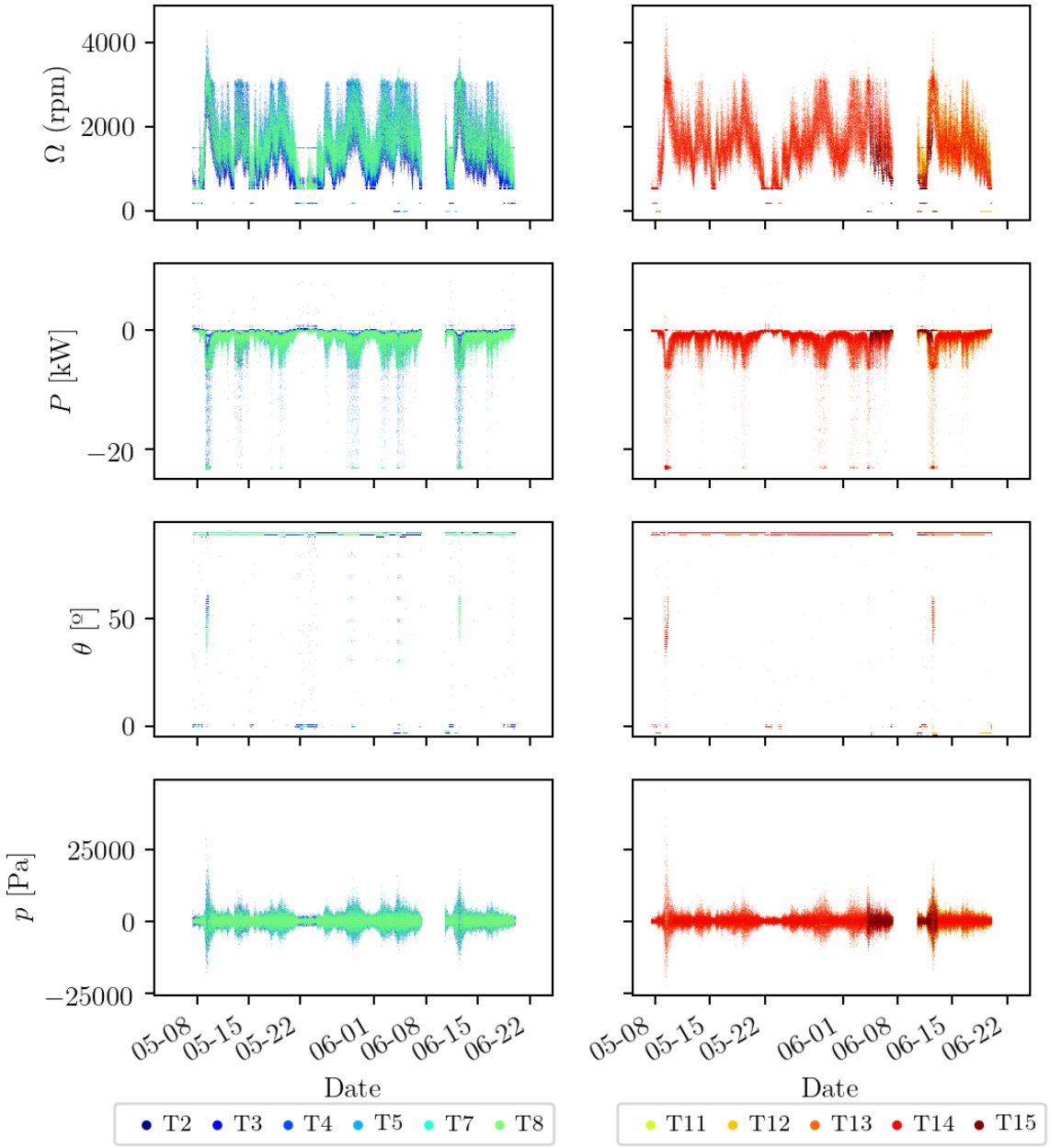


**Figure 20.** Time series of angular velocity $\Omega$, power $P$, valve angle $\theta$ and pressure in the chamber $p$, for all turbines during the temporal monitorization.

In Figure 19 all $\Omega$ time series are presented. From the 11 turbines, 8 were working during practically all the time, with the remaining three (T11, T12, T15) shut off for almost the whole monitorization.

At last, we add some scatter plots for all turbines. In the Figure 21, the dependency of power versus angular velocity is shown, which show great correlation, while in Figure 22 the relation of $\Omega$ and $P$ with $H_w$ is detailed. Note that one of the turbines (T4)

clearly showed a different behaviour than the others, with almost no output generation until reaching 3000 rpm.

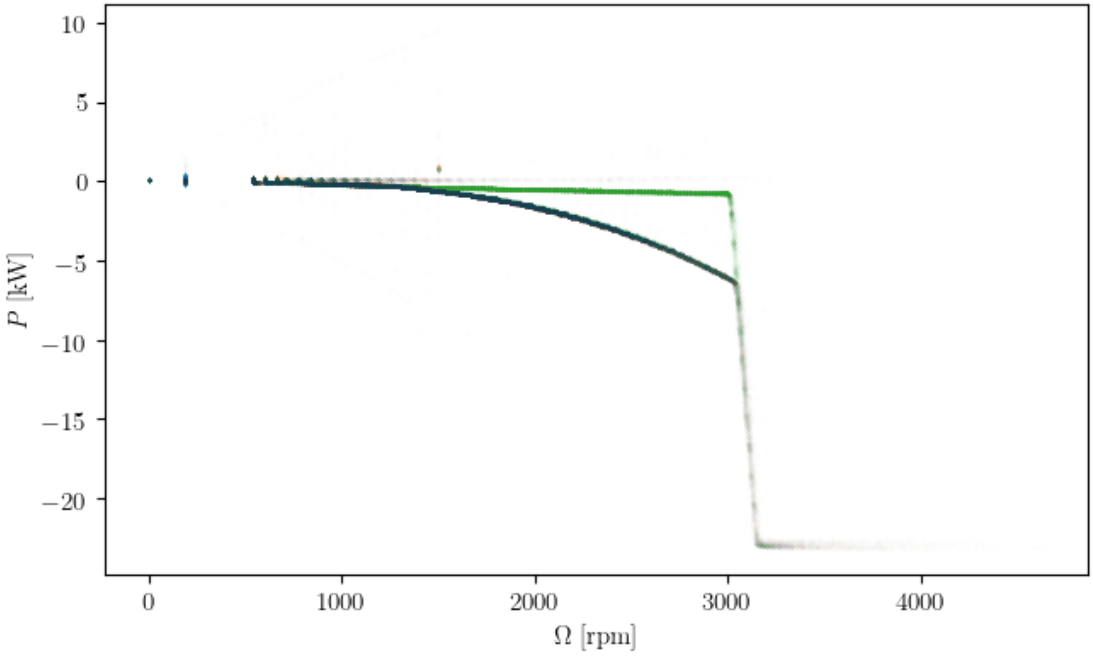


Figure 21. Power of all Mutriku turbines.

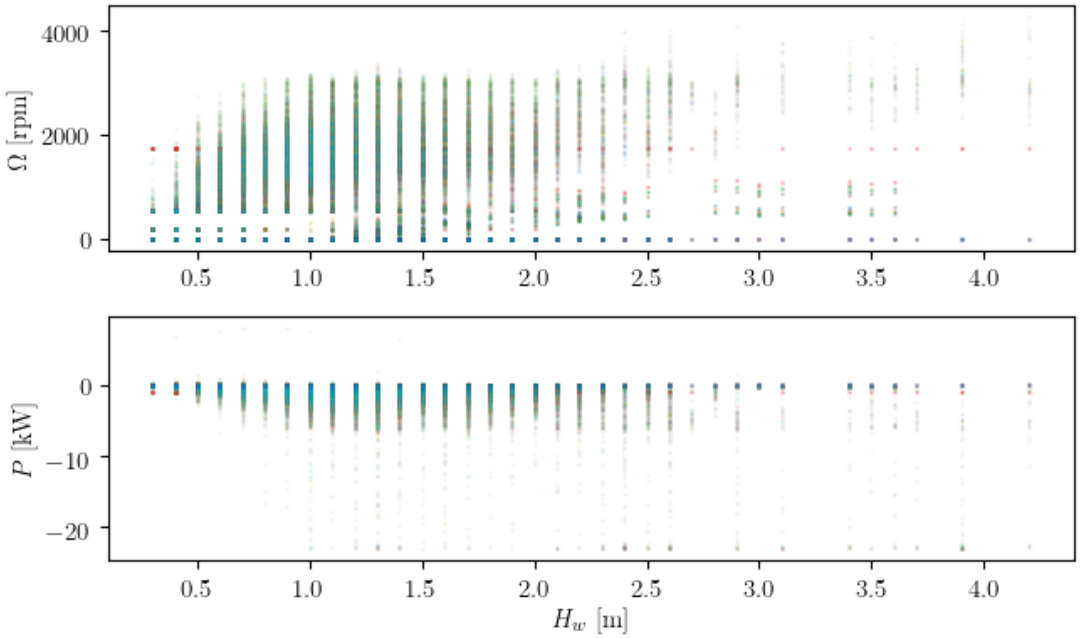


Figure 22. Scatter plots of $\Omega$-$H_w$ and $P$-$H_w$ for all Mutriku turbines.

## 5.4 Precipitation

Time series of precipitation were obtained from the AEMET OpenData service[4] during the interval of temporal monitorization.

### 5.4.1 MARMOK-A-5

In the case of MARMOK-A-5, the dataset was obtained from the Punta Galea meteorologic station, located at around 15 km southwest from the MARMOK-A-5 converter (Figure 23).

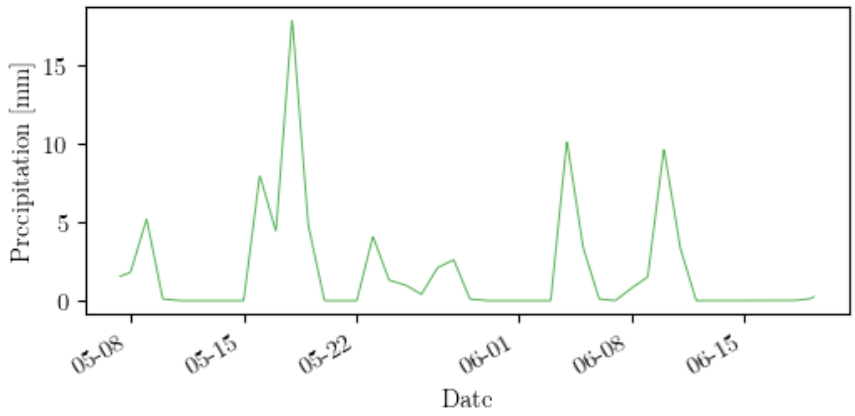


**Figure 23.** Precipitation registered for the MARMOK-A-5 temporal monitoring campaign.

### 5.4.2 Mutriku

As for Mutriku, the data comes from the Machicaco meteorologic station, which is located at 30 km northwest from the Mutriku power plant (Figure 24).

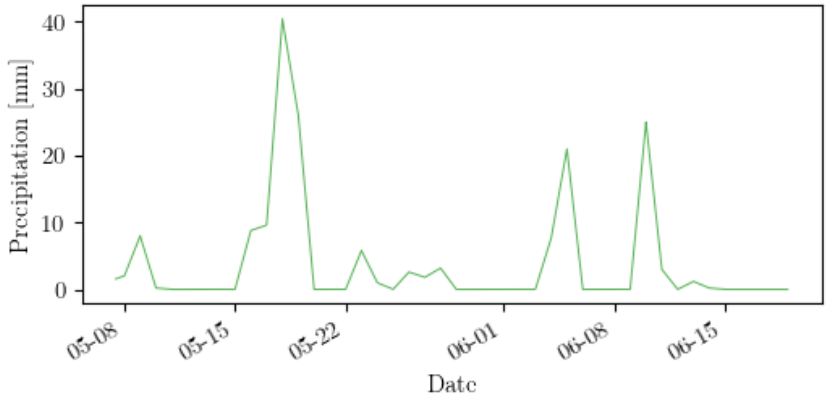


**Figure 24.** Precipitation registered for the Mutriku temporal monitoring campaign.

[4] Link: http://www.aemet.es/es/datos_abiertos.

As it can be seen in both figures, the precipitation time series are very similar in shape for the two cases, as is not surprising. Moreover, the similarity with the wave height graphs is noticeable (see Figure 14 and Figure 15).

# 6. Processed data

Having introduced the datasets we are going to work with, in this section the results of the acoustic processing are presented for every energy converter and type of campaign.

As expressed previously, our goal is to acoustically characterize the operation of the energy converters. The main metric used in this study is the Sound Pressure Level (SPL) measure, which shall be defined shortly. The fundamental problem of the acoustic characterization of in-situ devices is the existence of highly (uncontrollable) variable background noise levels. This makes the exact acoustic characterization of the devices a complex matter. Our approach consisted in classifying the acoustic signals according to the WECs operation regime (on and off), as well as to sea state conditions. This way it is possible to detect changes in SPL values relative to the operation regime.

## 6.1 Methodology

The SPL is defined as:

$$\mathrm{SPL} = 20 \log\left(\frac{p_{rms}}{p_{ref}}\right)$$

where $p_{rms}$ is the root mean square of the pressure in some chosen interval of time and $p_{ref}$ is a reference pressure (in water, $p_{ref} = 1$ µPa). The resulting SPL will slightly depend on such interval, that we will henceforth denote by $\Delta t$, and will be equal to 10 seconds in this study. Given a pressure signal in the appropriate units, the processing scheme consists in the following steps (see Figure 25):

1. Truncate the signal to avoid artifacts at its beginning and end. The exact truncation will depend on the campaign (mobile monitoring campaign recordings are shorter – 5 minutes). We also decimate the signal by a factor of 10. This way, we alleviate the computation significantly while ensuring we are working safely below the Nyquist limit frequency.
2. Apply a bandwidth Butterworth filter to the signal in 1/3 centred octave bands, ranging from 10 Hz to 10 kHz (31 different bands), and discard the origin and ending parts of it, to avoid filtering artifacts.
3. Divide the signal in chunks of $\Delta t$ seconds.
4. Calculate SPL of the individual sub-signals (for each frequency).

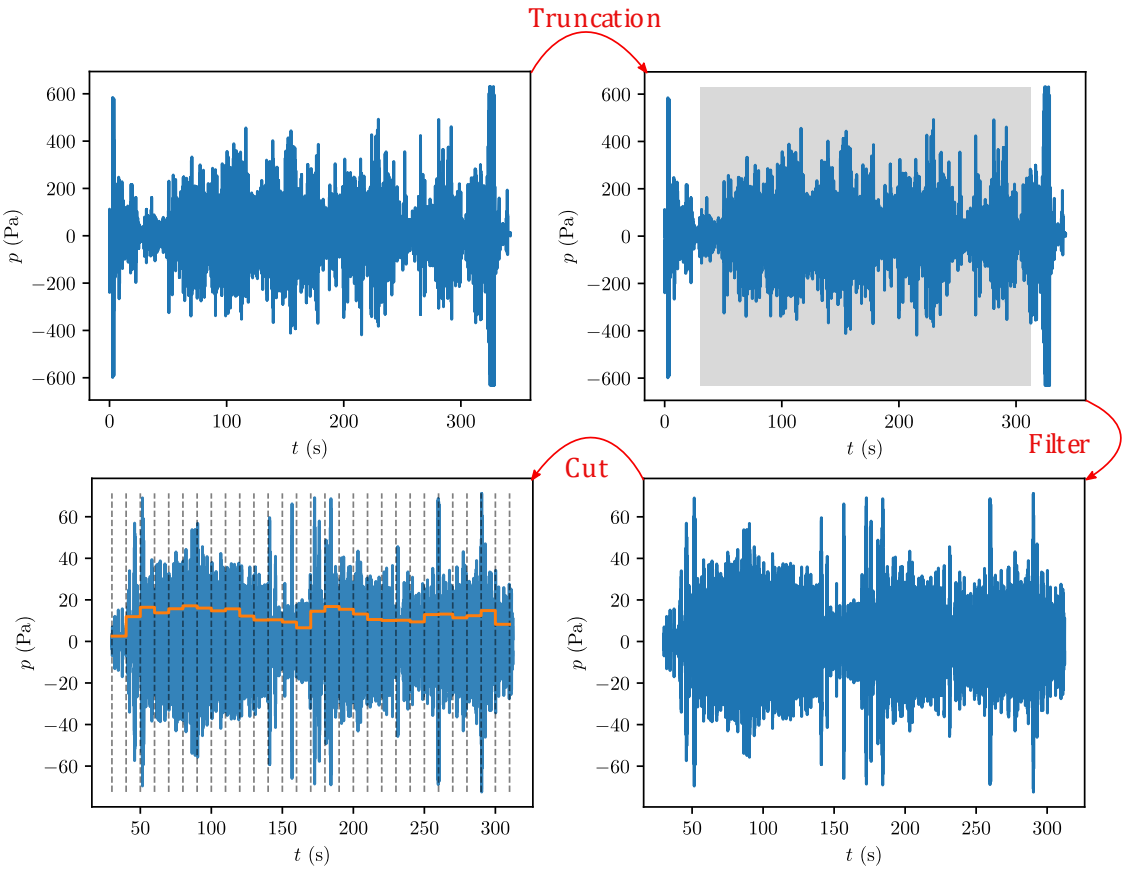


Figure 25. Processing scheme.

In the end, the result is a matrix consisting of the SPL of each sub-signal of every complete signal, such that we can associate a SPL value for each moment in time of the temporal monitorization. Every subsequent result will be based on a particular analysis of this very distribution. With the additional information of all the other variables (working regime of the converter and sea state), which time series are interpolated to match the exact timestamps of the acoustic data, it is readily possible to find which values of SPL correspond to each sea state and device operating regime.

Hereunder, a representative example of the filter behaviour in relation to the order is shown for the 1 kHz frequency band. It is observed that, for greater than 2nd orders filters, the frequency windowing is quite narrow, so that the final representation of the filtered signal will not be substantially modified. In the present study, a 6th order filter has been used.

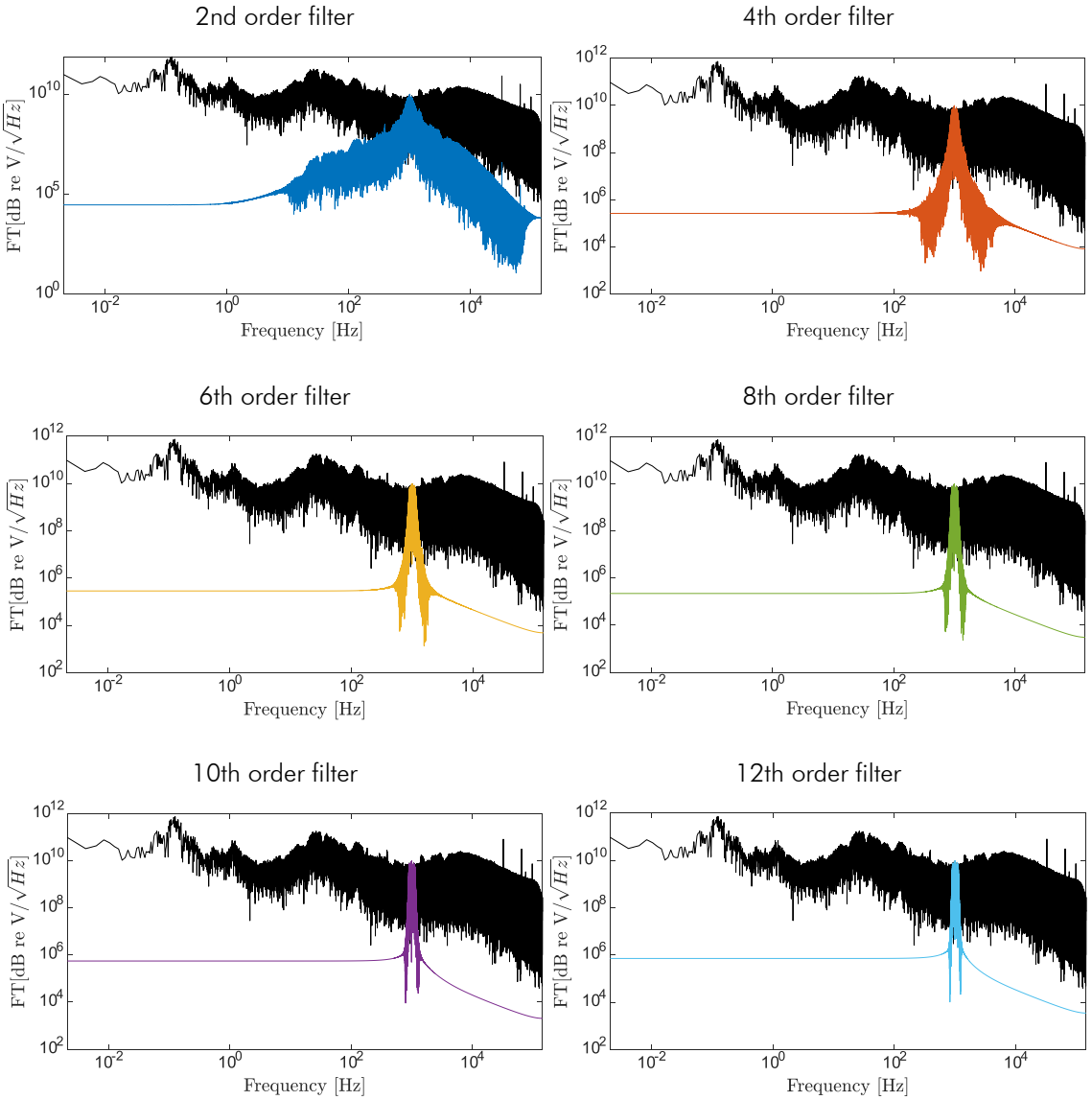


**Figure 26.** Example of the filter effect used on the acoustic signal spectrum.

## 6.2 Temporal analysis

We begin by presenting the results of the temporal monitorization (described in section 4.2) for each device separately.

### 6.2.1 MARMOK-A-5

After processing the data according to the scheme explained in section 6.1, a total of 49488 values of SPL corresponding to an $\Delta t$ of 10 seconds (each signal is divided into 48 sub-signals, therefore) were obtained, for each considered frequency. In the Figure 27, the time series consisting in the mean value of the sub-signals is plotted for

the two frequencies[5] identified by the MSFD as most relevant for anthropogenic noise studies.

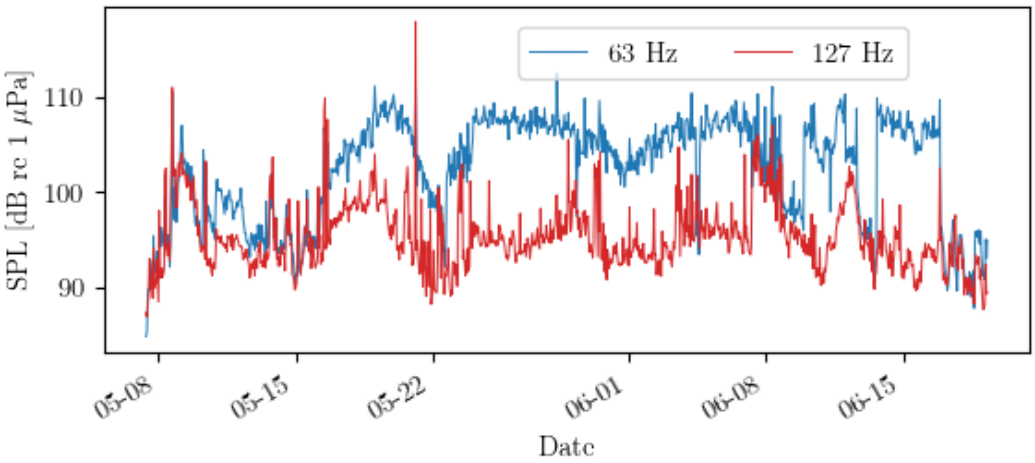


**Figure 27.** SPL time series from the temporal monitorization of MARMOK-A-5 for two selected frequencies.

As can be already noted, the SPL time series drawn in Figure 27 differ with those from the earlier campaign in 2012 (Figure 11) in some aspects, like higher sound levels overall, and a higher temporal dependency. In any case, peak levels are similar in both cases, reaching above 110 dB re 1 μPa; the dependence on frequency is also similar: the 63 Hz component have an average value of SPL 10 dB higher than that of 127 Hz.

We should remind that both time series are not comparable, since they were not acquired in the same conditions (different hydrophone location, different period of year, etc.).

We classify all signals in two groups, corresponding to the two states (on and off) of the converter (see section 5.3.1), which will be studied thoroughly in the following subsections.

#### *6.2.1.1 Background noise (**off state**)*

We first focus on the background (ambient) noise when the device was not effectively operating.

- **Previsualization and outlier identification:**

We select the time intervals when the converter was off ($\Omega < 0.1$) to see the corresponding values of background SPL, which will be considered the baseline background noise (marked as grey bands in Figure 16). We have identified a total of

[5] The frequencies should be 62.5 and 125 Hz. We used the closest ones of our analysis.

10858 sub-signals corresponding to this regimen. These are displayed as a function of frequency in Figure 28, in which the histogram of the whole distribution of SPL is also shown (for every frequency). In this figure it is obvious the presence of some outliers, especially in the lower frequencies and in situations when the wave heights were quite low ($H_w < 1$ m).

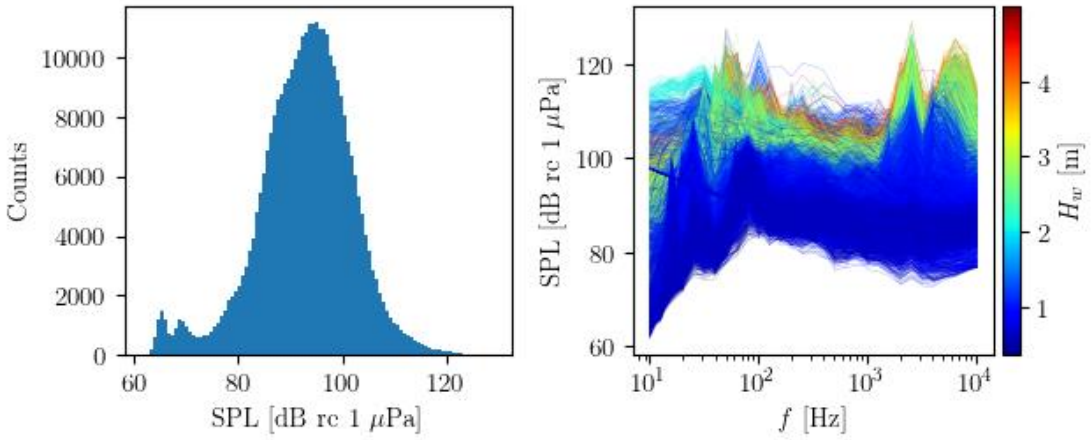


Figure 28. (Left) SPL histogram and (right) SPL as a function of frequency, coloured by corresponding wave height, for background acoustic signals.

To make the dataset cleaner, we take these outlying signals out of our analysis. More formally, for all the background acoustic data, once have been binned in different intervals of $H_w$, any signal in which the condition $\mathrm{SPL} \geq \mathrm{SPL}_{95}$ is satisfied ($\mathrm{SPL}_{95}$ stands for percentile 95 of the SPL distribution) for any frequency will be discarded. This will filter out some signals in which unwanted acoustic events have been introduced (hydrophone mount self-noise, vessels passing close by, etc.), while not altering too much the original distribution.

With this criterion, in Figure 29 we update the results of Figure 28 to see how SPL values are now distributed. Some outliers have been discarded, resulting in a more reasonable distribution (in general, lower significant wave height now correspond to lower SPL values). We remark that, in what follows, and unless otherwise explicitly indicated, these are the definitive values that will be used for further analysis.

- SPL final distribution:

After dropping the outlying values (1820) the final distribution consists of 9038 elements.

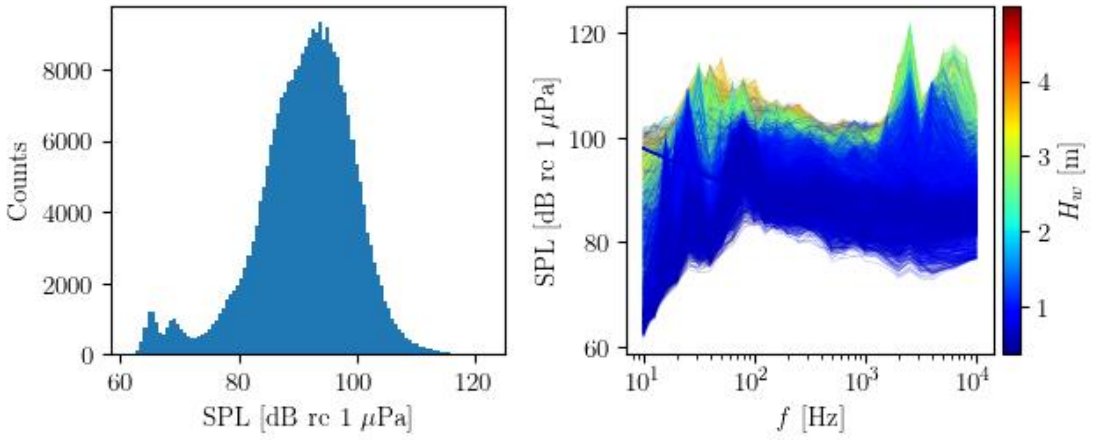


Figure 29. (Left) SPL histogram and (right) SPL as a function of frequency, coloured by corresponding wave height, for background acoustic signals after dropping outliers.

In Figure 30 the SPL box plot in frequencies is displayed; we detect higher deviation with respect to the median value for low (up to 100 Hz) and high frequencies (from 2 kHz upwards). Therefore, noise in these frequencies is most variable, whether it is caused by natural (animals, rain, wave induced noise, etc.) or anthropogenic (vessels) sources.

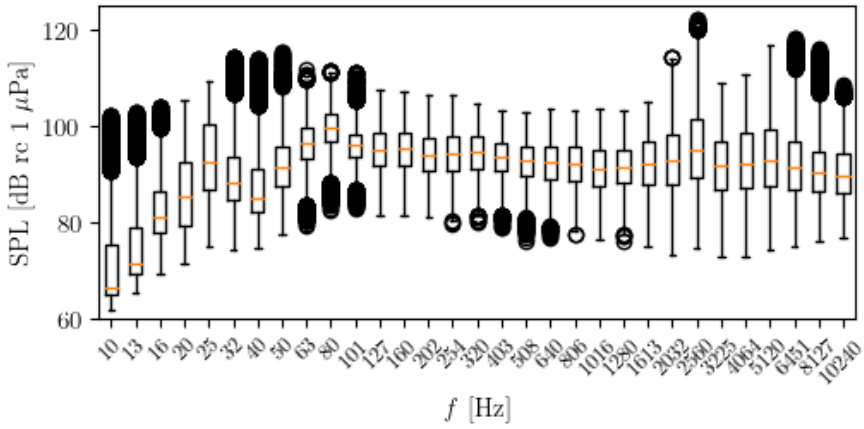


Figure 30. SPL box plot graph for background acoustic signals.

- SPL in $H_w$ bins:

Identifying significant wave height as the main indicator of sea natural ambient noise, it is useful to bin the data according to this parameter. After studying the distribution of significant wave height data (Figure 31), three bins are defined to classify other data according to this parameter: these are given by $H_w < 1$, $1 \leq H_w < 2$, and $H_w > 2$ (up to ~5 m, which was the maximum wave height registered during the acoustic monitoring).

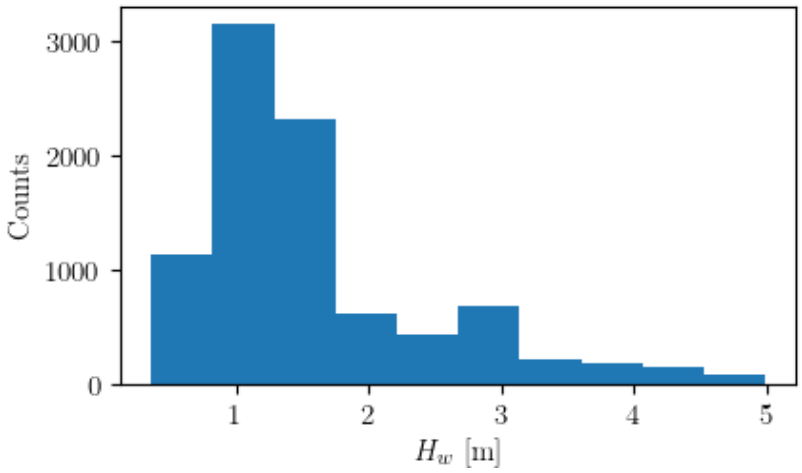


**Figure 31.** Histogram of the significant wave height time series (according to Figure 14) for the case of MARMOK-A-5.

There is a good number of data samples for each of these groups (2487, 5231 and 3140, respectively), ensuring a good variability of conditions in which the converter was off. In Figure 32 the average SPL is calculated for every wave height bin, confirming, as expected, the fact that the higher the significant wave height the higher the average SPL for the full spectrum of frequencies.

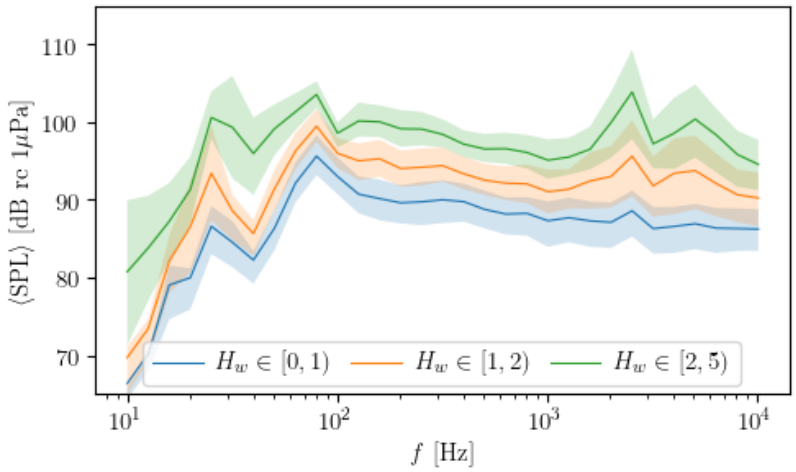


**Figure 32.** Mean SPL values for background signals classified in wave height bins. Deviations defined by Q1 and Q2 (percentile 25 and 75) are added as shaded bands.

We find some peaks for mean SPL in 25, 80 and 2560 Hz (and around 5120 Hz for highest $H_w$), with values approximately ranging from 87, 95 and 89 (for lowest $H_w$ bin) to 100, 104 and 104 (for highest $H_w$ bin) dB re 1 µPa, respectively.

In Figure 33 we have classified the data results according to the aforementioned bins and now calculated the percentile distribution (in an interpolated way) for every such

wave height state. These plots show (i): the almost exact coincidence of mean and median, (ii): the frequencies with higher deviations between values are found in both ends of the spectrum (up to ~ 60 Hz in one case, and from 1 kHz upwards), (iii): deviations are higher for higher values of $H_w$, specifically in the mentioned frequency regions, (iv): there seems to be a shift in the absolute maximum from the one that appears near 80 Hz to the one at around 2560 Hz as we increase wave height, with a maximum value for the 95th percentil of almost 118 dB re 1 µPa at such frequency.

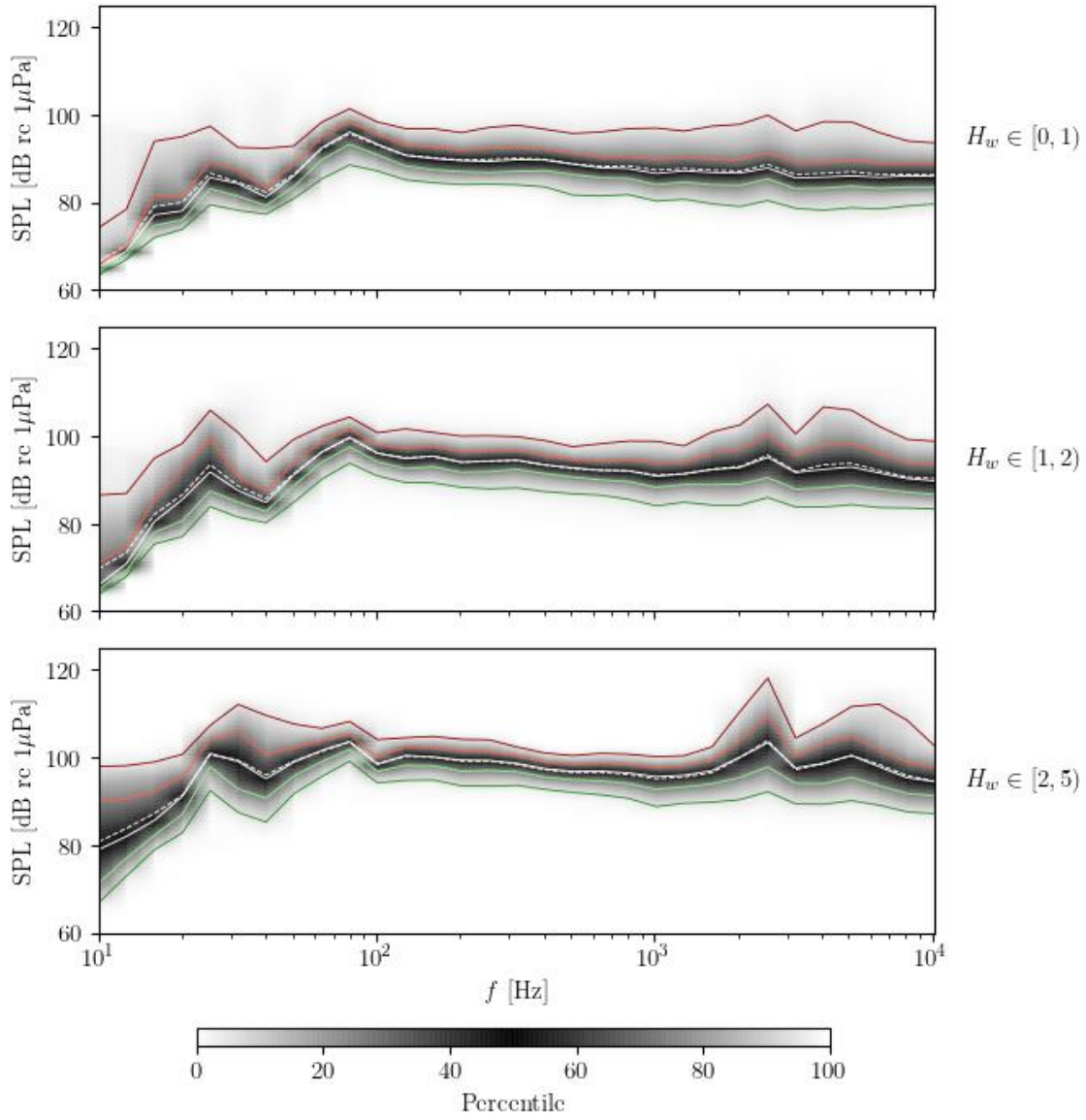


Figure 33. Percentile distribution as a colour graph for background noise classified by wave height, for MARMOK-A-5. In red (darker) $SPL_{95}$; (lighter) $SPL_{75}$. In green (darker) $SPL_5$; (lighter) $SPL_{25}$. In white (solid) the median $SPL_{50}$; (dashed) mean SPL.

- SPL dependence with respect other parameters:

For completeness, we now explore the dependence of $\mathrm{SPL}(f)$ with respect to the other parameters. These complement the results shown in Figure 34 and Figure 35, which are our main results of this subsection. In one hand, without binning in $H_w$, we can add this time series information as colour, as done in the next figures.

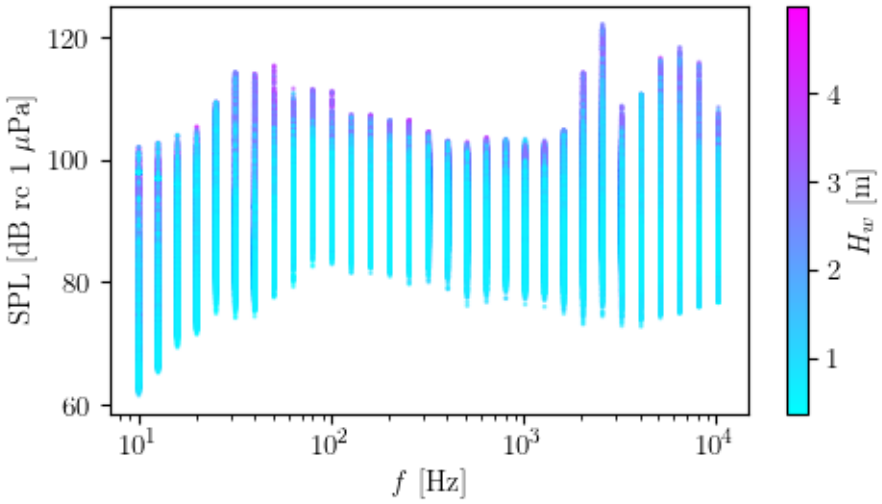


Figure 34. SPL colored by respective $H_w$.

Figure 34 confirm what was found in the last figures, that is, higher SPL values are associated to higher significant wave height values, with a clear prevalence of low wave height data, as was seen in the Figure 31.

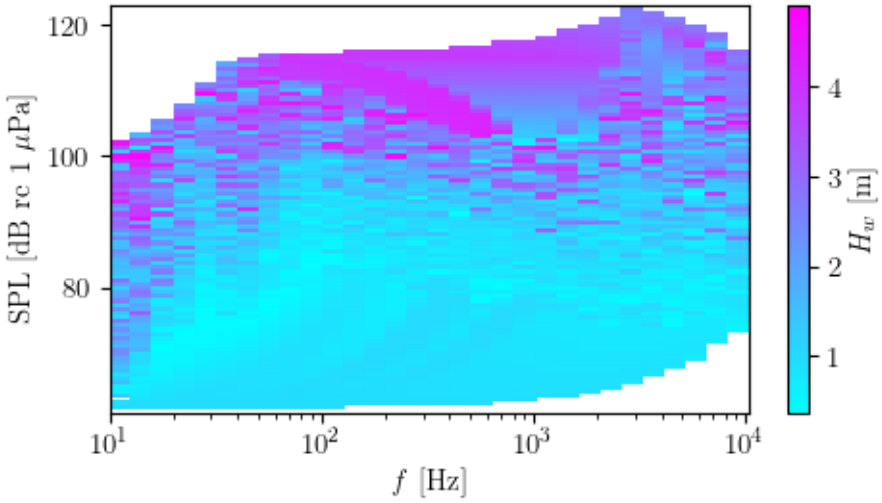


Figure 35. Interpolated grid plot of $\mathrm{SPL}(f)$ with $H_w$ in colour for background signals for MARMOK-A-5.

Another way of visualizing the results if by plotting the SPL against $\boldsymbol{H_w}$, as shown in the Figure 36 and Figure 37. Again, of course, obtained sound pressure levels are higher for higher wave height and lower frequencies.

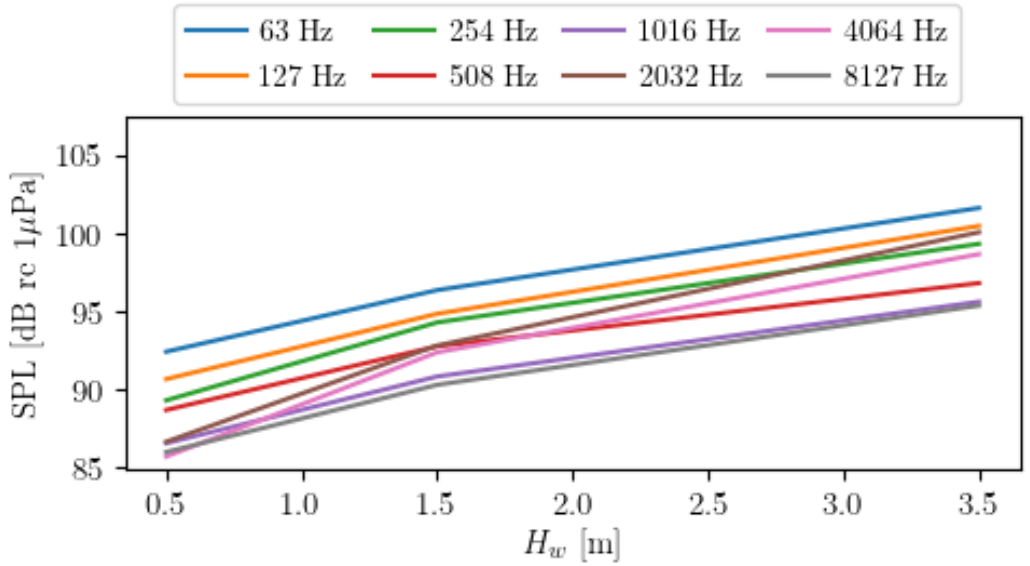


Figure 36. SPL as a function of $H_w$, for some frequency octaves for background noise for MARMOK-A-5.

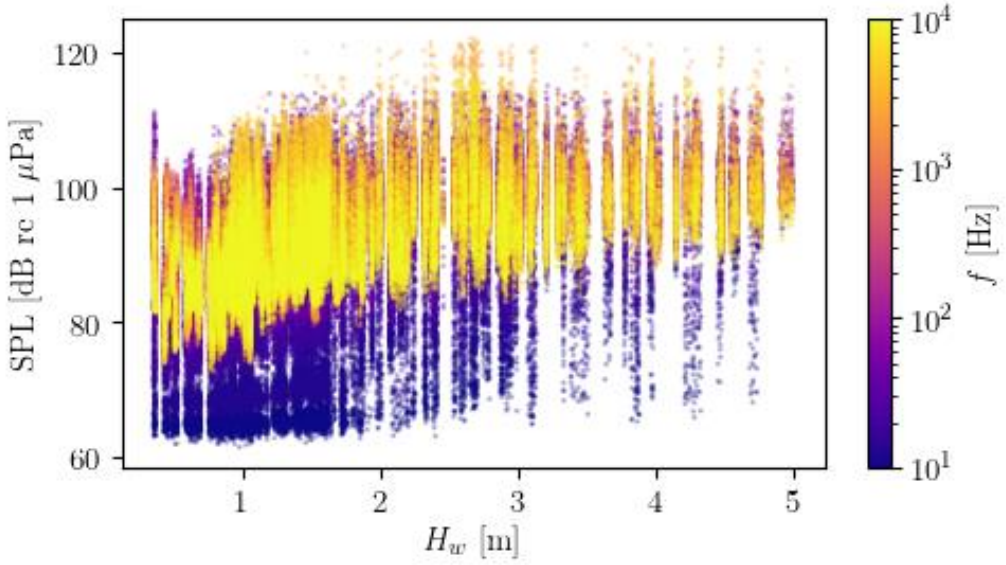


Figure 37. Scatter plot of SPL and $H_w$, coloured by frequency, for background signals for MARMOK-A-5.

- Correlation coefficients:

Finally, we calculate the Pearson correlation coefficients between SPL (of course, corresponding to the "off" regime) and significant wave height ($H_w$) and wave period ($T_w$), respectively. Results in Figure 38 show some correlation with respect to $H_w$, with a maximum of 0.73 at 50 Hz and an average value of 0.6. In the other hand, correlation with $T_w$ is essentially negligible, with a maximum of 0.64 at the lowest frequency[6] (10 Hz) and an average value of 0.35.

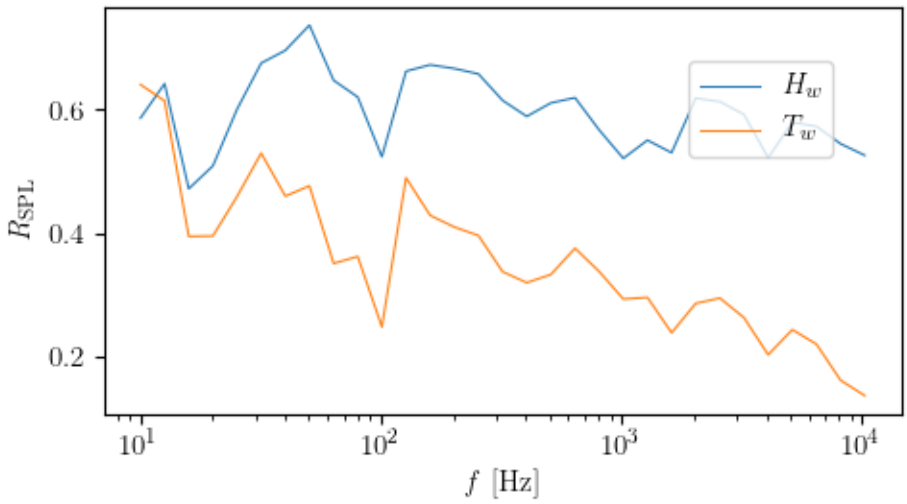


Figure 38. Pearson correlation coefficients between SPL and $H_w$, $T_w$, respectively, for background signals, for MARMOK-A-5.

### *6.2.1.2 Background plus converter noise (on state)*

Having characterized the baseline background noise levels for different sea states, we now consider the source noise too, by taking the samples in which $\Omega \geq 0.1$. We find many more samples in this group than before, amounting to a total of 38630.

- Previsualization and outlier identification:

Proceeding as before, the raw distribution of values of SPL is shown in Figure 39. There seem to be some clear outliers in this distribution as well, with values of SPL reaching 120 dB re 1 µPa for very low wave heights. Again, we drop those samples satisfying the condition $\mathrm{SPL} \geq \mathrm{SPL}_{95}$ for any frequency of the spectrum.

[6] This was expected since at very low frequencies, hydrostatic pressure changes are caused by the variability of the water column depth from the passing of waves.

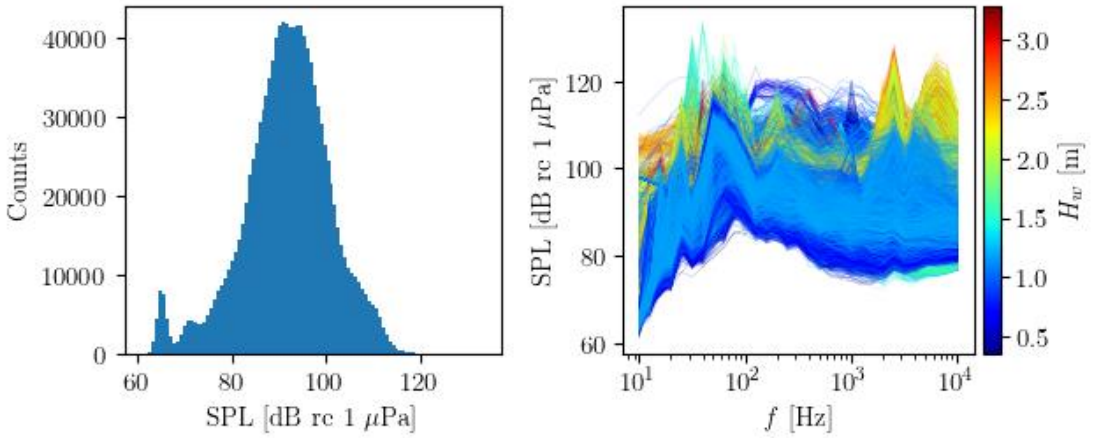


Figure 39. (Left) SPL histogram and (right) SPL as a function of frequency, coloured by corresponding wave height, for not background acoustic signals, for MARMOK-A-5.

- SPL final distribution:

After dropping the outliers, 33378 samples remain, which are again plotted in Figure 40.

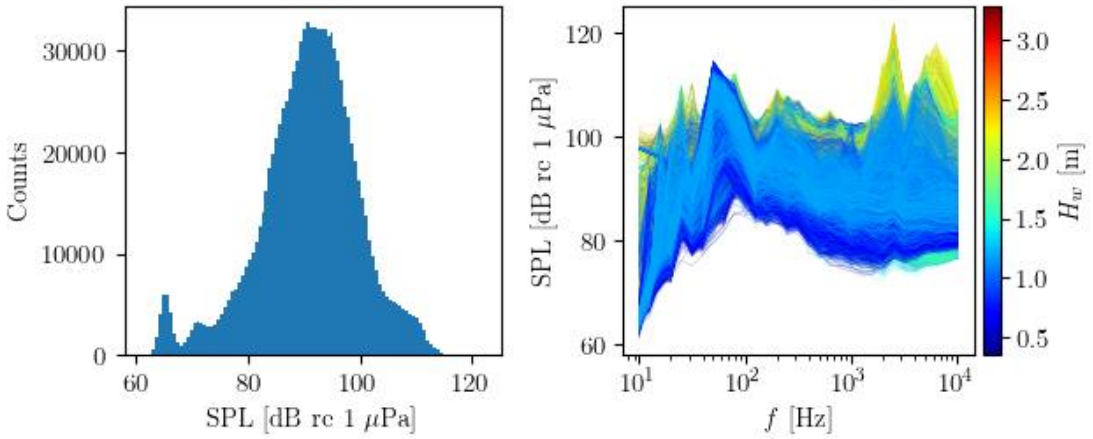


Figure 40. (Left) SPL histogram and (right) SPL as a function of frequency, coloured by corresponding wave height, for background acoustic signals, after dropping outliers, for MARMOK-A-5.

The box plot of Figure 41 show some appreciable differences already. In the first place, the sound pressure levels are a bit higher, in average, with medians bounded between roughly between 90 and 103 dB re 1 **μ**Pa (except for the lower frequencies). There is also a clear increase in the levels from 32 Hz to 100 Hz, which seems to be a particular signature of the converter. There are many more outliers in the lowest frequencies too.

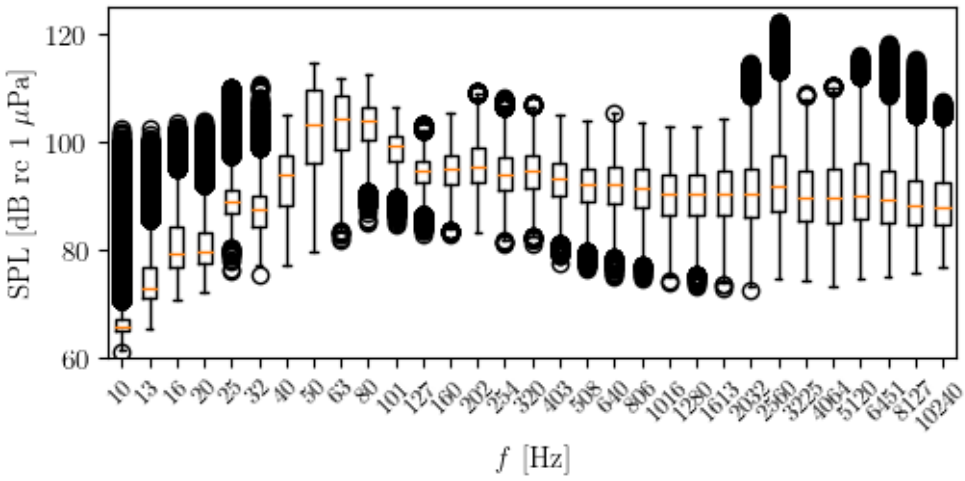


**Figure 41.** SPL box plot for non-background signals. A value of $\mathrm{IQR} = 1.5$ was used.

- **SPL in $H_w$ bins:**

Interestingly, the maximum wave height found in any period with device operation was 3.28 meters, lower than the respective one found during no operation at all (greater than 4 meters) (Figure 42).

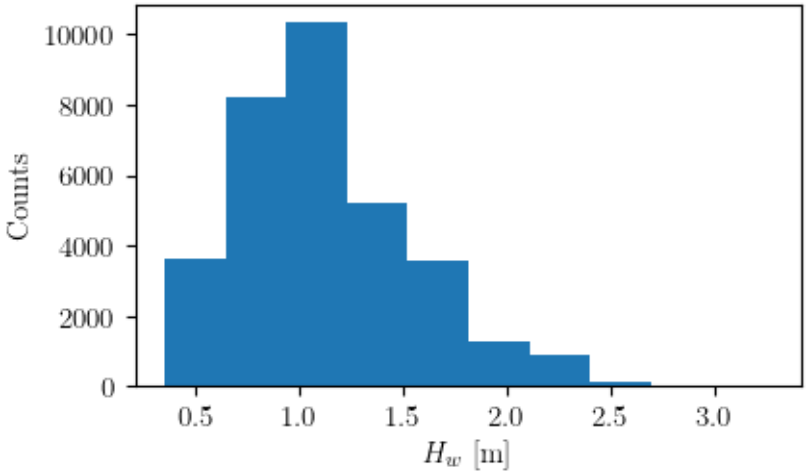


**Figure 42.** Histogram of $H_w$ corresponding to non-background signals.

In the Figure 43 the average SPL is calculated for every significant wave height bin. The main difference with the corresponding figure when the converter was off is noticeable: the sound pressure level values have particularly risen in the frequencies ranging from 50 to 100 Hz, approximately. In average, all sound pressure levels are a bit higher. This can be seen in Figure 44 too.

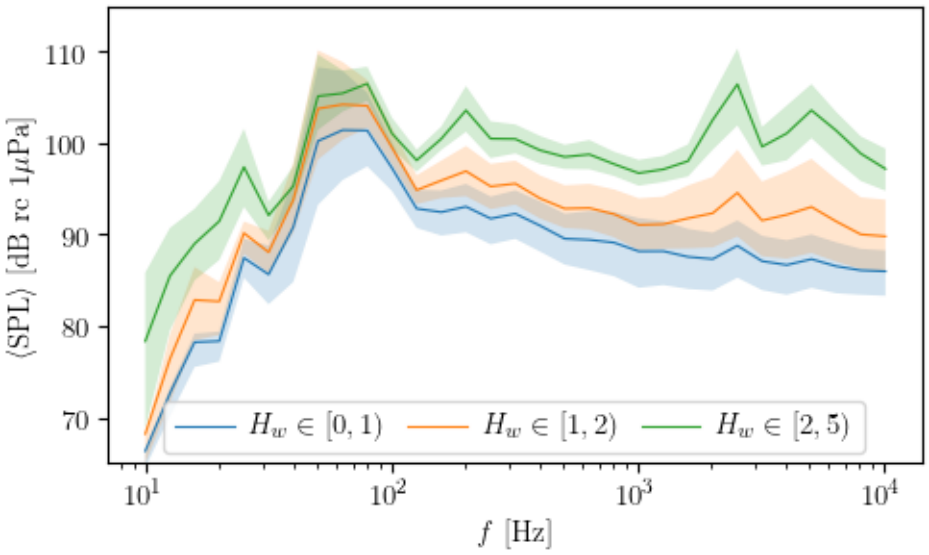


Figure 43. Mean SPL values for non-background signals classified in wave height bins. Deviations defined by Q1and Q2 are added as shaded bands.

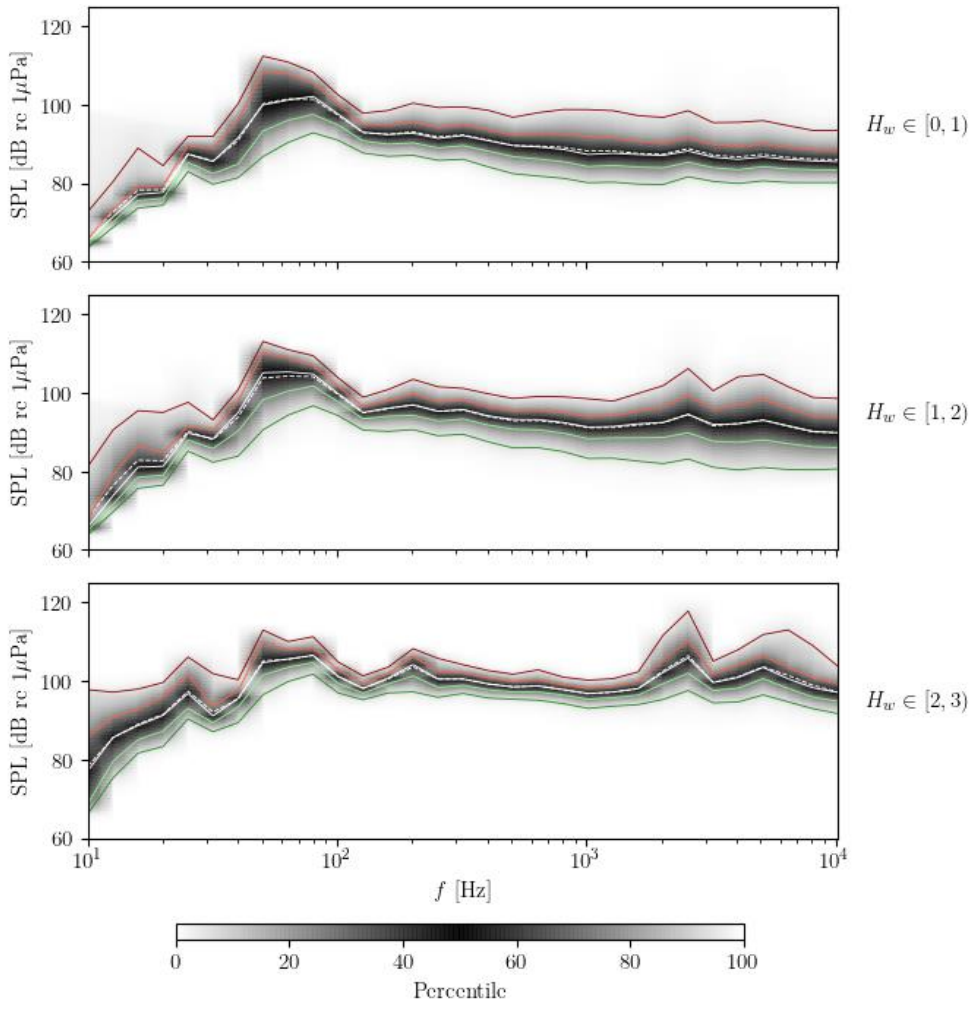


Figure 44. Percentile distribution as a colour graph for non-background noise classified by wave height, for MARMOK-A-5. In red (darker) $SPL_{95}$; (lighter) $SPL_{75}$. In green (darker) $SPL_5$; (lighter) $SPL_{25}$. In white (solid) the median $SPL_{50}$; (dashed) mean SPL.

- SPL dependence with respect to other parameters:

As before, we know explore other dependences of SPL with respect to other parameters. Without binning the $H_w$, Figure 45 and 46 show this parameter with colour as scatter plot and a interpolated grid plot. Again, most of the high SPL values correspond to high values of $H_w$.

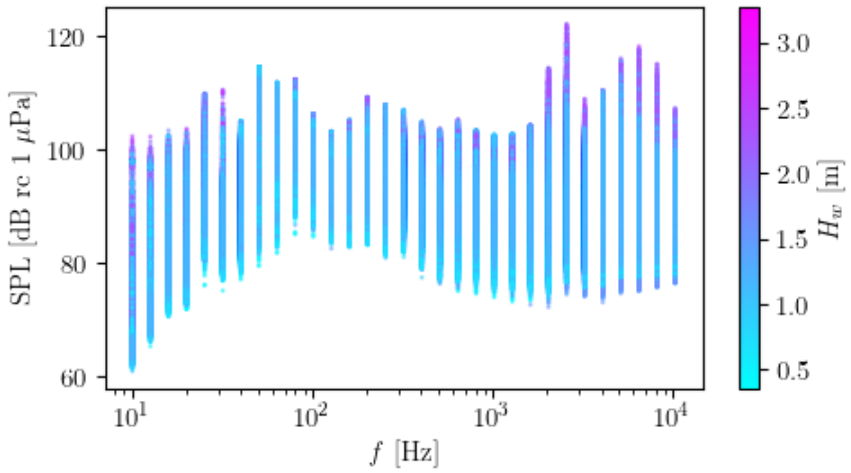


Figure 45. Scatter plot of SPL($f$) with $H_w$ in colour for non-background signals for MARMOK-A-5.

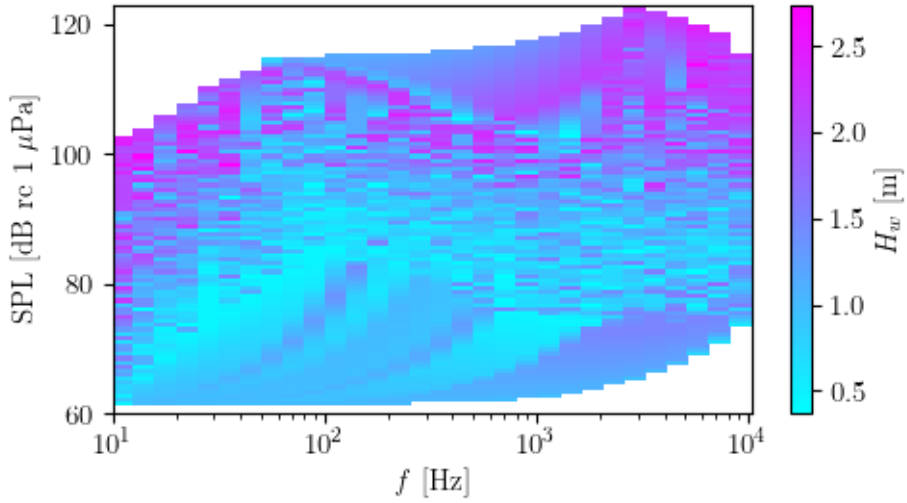


Figure 46. Interpolated grid plot of SPL($f$) with $H_w$ in colour for non-background signals for MARMOK-A-5.

In Figure 47, $H_w$ is displayed in the horizontal axis for some selected frequency octave bands. For every one of them, SPL increases as wave height does and as frequency decrease, overall. However, the SPL for high frequencies surpass some of the low frequencies, revealing some sound generation mechanism very dependent on wave height.

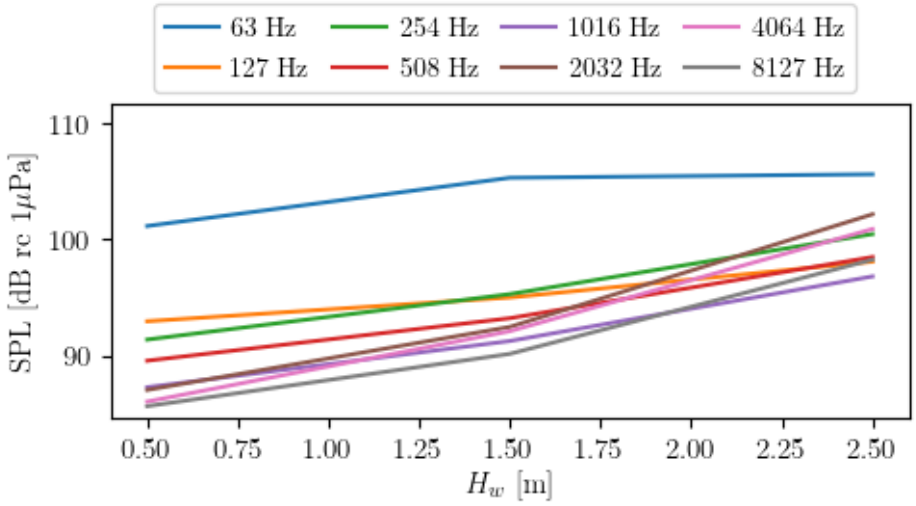


**Figure 47.** SPL($H_w$) for some frequency octave bands for non-background signals for MARMOK-A-5.

Another interesting parameter to consider is the power of the turbines. In the Figure 48 SPL values have been binned according to power output. Even though it is clear that SPL rises as power increases for the lower $P$ bins ($P \approx 1$, $P \approx 2$), once it reaches higher values of power, SPL values get more overlapped.

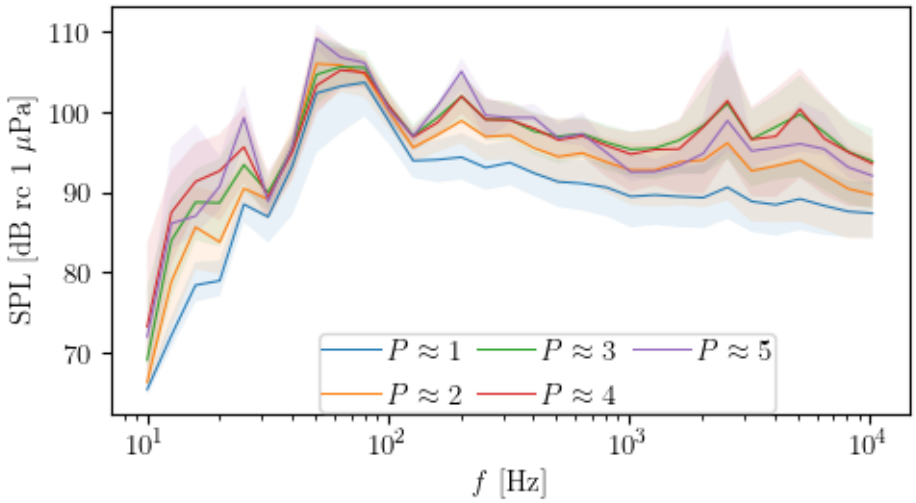


**Figure 48.** SPL as a function of $f$, coloured by power output for non-background signals for MARMOK-A-5.

The Pearson correlation coefficient between SPL and some other parameters is plotted in Figure 49. The highest correlation is again given by $H_w$, followed by $P$ and $\Omega$ closely, and by $T_w$ in last place. $R_{\mathrm{SPL},T_w}$ is remarkably low now for non-background signals (to be compared with 47), even reaching negative values (anti-correlation).

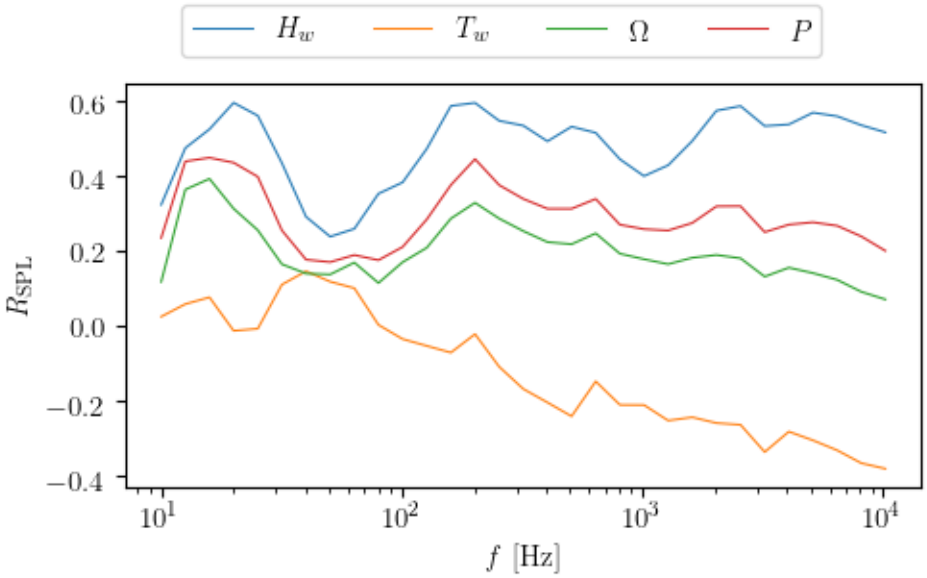


**Figure 49.** Pearson correlation coefficients between SPL and $H_w$, $T_w$, $\Omega$ and $P$ respectively, for non-background signals, for MARMOK-A-5.

### *6.2.1.3 Conclusions*

As we have seen in the previous subsections, on and off regimes show different SPL behaviour. To explicitly evidence this, in Figure 50 the difference between both modes is calculated for the three $H_w$ bins ($\Delta\mathrm{SPL} = \mathrm{SPL}_{\mathrm{on}} - \mathrm{SPL}_{\mathrm{off}}$). There is a clear variation of SPL in the low frequencies, centred in 50 Hz, of almost 14 dB re 1 µPa, that seem to decrease as wave height increases. For the rest of frequencies there seems to not be any relevant difference, given the high uncertainty[7] this variable is subjected to.

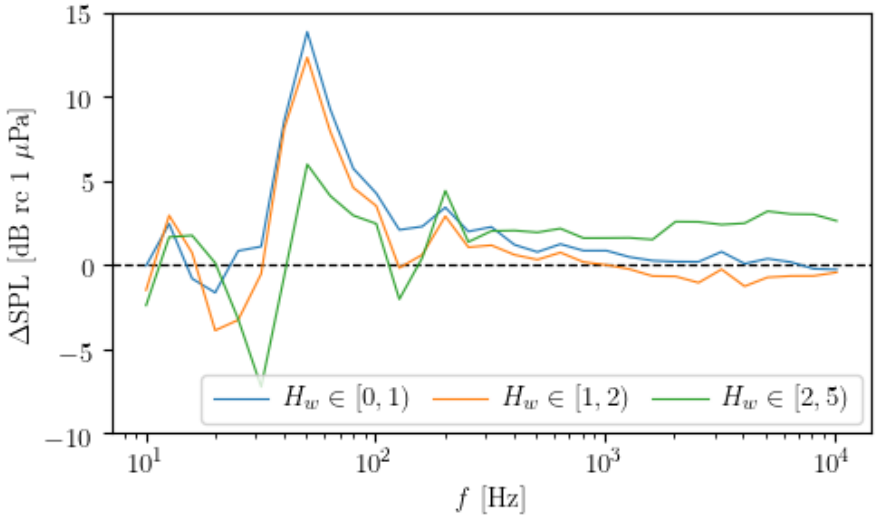


**Figure 50.** Difference between $\mathrm{SPL}_{\mathrm{on}}$ and $\mathrm{SPL}_{\mathrm{off}}$ for every $H_w$ bin for MARMOK-A-5.

[7] Not shown here for visibility reasons. See instead Figure 43 and Figure 50.

In summary, for background noise (device is off), we find SPL relative peaks at 25, 80 and 2560 Hz, that increase as wave height increases, with values approximately ranging from 87, 95 and 89 (for lowest $H_w$ bin) to 100, 104 and 104 (for highest $H_w$ bin) dB re 1 μPa, respectively, with the highest variability found in the lowest frequencies (from 10 to ~60 Hz) and the high frequencies (2560, 5120 Hz). Interestingly, a clear increase in the SPL at 2560 Hz is noticeable for high $H_w$ values. This signature was attributed to clashing of the mooring chains of the device (note the second harmonic at 5120 Hz).

For non-background noise (device is on), we find same relative peaks at 25 and 2560 Hz (and the harmonic 5120 Hz, particularly at high wave heights), but now from 50 to 100 Hz higher values of SPL appear, almost independent of $H_w$, and which seem to be the main signature of the energy converter MARMOK-A-5.

In the end, the most relevant difference in noise due to the operation of the device is found in the low frequencies, piking at 50 Hz, with peak difference values in SPL of 14, 12 and 6 dB re 1 μPa for $H_w < 1$, $1 \leq H_w < 2$, and $H_w > 2$, respectively. We remind that these results are spatially referenced to a distance from the converter of almost 100 meters.

In Table 10, 11 and 12, the exact results (difference of the average value, as well as standard deviation of the difference) are shown for every frequency and wave height bin; the row in which the highest difference is found is highlighted in bold font.

**Table 10.** SPL differences between on and off states for MARMOK-A-5 for $H_w \in [0,1)$ m.

| Frequency [Hz] | $\Delta\langle SPL \rangle$ [dB re 1 μPa] | $\delta SPL$ [dB re 1 μPa] |
|---|---|---|
| 10 | -0.04 | 10.94 |
| 13 | 2.46 | 9.99 |
| 16 | -0.8 | 11.06 |
| 20 | -1.64 | 10.04 |
| 25 | 0.85 | 8.4 |
| 32 | 1.1 | 8.29 |
| 40 | 8.57 | 11.51 |
| **50** | **13.86** | **12.33** |
| 63 | 9.26 | 10.73 |
| 80 | 5.74 | 8.89 |
| 101 | 4.27 | 6.97 |
| 127 | 2.1 | 6.57 |
| 160 | 2.3 | 7.27 |
| 202 | 3.43 | 7.59 |
| 254 | 2.0 | 7.93 |
| 320 | 2.27 | 7.98 |
| 403 | 1.21 | 8.11 |
| 508 | 0.78 | 8.36 |
| 640 | 1.25 | 9.05 |
| 806 | 0.86 | 9.59 |
| 1016 | 0.86 | 10.45 |
| 1280 | 0.48 | 9.98 |
| 1613 | 0.27 | 10.19 |
| 2032 | 0.21 | 10.33 |
| 2560 | 0.2 | 10.62 |
| 3225 | 0.79 | 9.67 |
| 4064 | 0.09 | 10.57 |
| 5120 | 0.38 | 10.37 |
| 6451 | 0.18 | 9.42 |
| 8127 | -0.22 | 8.37 |
| 10240 | -0.26 | 8.13 |

Table 11. SPL differences between on and off states for MARMOK-A-5 for $H_w \in [1,2)$ m.

| Frequency [Hz] | $\Delta\langle SPL\rangle$ [dB re 1 µPa] | $\delta SPL$ [dB re 1 µPa] |
|---|---|---|
| 10 | -1.48 | 14.32 |
| 13 | 2.95 | 13.29 |
| 16 | 0.73 | 11.73 |
| 20 | -3.88 | 12.27 |
| 25 | -3.26 | 11.08 |
| 32 | -0.52 | 9.25 |
| 40 | 8.12 | 9.78 |
| **50** | **12.34** | **11.51** |
| 63 | 7.93 | 9.03 |
| 80 | 4.61 | 7.17 |
| 101 | 3.52 | 5.97 |
| 127 | -0.17 | 6.18 |
| 160 | 0.62 | 6.68 |
| 202 | 2.91 | 7.49 |
| 254 | 1.06 | 7.44 |
| 320 | 1.18 | 7.09 |
| 403.17 | 0.61 | 7.13 |
| 507.97 | 0.32 | 7.06 |
| 640.0 | 0.75 | 7.45 |
| 806.35 | 0.18 | 8.08 |
| 1015.94 | 0.01 | 8.79 |
| 1280.0 | -0.24 | 8.25 |
| 1612.7 | -0.65 | 10.26 |
| 2031.87 | -0.67 | 11.52 |
| 2560.0 | -1.05 | 13.63 |
| 3225.4 | -0.25 | 11.02 |
| 4063.75 | -1.26 | 13.91 |
| 5120.0 | -0.73 | 13.73 |
| 6450.8 | -0.65 | 12.07 |
| 8127.49 | -0.64 | 10.41 |
| 10240.0 | -0.43 | 10.21 |

Table 12. SPL differences between on and off states for MARMOK-A-5 for $H_w \in [2,5)$ m.

| Frequency [Hz] | $\Delta\langle SPL\rangle$ [dB re 1 µPa] | $\delta SPL$ [dB re 1 µPa] |
|---|---|---|
| 10 | -2.39 | 20.46 |
| 13 | 1.67 | 15.05 |
| 16 | 1.77 | 11.4 |
| 20 | 0.13 | 10.71 |
| 25 | -3.2 | 9.57 |
| **32** | **-7.23** | **12.11** |
| 40 | -0.65 | 10.49 |
| 50 | 5.99 | 9.95 |
| 63 | 4.12 | 6.43 |
| 80 | 2.95 | 5.5 |
| 101 | 2.46 | 5.44 |
| 127 | -2.03 | 4.9 |
| 160 | 0.44 | 4.93 |
| 202 | 4.42 | 6.61 |
| 254 | 1.38 | 6.11 |
| 320 | 2.03 | 4.92 |
| 403.17 | 2.05 | 4.67 |
| 507.97 | 1.95 | 4.5 |
| 640.0 | 2.17 | 5.21 |
| 806.35 | 1.61 | 5.13 |
| 1015.94 | 1.61 | 5.62 |
| 1280.0 | 1.62 | 5.49 |
| 1612.7 | 1.52 | 6.48 |
| 2031.87 | 2.58 | 10.7 |
| 2560.0 | 2.57 | 13.68 |
| 3225.4 | 2.41 | 7.76 |
| 4063.75 | 2.49 | 9.86 |
| 5120.0 | 3.2 | 10.88 |
| 6450.8 | 3.04 | 11.74 |
| 8127.49 | 3.02 | 10.59 |
| 10240.0 | 2.63 | 4.67 |

### 6.2.2 Mutriku

For Mutriku we have a different setup than encountered in the previous converter, that is, many turbines (11) working possibly simultaneously, which makes the analysis a bit more complex. We present the results in the same way as before, separating every time series in two groups according to the "on" and "off" regime condition.

After processing the data according to the scheme explained in section 6.1, a total of 49008 values of SPL corresponding to an $\Delta t$ of 10 seconds (each signal is divided into 48 sub-signals, therefore) were obtained, for each considered frequency. In the next figure, the time series consisting in the mean value of the sub-signals is plotted for the two frequencies[8] identified by the MSFD as most relevant for anthropogenic noise studies.

In Figure 51 we see the average (mean of sub-signals within a signal) SPL time series for the whole period of monitorization in Mutriku for 63 and 127 Hz. There seems to be no significant difference between both series, with a mean value of 80 (standard deviation of 4.5) and 82 (5.6) dB re 1 μPa, respectively.

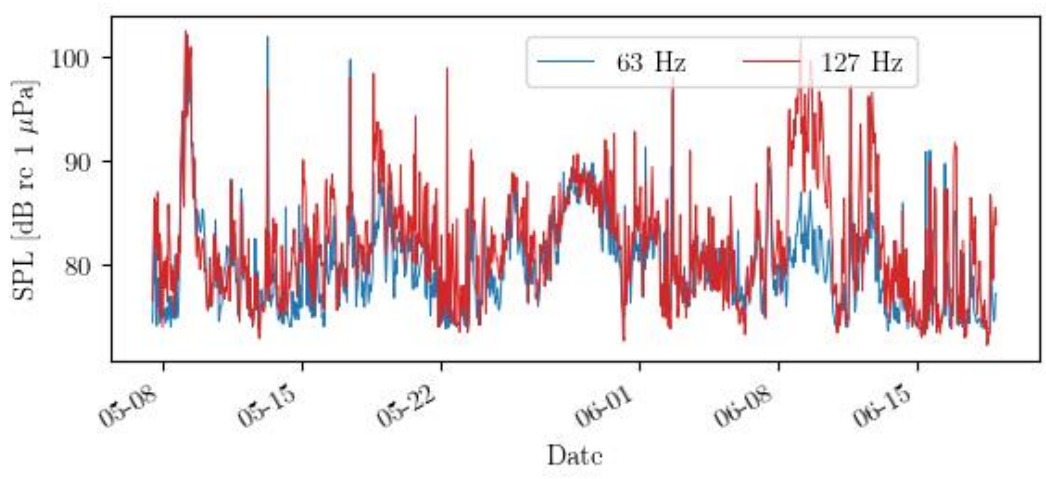


**Figure 51.** SPL time series from the temporal monitorization of Mutriku for two selected frequencies.

In the following sections we present the analysis of "on" and "off" regimes.

#### *6.2.2.1 Background noise (off state)*

We start with the background noise, with no operation at all from the Mutriku plant.

- **Previsualization and outlier identification:**

As we saw in Figure 20, the only time when every turbine was considered off was basically during the blackout occurred in the 8th and 9th of June 2019. We can exploit

[8] The frequencies should be 62.5 and 125 Hz. We used the closest ones of our analysis.

this fact to obtain the spectrum of background noise as recorded by the fixed hydrophone, in a similar way as we already did for MARMOK-A-5. However, unlike the previous converter, although in principle these two days could show enough variability in sea states, it was not the actual case, as can be seen in Figure 52, where the distribution is skewed to values higher than 1 meter. Note also that just 3984 of all 49008 sub-signals are classified in this group. This will be addressed later. The difference between this and the MARMOK-A-5 SPL distribution is quite notable, particularly in the high end of the spectrum.

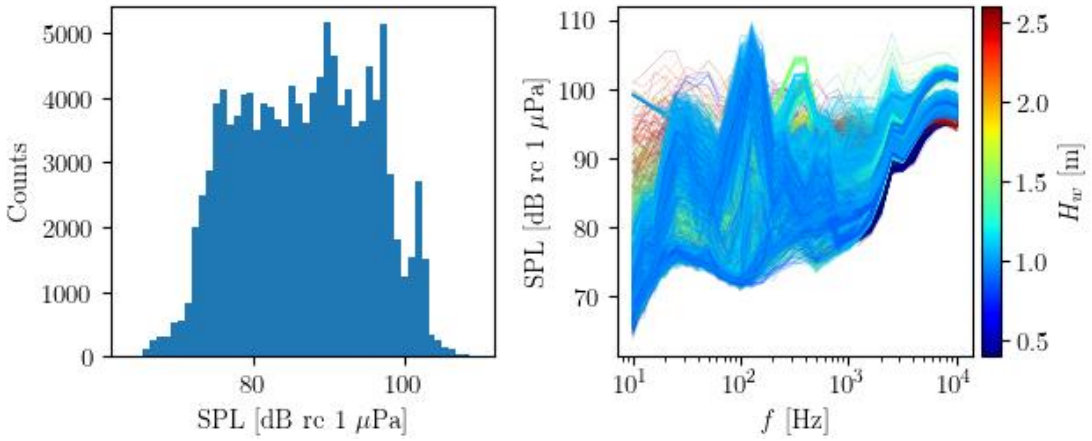


Figure 52. (Left) SPL histogram and (right) SPL as a function of frequency, coloured by corresponding wave height, for background acoustic signals, for Mutriku

In Figure 53 the distribution and SPL curves are shown before filtering out any outliers. Again, some clear outliers can be detected (highest values of SPL for low wave heights), so we proceed as before, dropping any signal that satisfies $\mathrm{SPL} \geq \mathrm{SPL}_{95}$.

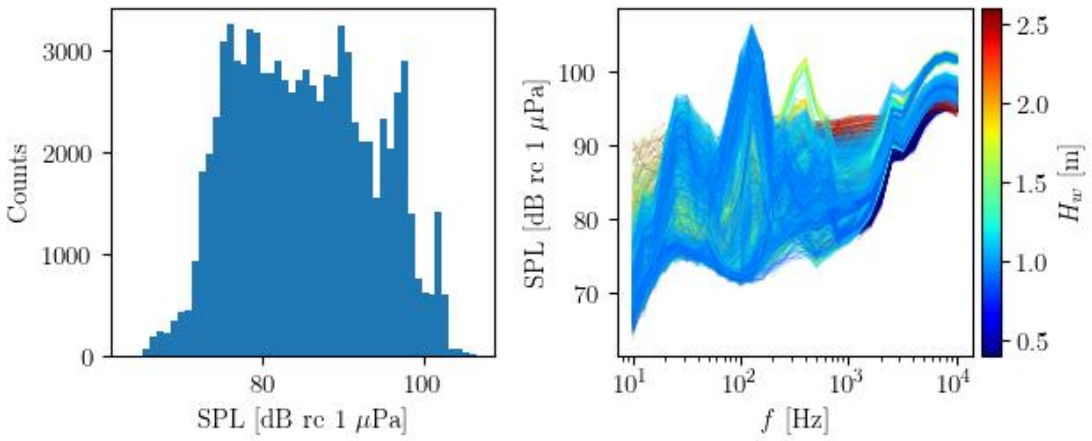


Figure 53. (Left) SPL histogram and (right) SPL as a function of frequency, coloured by corresponding wave height, for background acoustic signals after eliminating outliers, for Mutriku.

The updated distribution (with no outliers) is displayed in Figure 53, in which we can see some of the outliers have been dropped out. We remark that, in what follows, and unless otherwise explicitly indicated, these are the definitive values that will be used for further analysis.

- SPL final distribution:

After dropping the outlying values (1175) the final distribution consists of 2809 elements. In the SPL box plot in frequencies is displayed; we detect higher deviation with respect to the median value for the lowest frequencies (up to 16 Hz). In the low frequencies from 80 to 160 Hz we find the highest spread in SPL values, as was also detectable in Figure 53. These may be attributed to vessel noise, since the Mutriku area is usually transited by fishing vessels. There are not many outliers altogether in this distribution.

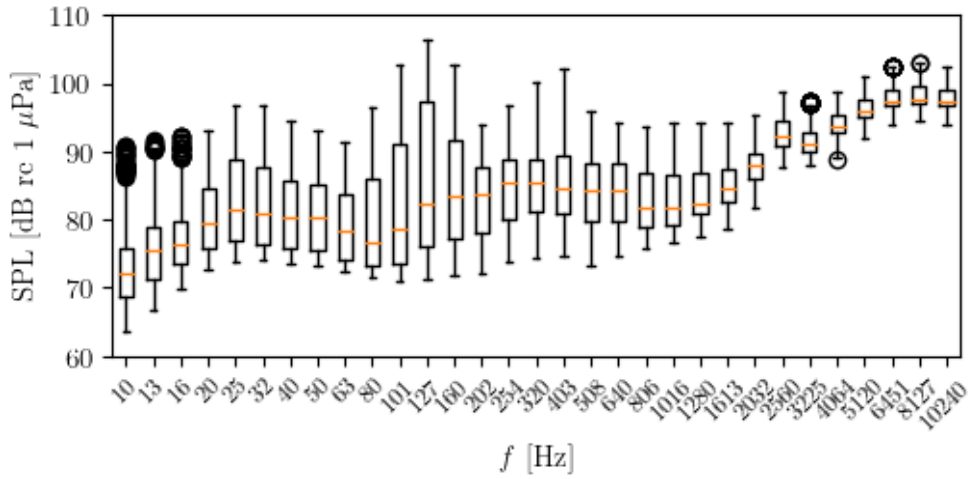


Figure 54. SPL box plot graph for background acoustic signals for Mutriku.

- SPL in $H_w$ bins:

In Figure 55 the wave height histogram corresponding to the off-state signals is presented. Binning in the same bins as before ($H_w < 1$, $1 \leq H_w < 2$, and $H_w > 2$), the data is further classified into three groups, consisting of 332, 1563 and 914 samples.

In Figure 56 the average SPL is calculated for every wave height bin, not showing a direct dependence on wave height. The highest values are concentrated in the high end of the spectrum, probably because of the filtering effect of shallow waters in low frequency sound propagation, reaching values of 99 dB re 1 μPa for the highest wave heights. There is a lot of variability at low frequencies (specially for medium wave heights), probably caused by vessels transiting close by the area.

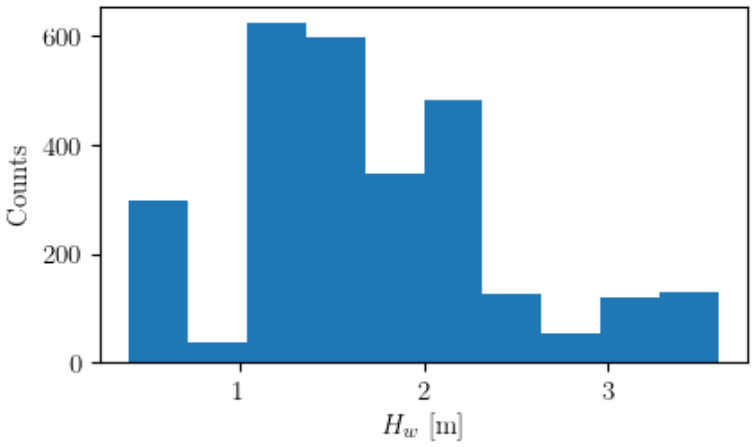


Figure 55. $H_w$ histogram for background signals for Mutriku.

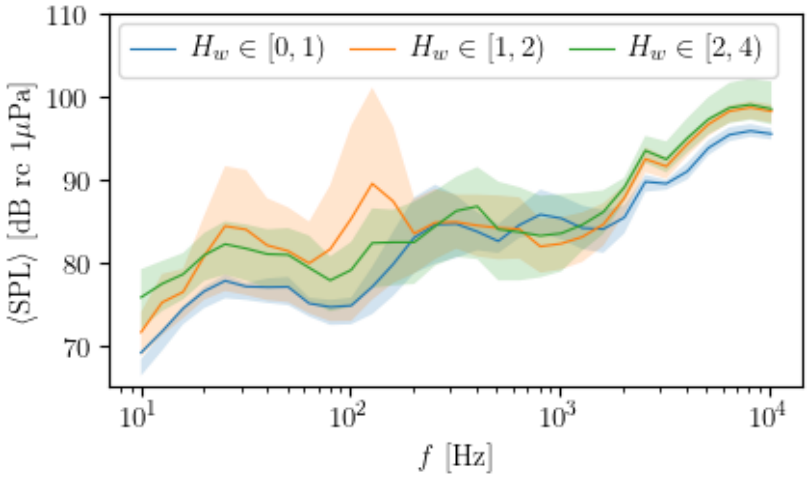


Figure 56. Mean SPL values for background signals classified in wave height bins in Mutriku. Deviations defined by Q1(percentile 25) and Q2 (percentile 75) are added as shaded bands.

In Figure 57 we have classified the data results according to the aforementioned bins and calculated the percentile distribution for every such wave height state. These results confirm what was mentioned before, that is, SPL values do not depend too much on wave height for this case, at least not as much as for MARMOK-A-5, and the high variability in the low frequencies for the $H_w \in [1,2)$ bin.

- **SPL dependence with respect to other parameters:**

Without binning the data into these three wave height classes, we specify the wave height as colour in the next figure, which show in more detail in which frequencies is the noise not particularly dependent on wave height: from 30 Hz to 120 Hz approximately. Figure 58, although showing some artifacts from interpolation, show this same behaviour.

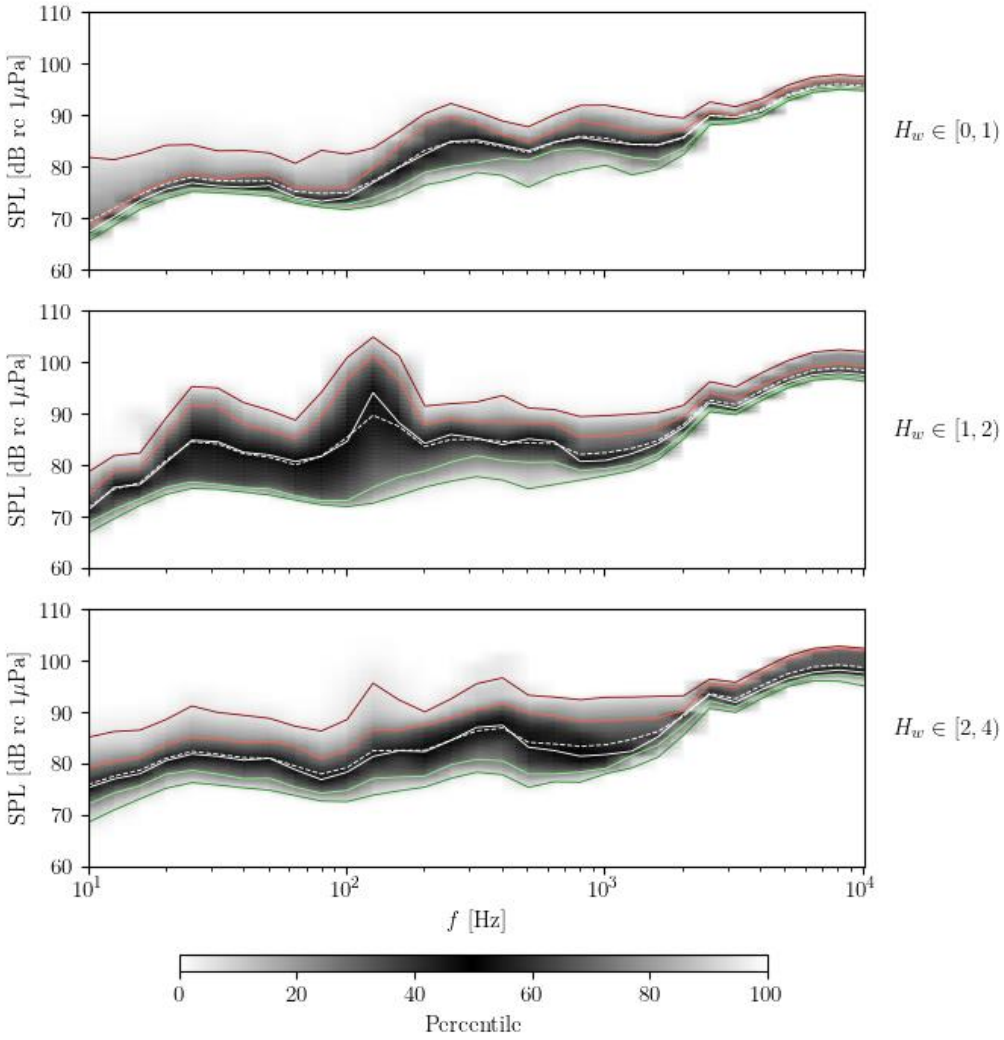


Figure 57. Percentile distribution as a colour graph for background noise classified by wave height, for Mutriku. In red (darker) $SPL_{95}$; (lighter) $SPL_{75}$. In green (darker) $SPL_5$; (lighter) $SPL_{25}$. In white (solid) the median $SPL_{50}$; (dashed) mean SPL.

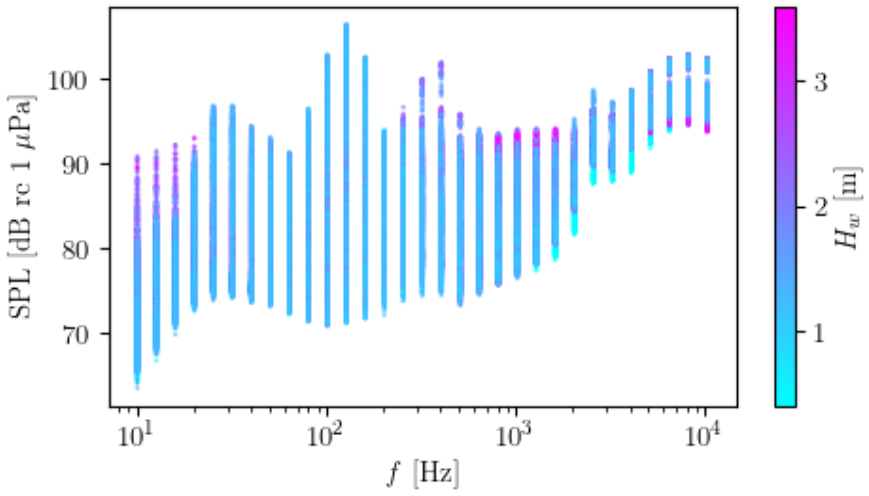


Figure 58. Scatter plot of SPL colored by respective $H_w$ for background noise in Mutriku.

These same results are also seen in Figure 60 and 61, now with $H_w$ displayed in the horizontal axis. Overall, while SPL seem to increase with $H_w$, the difference is almost negligible. Contrary to the case of MARMOK-A-5, now it is the higher frequencies that have the higher sound pressure level values. Note also the increase in 63 and 127 Hz for intermediate wave heights.

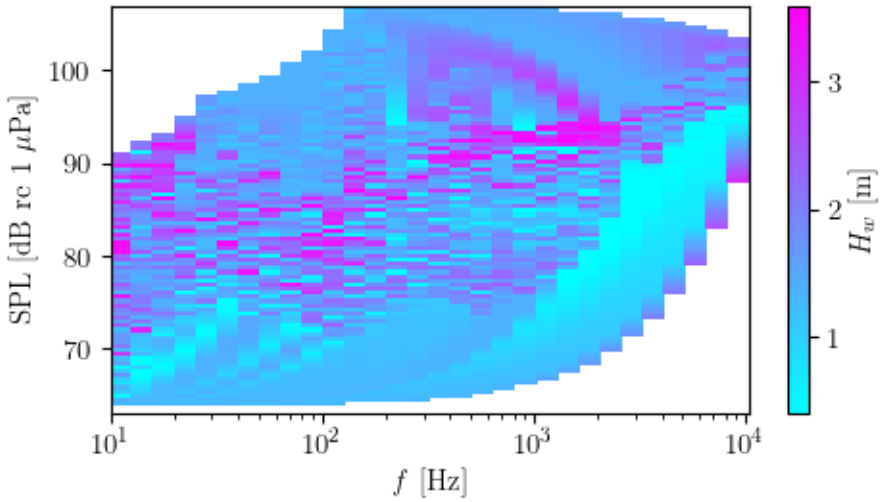


Figure 59. Interpolated grid plot of SPL($f$) with $H_w$ in colour for background signals in Mutriku.

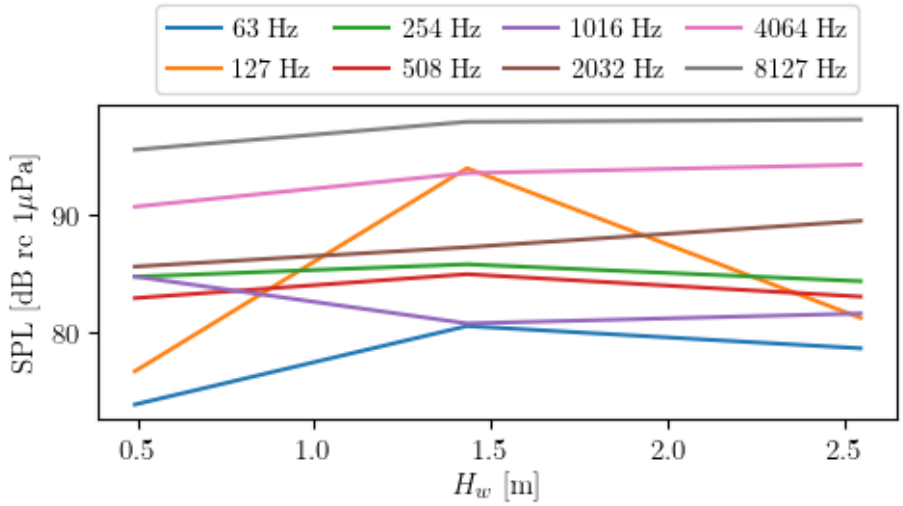


Figure 60. Average SPL as a function of $H_w$, for some frequency octaves for background noise in Mutriku.

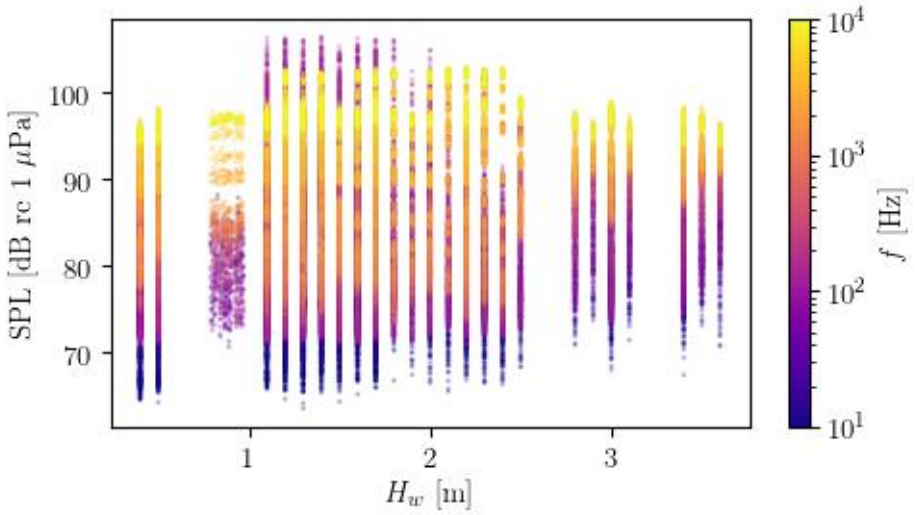


**Figure 61.** Scatter plot of SPL and $H_w$, coloured by frequency, for background signals for Mutriku.

Lastly, we analyse the correlation between SPL and $H_w$, more specifically, the Pearson correlation coefficient, shown in Figure 62. It shows local maxima at 10 and 2000 Hz, with values close to 0.5; this shows less correlation than the respective case for MARMOK-A-5.

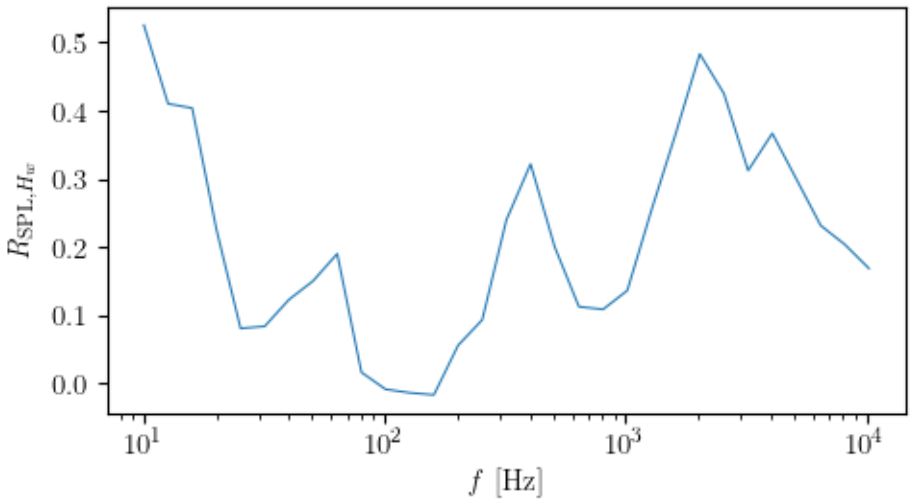


**Figure 62.** Pearson correlation coefficient between SPL and $H_w$, for the background noise in Mutriku.

### *6.2.2.2 Background plus converter noise (**on state**)*

- **Previsualization and outlier identification:**

Here we focus on the other case, when at least one turbine was operating (any of them satisfying $\Omega > 200$ rpm). The number of samples is now much higher, with 45024 sub-signals. As before, we start checking the original distribution of SPL (Figure 63). As

always, a lot of outliers can be detected; we will perform the same filtering approach as for other cases (refer to previous sections for more details) and update the figure as shown in Figure 64. This figure also shows a strong prevalence of wave heights of around 1 meter and not many cases of extreme values ($H_w$>3 meters).

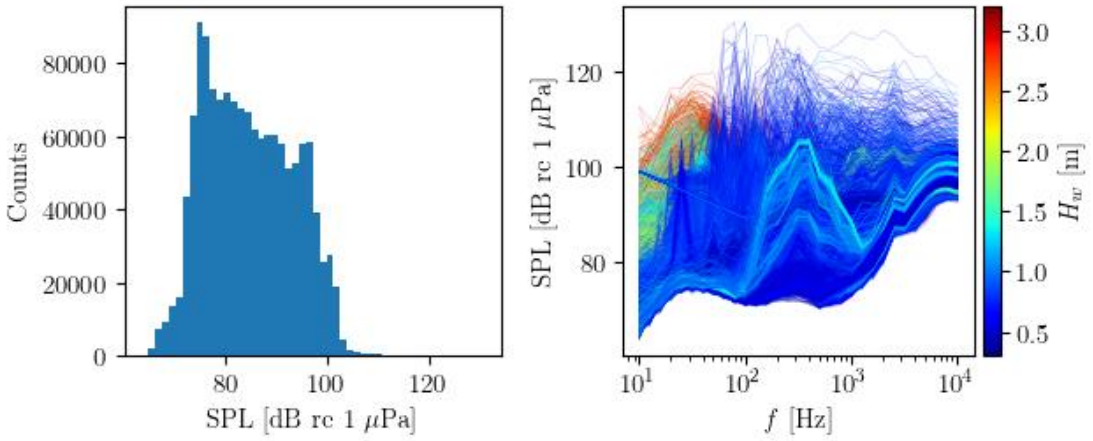


Figure 63. (Left) SPL histogram and (right) SPL as a function of frequency, coloured by corresponding wave height, for non-background acoustic signals, for Mutriku.

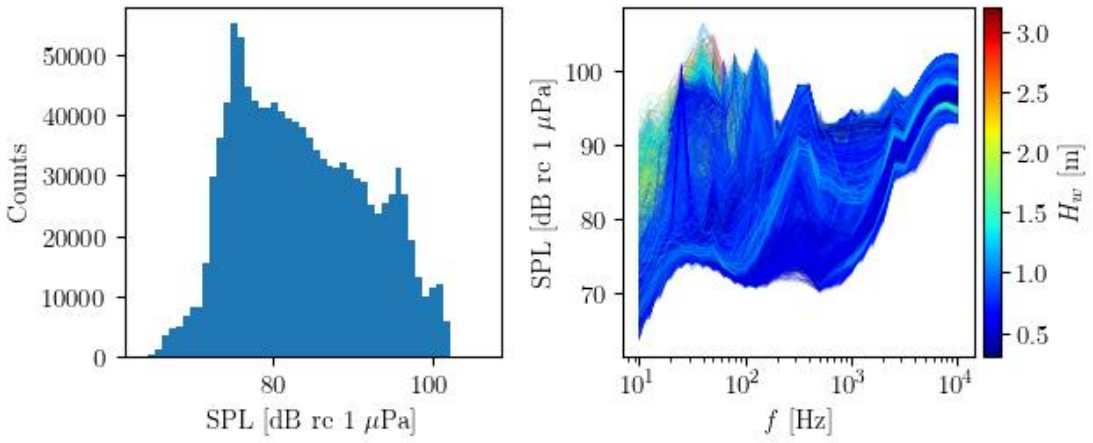


Figure 64. (Left) SPL histogram and (right) SPL as a function of frequency after dropping outliers, coloured by corresponding wave height, for non-background acoustic signals, for Mutriku.

- **SPL final distribution:**

A total of 7693 outlying signals are identified, which, after being discarded, make the total number of sub-signals amount to 37331.

In the box plot in Figure 65, a fairly big number of outliers is found at the lower frequencies. The median values of average SPL are quite similar to those represented in 58, with not much difference between both regimes so far.

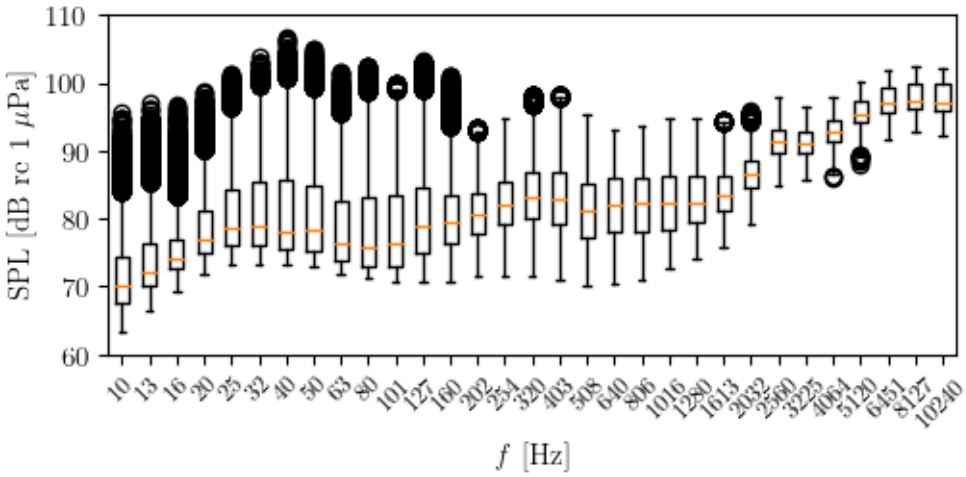


Figure 65. SPL box plot graph for non-background acoustic signals for Mutriku.

- **SPL in $H_w$ bins:**

In the same way as before, let us classify these data into $H_w$ bins. In Figure 66 the histogram of wave height values during operation of the Mutriku plant is shown. The distribution is now more akin to the expected (as was for both regimes in MARMOK-A-5), one of log-normal type. After separating into the same bins as for the previous analysis ($H_w < 1$, $1 \leq H_w < 2$, and $H_w > 2$) we end up with 14476, 20293 and 2562 samples, respectively.

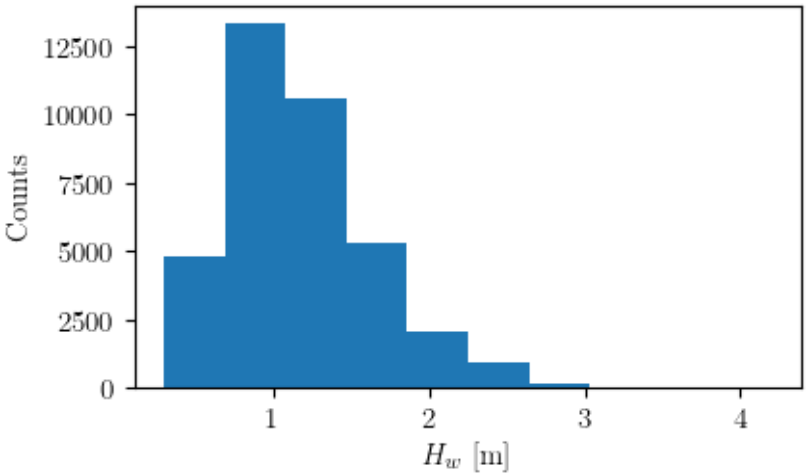


Figure 66. $H_w$ histogram for non-background signals for Mutriku.

Averaging the SPL vectors classified in such bins give the results shown in Figure 67. There is a slight increase in the sound pressure level values for higher values of wave height, although there is also overlap between their respective deviations. The

behaviour at the highest frequencies is the same as for the off state, with close to no difference between different $H_w$ bins. There seems to be no noticeable relevant signature of the Mutriku converter. The peak around 100 Hz that characterized the results of the off state (Figure 56) is now absent, further ensuring that it was caused by some uncommon energetic event (probably heavy vessel traffic).

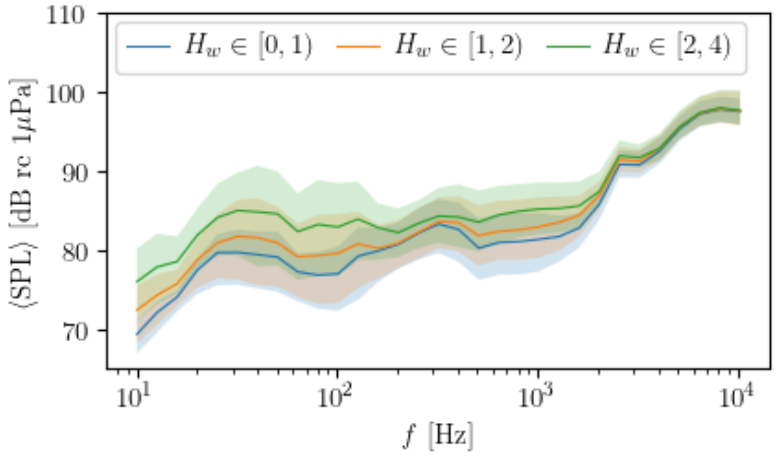


Figure 67. Mean SPL values for background signals classified in wave height bins in Mutriku. Deviations defined by Q1(percentile 25) and Q2 (percentile 75) are added as shaded bands.

The percentile distributions classified in these bins shown in Figure 68 are very similar to each other. Again, the high end of the spectrum exhibits the same behaviour, being essentially independent of wave height. Median and mean values are not so comparable as for the case of MARMOK-A-5, with the mean being a little higher than the median up to 1 kHz; in any case, they are mostly the same for every bin. As for the other percentiles, they get slightly spread out as $H_w$ increases.

- SPL dependence with respect to other parameters:

At last, we further explore the relation of SPL to other parameters, such as power. But first, without binning in $H_w$, Figure 69 and Figure 70 show this parameter with colour as scatter plot and an interpolated grid plot.

The prevalence of low wave heights is clear, as well as the slight independence of SPL with $H_w$ (except for the lowest frequencies, where most of high values of $H_w$ concentrate).

In the Figure 71 average SPL is shown as a function of wave height, thus now displayed in the horizontal axis, for some selected octave bands. As explained before, there is no clear dependence of the average SPL on $H_w$ except for the lowest frequencies. Higher values of sound pressure levels correspond to higher frequencies, as was the case in the off regime (Figure 60).

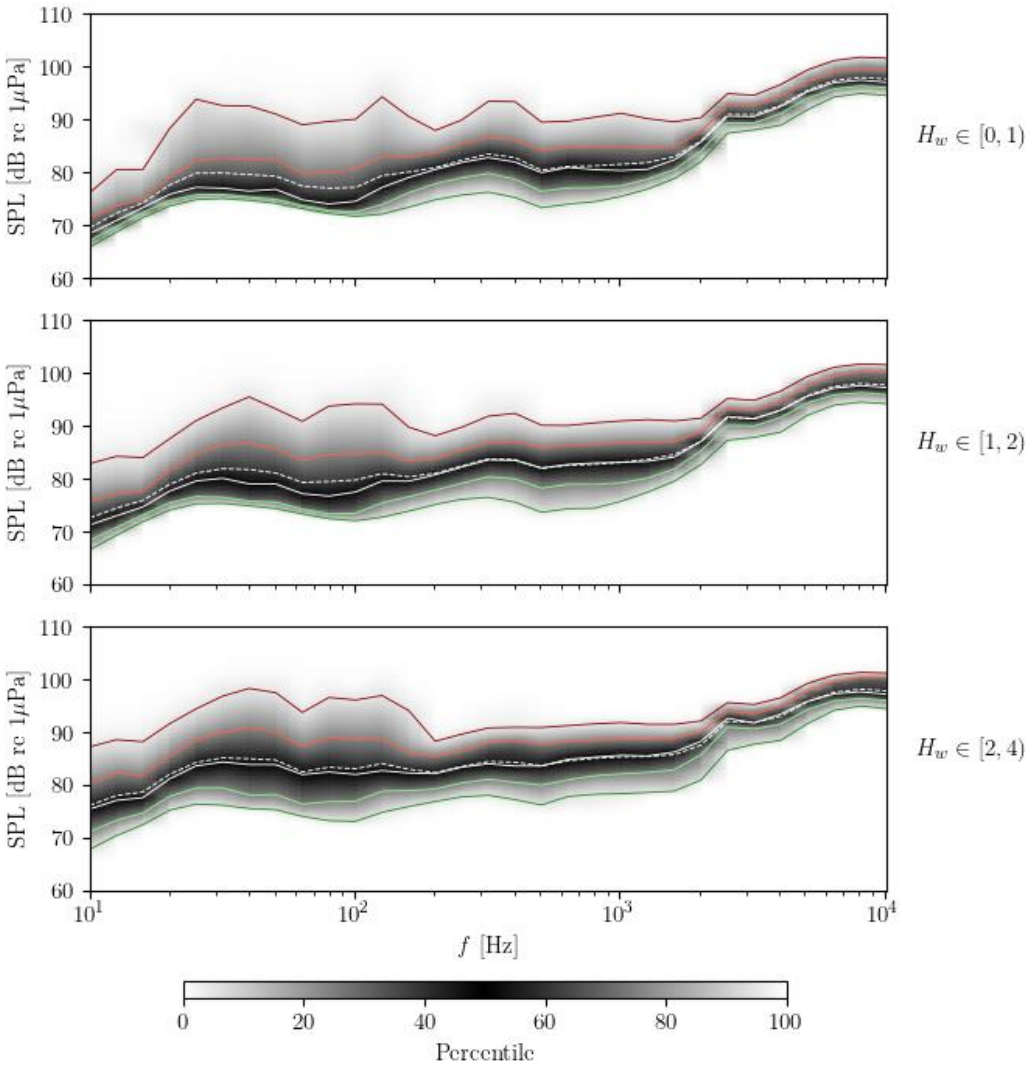


Figure 68. Percentile distribution as a colour graph for non-background noise classified by wave height, for Mutriku. In red (darker) $SPL_{95}$; (lighter) $SPL_{75}$. In green (darker) $SPL_5$; (lighter) $SPL_{25}$. In white (solid) the median $SPL_{50}$; (dashed) mean SPL.

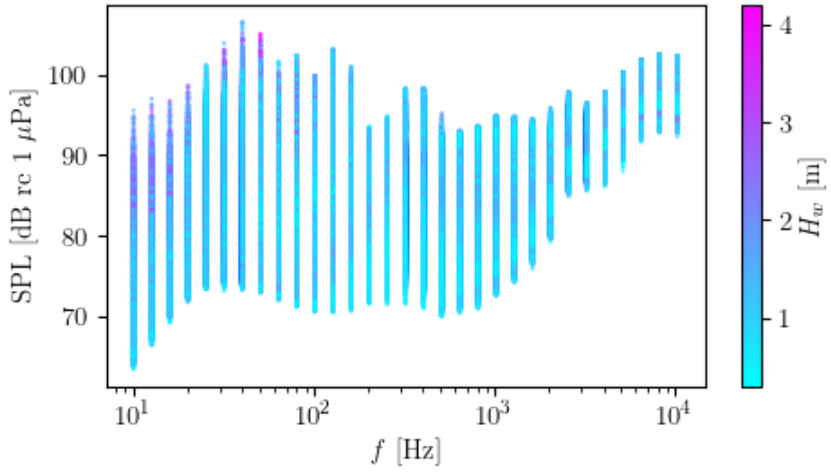


Figure 69. Scatter plot of SPL coloured by respective $H_w$ for non-background noise in Mutriku.

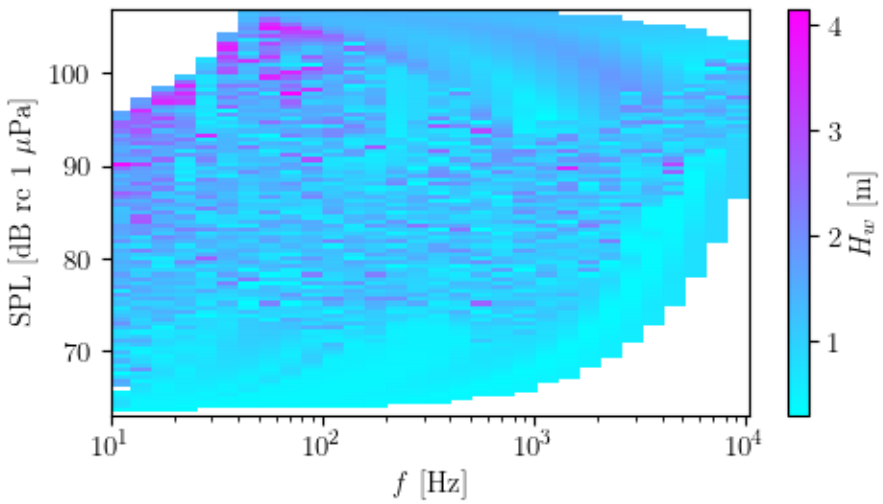


Figure 70. Interpolated grid plot of SPL($f$) with $H_w$ in colour for non-background signals in Mutriku.

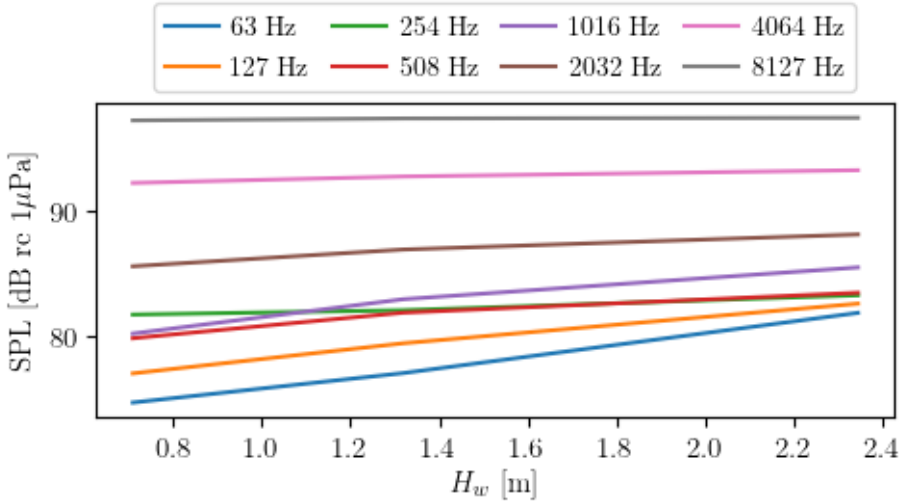


Figure 71. SPL($H_w$) for some frequency octave bands for non-background signals for MARMOK-A-5.

In Figure 72 the same behaviour is portrayed: excepting some outliers, there is a clear dependence of SPL on frequency. The distribution of wave height values for this case can also be visualized quite nicely.

Regarding the relation of sound pressure level with power output, we see in Figure 73 a scatter plot relating SPL and $P_T$ (total power output, in absolute value). Most values gather around 0 and 20 kW, with a mean value of 0.8 kW. Again, the dependence of sound pressure level on frequency is noticeable.

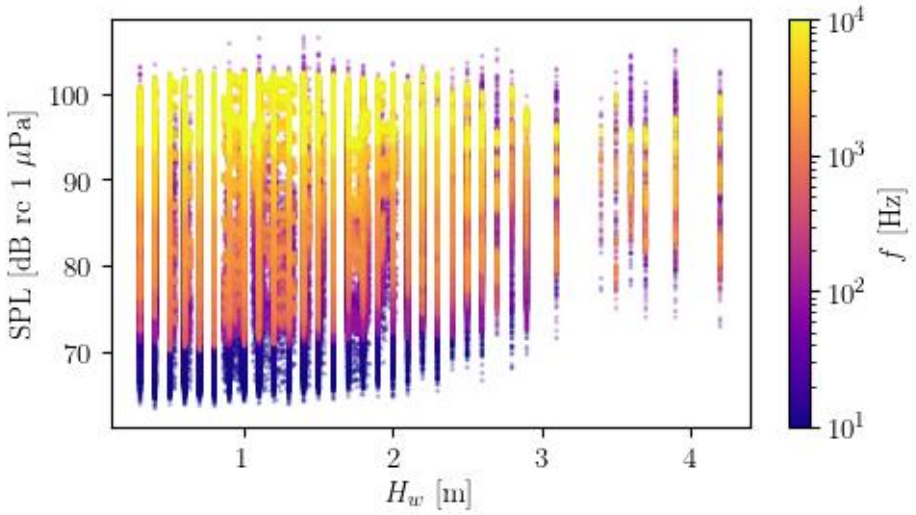


Figure 72. Scatter plot of SPL and $H_w$, coloured by frequency, for non-background signals for Mutriku.

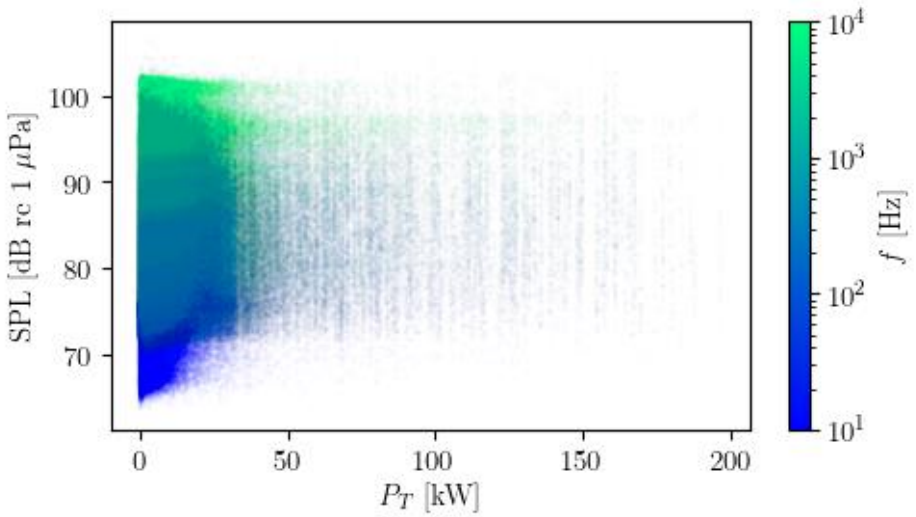


Figure 73. Scatter plot of SPL and total power (absolute value) of the Mutriku plant, coloured by frequency, for the on-regime.

Finally, Pearson correlation coefficients between SPL and $H_w$, total angular velocity (sum for all turbines) $\Omega_T$ and total power ($P_T$) in absolute value are calculated for this case and shown in Figure 74; from them we deduce there is basically no correlation at all, as their absolute maxima lie between 0.44 and 0.32, respectively, at 10 Hz. In more detail, in Figure 755 the scatter plots of SPL and $|P_T|$ for the frequencies for which $R_{\mathrm{SPL},P_T}$ has extreme values (0.32 -maximum- at 10 Hz and -0.02 -minimum- at 10240 Hz).

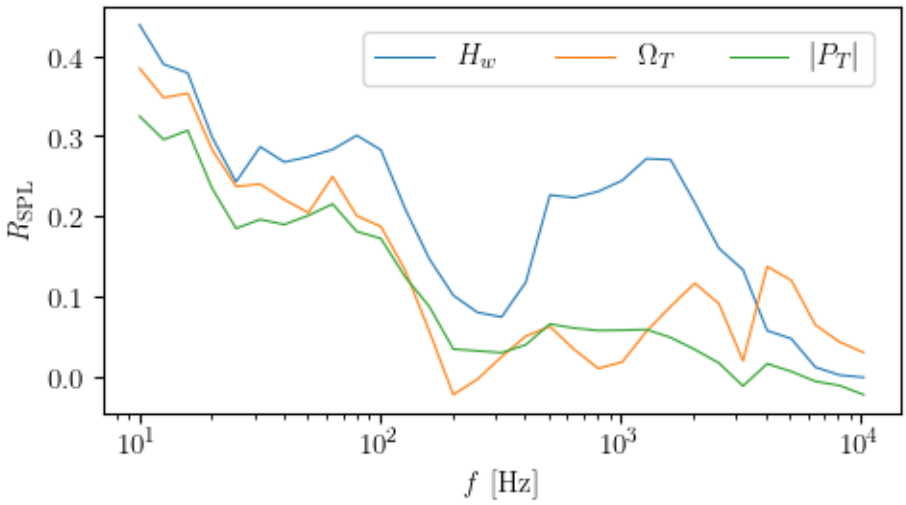


**Figure 74.** Pearson correlation coefficients between SPL and $H_w$, $\Omega_T$ and $|P_T|$ respectively, for non-background signals, for Mutriku.

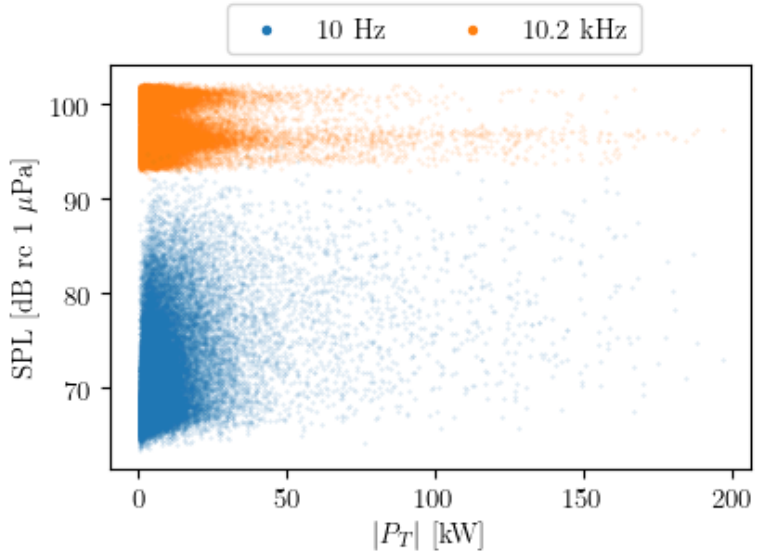


**Figure 75.** Scatter plot of SPL and total power (absolute value) for the two frequencies in which Pearson correlation coefficients are highest (10 Hz) and lowest (10.2 kHz).

### *6.2.2.3 Conclusions*

In Figure 76 the difference in sound pressure level between on and off regimes is shown, for every considered wave height bin, is shown. As expected from the earlier results, there is no clear indication of an increase in the sound pressure levels when the plant is operating. In fact, there is even a decrease in the intermediate wave height bin, particularly around 100 Hz; for the other wave height bins, the difference is positive in these very frequencies. Considering the uncertainties under which these

quantities are subject[9], we reckon there is not significative noise generated by the functioning of the plant at (at least) a distance of 1000 m.

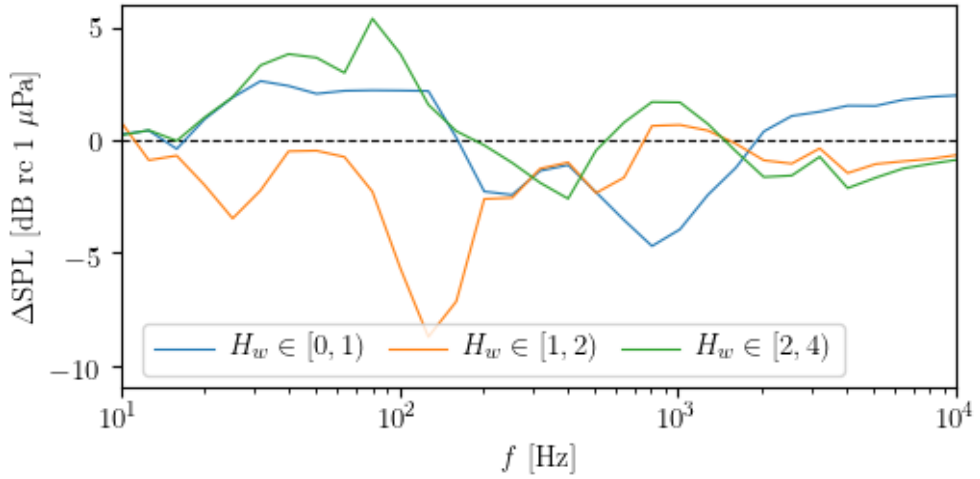


**Figure 76.** Difference between $\mathrm{SPL_{on}}$ and $\mathrm{SPL_{off}}$ for every $H_w$ bin for Mutriku.

In the Tables 13, 14 and 15, the exact results (difference of the average value, as well as standard deviation of the difference) are expressed for every frequency and wave height bin; the row in which the highest difference (in absolute value) is found is highlighted in bold font.

**Table 13.** SPL differences between on and off states for Mutriku for $H_w \in [0,1)$ m.

| Frequency [Hz] | Δ⟨SPL⟩ [dB re 1 µPa] | $\delta$SPL [dB re 1 µPa] | Frequency [Hz] | Δ⟨SPL⟩ [dB re 1 µPa] | $\delta$SPL [dB re 1 µPa] |
|---|---|---|---|---|---|
| 10 | 0.25 | 8.54 | 403 | -1.11 | 8.72 |
| 13 | 0.42 | 7.85 | 508 | -2.32 | 8.27 |
| 16 | -0.4 | 6.17 | 640 | -3.55 | 8.24 |
| 20 | 0.93 | 7.72 | **806** | **-4.7** | **8.7** |
| 25 | 1.89 | 8.95 | 1016 | -3.96 | 8.51 |
| 32 | 2.62 | 8.41 | 1280 | -2.43 | 7.88 |
| 40 | 2.4 | 8.74 | 1613 | -1.23 | 6.54 |
| 50 | 2.05 | 8.5 | 2032 | 0.38 | 4.77 |
| 63 | 2.18 | 7.8 | 2560 | 1.07 | 3.65 |
| 80 | 2.21 | 9.34 | 3225 | 1.26 | 3.06 |
| 101 | 2.19 | 9.33 | 4064 | 1.52 | 3.48 |
| 127 | 2.17 | 10.64 | 5120 | 1.51 | 3.28 |
| 160 | 0.11 | 9.53 | 6451 | 1.79 | 3.12 |
| 202 | -2.28 | 8.8 | 8127 | 1.92 | 3.11 |
| 254 | -2.43 | 9.33 | 10240 | 1.98 | 3.15 |
| 320 | -1.37 | 9.14 | | | |

[9] Not shown here for visibility reasons. See instead Figure 56 and 67.

Table 14. SPL differences between on and off states for Mutriku for $H_w \in [1,2)$ m.

| Frequency [Hz] | $\Delta\langle$SPL$\rangle$ [dB re 1 µPa] | $\delta$SPL [dB re 1 µPa] | Frequency [Hz] | $\Delta\langle$SPL$\rangle$ [dB re 1 µPa] | $\delta$SPL [dB re 1 µPa] |
|---|---|---|---|---|---|
| 10 | 0.82 | 8.92 | 403 | -0.99 | 10.0 |
| 13 | -0.89 | 8.96 | 508 | -2.35 | 9.87 |
| 16 | -0.69 | 7.31 | 640 | -1.67 | 9.36 |
| 20 | -2.0 | 9.61 | 806 | 0.63 | 8.93 |
| 25 | -3.48 | 12.66 | 1016 | 0.67 | 8.72 |
| 32 | -2.23 | 13.53 | 1280 | 0.42 | 7.91 |
| 40 | -0.5 | 13.32 | 1613 | -0.16 | 6.49 |
| 50 | -0.47 | 12.17 | 2032 | -0.9 | 4.84 |
| 63 | -0.75 | 11.55 | 2560 | -1.05 | 4.24 |
| 80 | -2.29 | 15.36 | 3225 | -0.37 | 3.99 |
| 101 | -5.69 | 18.49 | 4064 | -1.46 | 4.11 |
| **127** | **-8.73** | **19.08** | 5120 | -1.07 | 4.04 |
| 160 | -7.16 | 14.63 | 6451 | -0.94 | 4.12 |
| 202 | -2.61 | 9.16 | 8127 | -0.83 | 4.22 |
| 254 | -2.56 | 9.13 | 10240 | -0.65 | 4.37 |
| 320 | -1.27 | 9.18 | | | |

Table 15. SPL differences between on and off states for Mutriku for $H_w \in [2,5)$ m.

| Frequency [Hz] | $\Delta\langle$SPL$\rangle$ [dB re 1 µPa] | $\delta$SPL [dB re 1 µPa] | Frequency [Hz] | $\Delta\langle$SPL$\rangle$ [dB re 1 µPa] | $\delta$SPL [dB re 1 µPa] |
|---|---|---|---|---|---|
| 10 | 0.21 | 11.08 | 403 | -2.6 | 11.14 |
| 13 | 0.44 | 10.25 | 508 | -0.46 | 10.95 |
| 16 | -0.04 | 9.01 | 640 | 0.78 | 10.25 |
| 20 | 1.01 | 9.15 | 806 | 1.69 | 9.8 |
| 25 | 1.9 | 10.3 | 1016 | 1.67 | 9.34 |
| 32 | 3.31 | 11.04 | 1280 | 0.71 | 8.4 |
| 40 | 3.81 | 11.93 | 1613 | -0.5 | 7.45 |
| 50 | 3.65 | 11.64 | 2032 | -1.64 | 5.6 |
| 63 | 2.98 | 10.91 | 2560 | -1.58 | 4.62 |
| **80** | **5.38** | **11.89** | 3225 | -0.74 | 4.27 |
| 101 | 3.82 | 12.7 | 4064 | -2.13 | 4.52 |
| 127 | 1.57 | 13.56 | 5120 | -1.67 | 4.51 |
| 160 | 0.4 | 10.96 | 6451 | -1.26 | 4.48 |
| 202 | -0.23 | 8.93 | 8127 | -1.05 | 4.61 |
| 254 | -1.01 | 8.98 | 10240 | -0.86 | 4.89 |
| 320 | -1.9 | 9.95 | | | |

## 6.3 Spatial analysis

The aim of this analysis is to spatially characterize the noise registered in the surroundings of the converters. This first study can be seen as an introduction to the task 3.2 (Acoustic Modelling), in which the SPL field around the converters will be simulated in much more detail.

### 6.3.1 MARMOK-A-5

Given that only meaningful results were obtained in the first day of the spatial monitoring campaign, as in the second day only some recordings were taken (recall section 4.1.4.1), in the next subsection the interpolated maps of SPL are presented.

In the Figures 77, 78 and 79, the empirical noise maps, obtained by direct interpolation of the processed acoustic data, are shown for frequencies from 15 Hz to 8 kHz. Note that the higher levels are found in the lowest frequencies (up to 49 Hz).

On the other hand, in Figure 80, average SPL from these interpolated sound maps have been calculated in concentric annuli of increasing radii (centred in the source) to obtain the explicit dependence of sound pressure levels on distance from the converter.

As was expected from the precedent results, there is a great gap between levels between the lowest frequencies and those of the rest of the spectrum.

#### *6.3.1.1 Conclusions*

The spatial acoustic monitoring in BiMEP gave very high SPL values reaching 150 dB re 1 μPa for the frequencies between 31 and 49 Hz. From these frequencies, levels decrease as we approach the end of the considered spectrum, getting values around 95 dB re 1 μPa. But even if the sea state in Beaufort scale was of 7 (recall 15), some unwanted noise (vessel motor, water splashing, etc.) must have been added to the signals in order to reach these levels. The dependence of sound levels with respect the distance is not very clear, but it shows some decrease, specially from 700 m and beyond, and for higher frequencies.

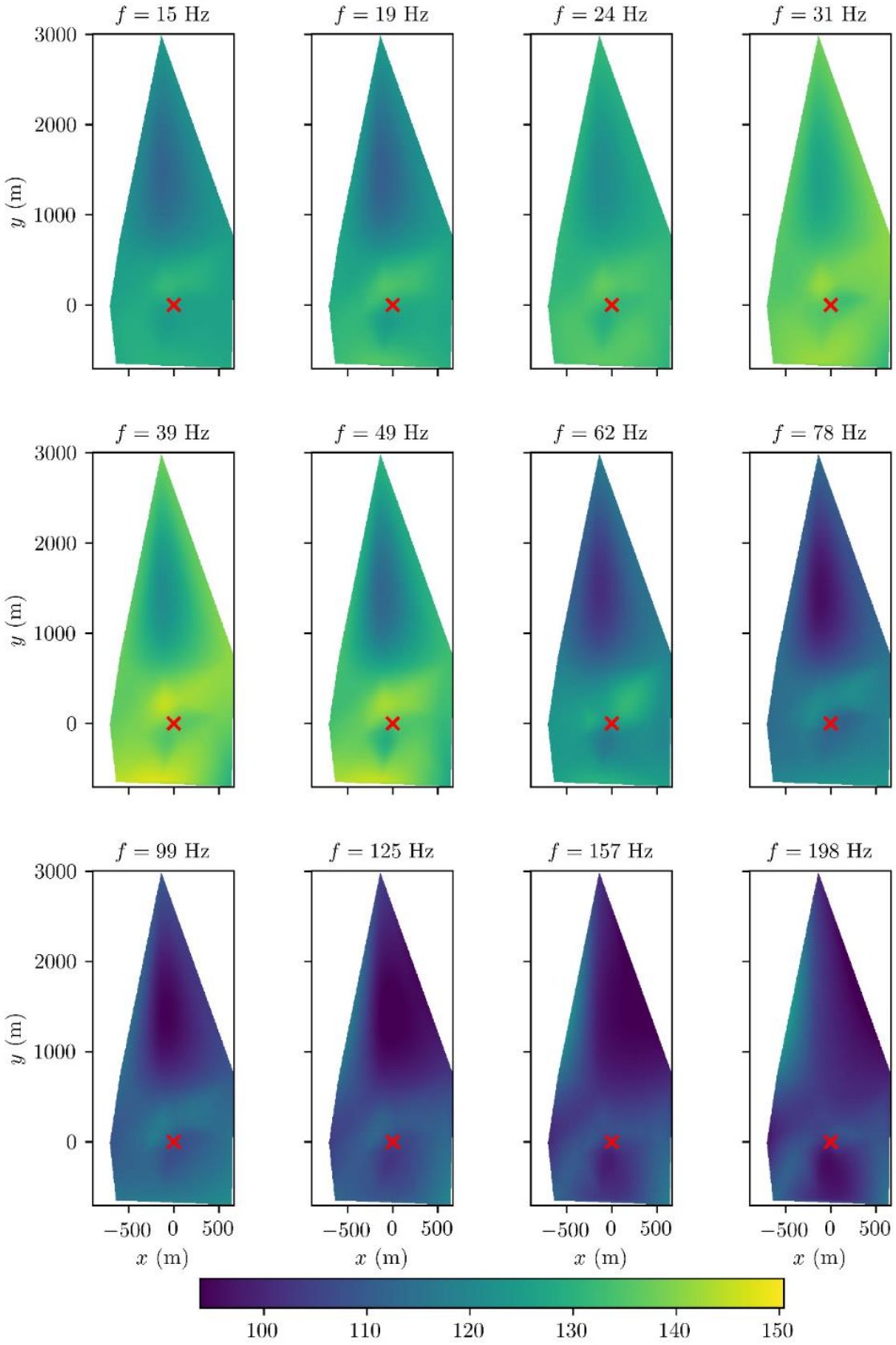


Figure 77. Maps from recordings made in the 06-05-2019. Device location is marked as a red cross.

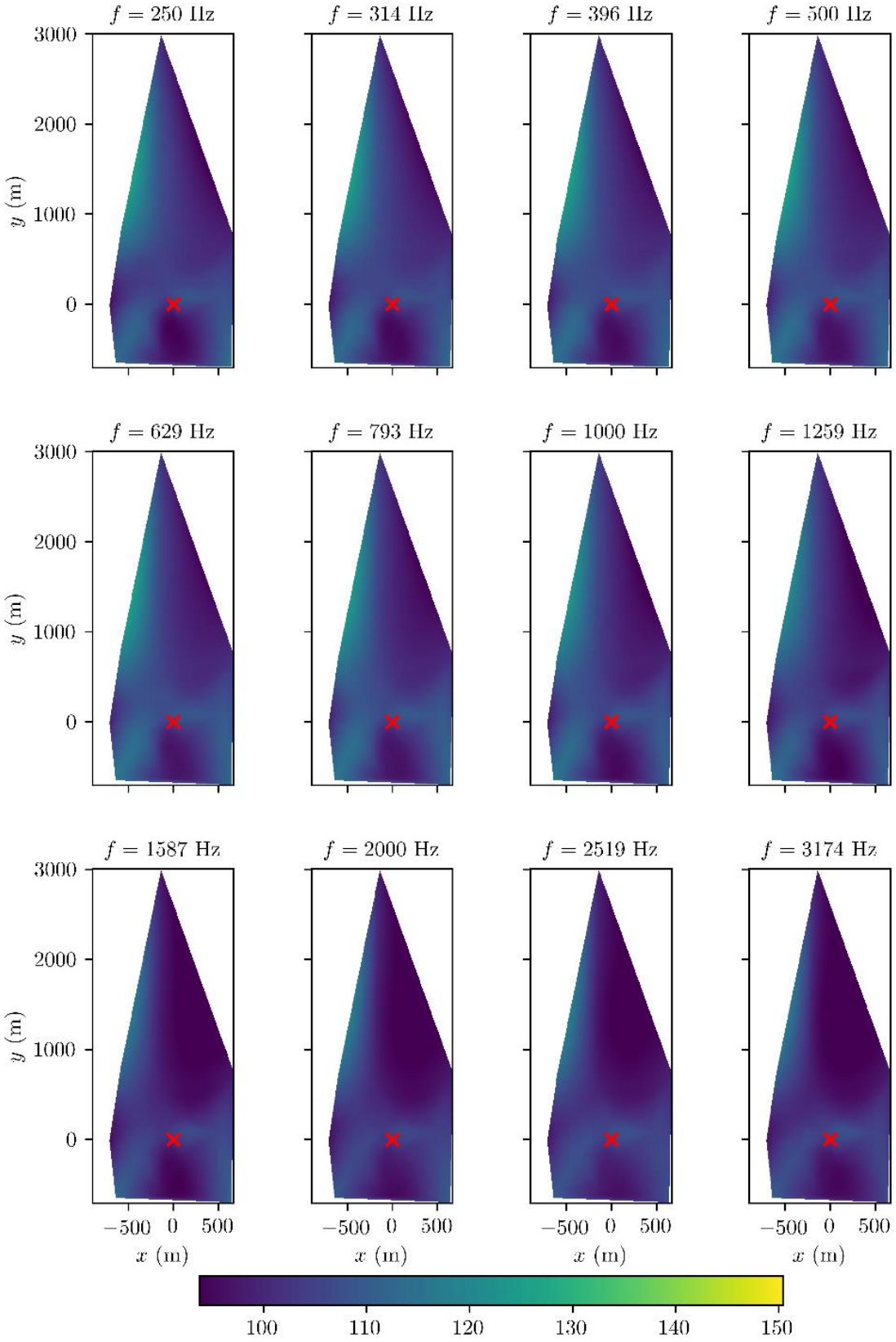


Figure 78. Maps from recordings made in the 06-05-2019 for frequencies from 250 to 3174 Hz.

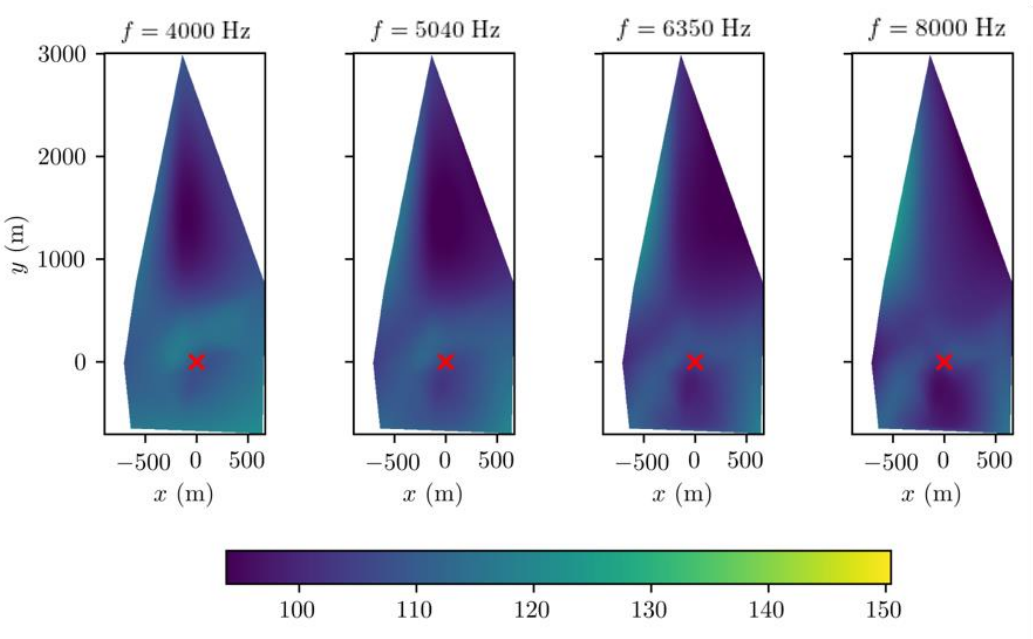


Figure 79. Last set of frequencies for the maps made from the recordings in 06-05-2019.

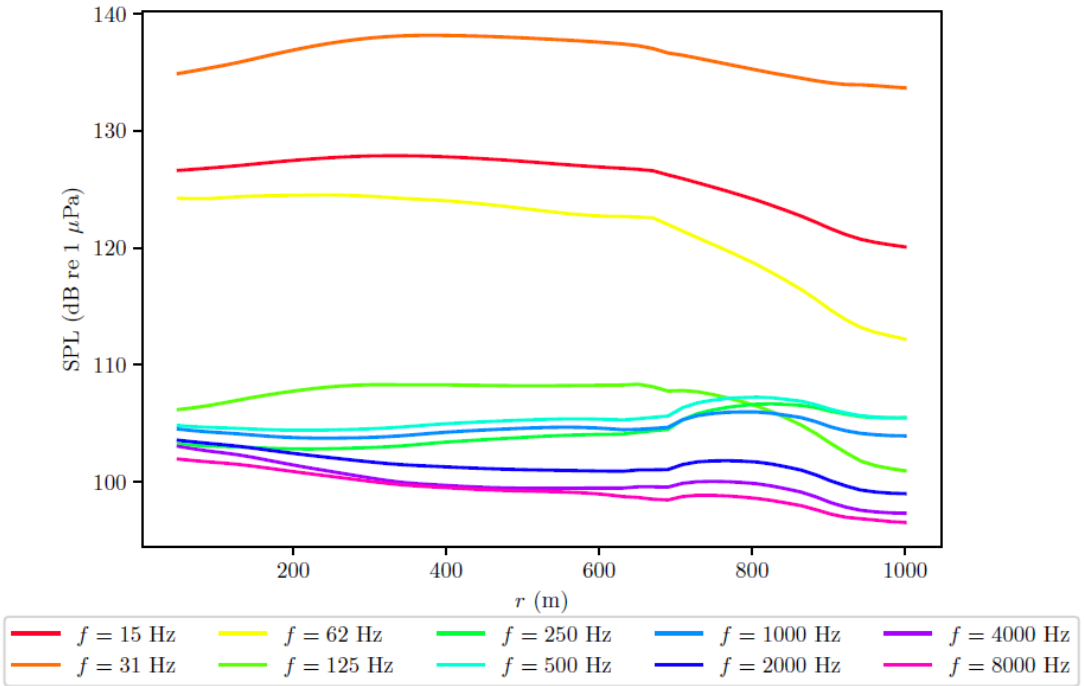


Figure 80. Average SPL in concentric annuli of increasing radii for MARMOK-A-5 for the bands of frequency centred in the octaves between 15 and 8000 Hz.

### 6.3.2 Mutriku

Proceeding in the same way as for MARMOK-A-5, we obtain the following figures for the spatial monitoring campaign carried out in Mutriku the 7th of May of 2019. In them, empirical noise maps, obtained by direct interpolation of the processed acoustic data, are shown for frequencies from 15 Hz to 8 kHz. Note that the higher levels are concentrated in the frequencies ranging from 31 to 49 Hz.

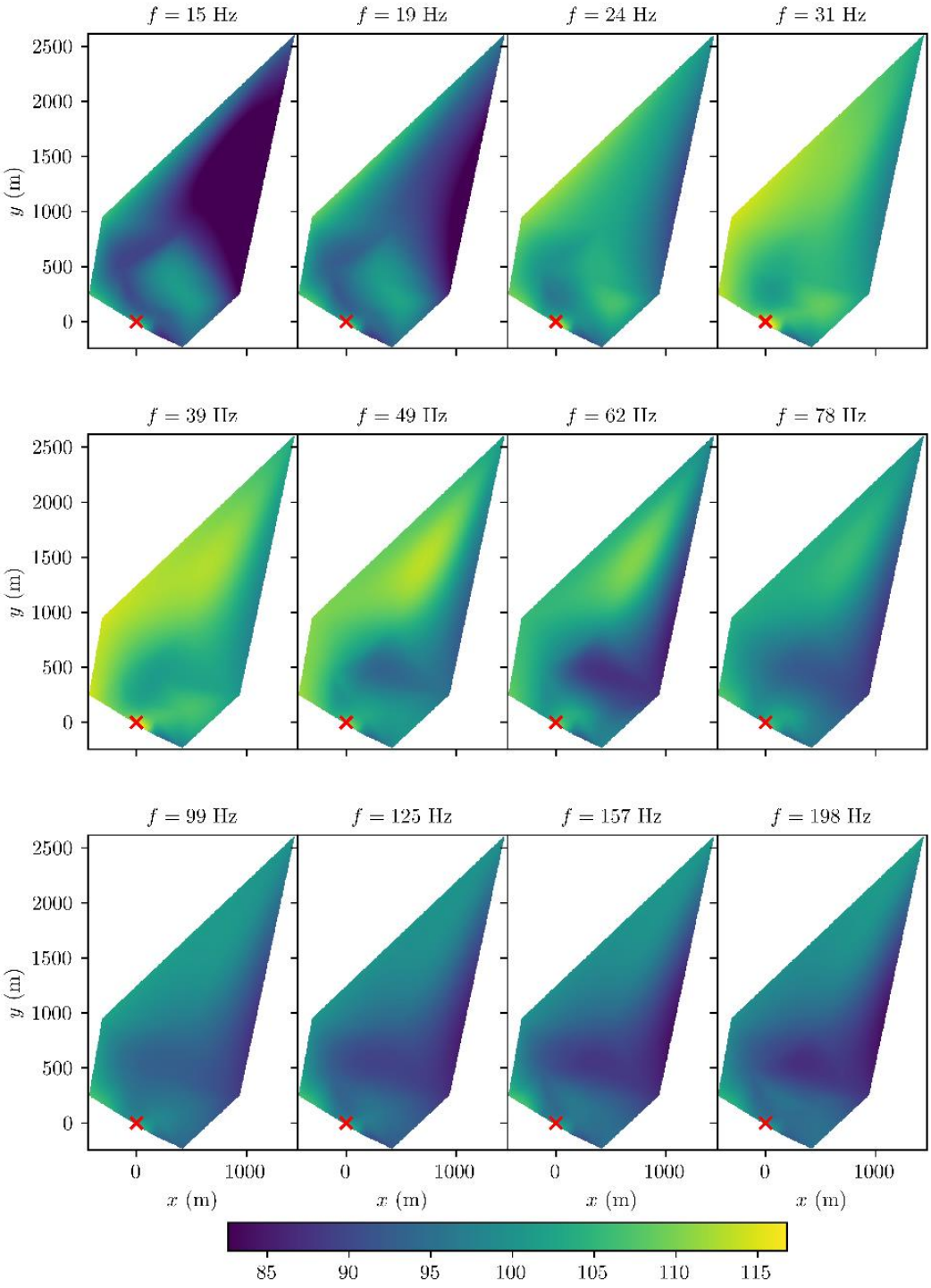


Figure 81. Maps from recordings made in the 07-05-2019. Device location is marked as a red cross.

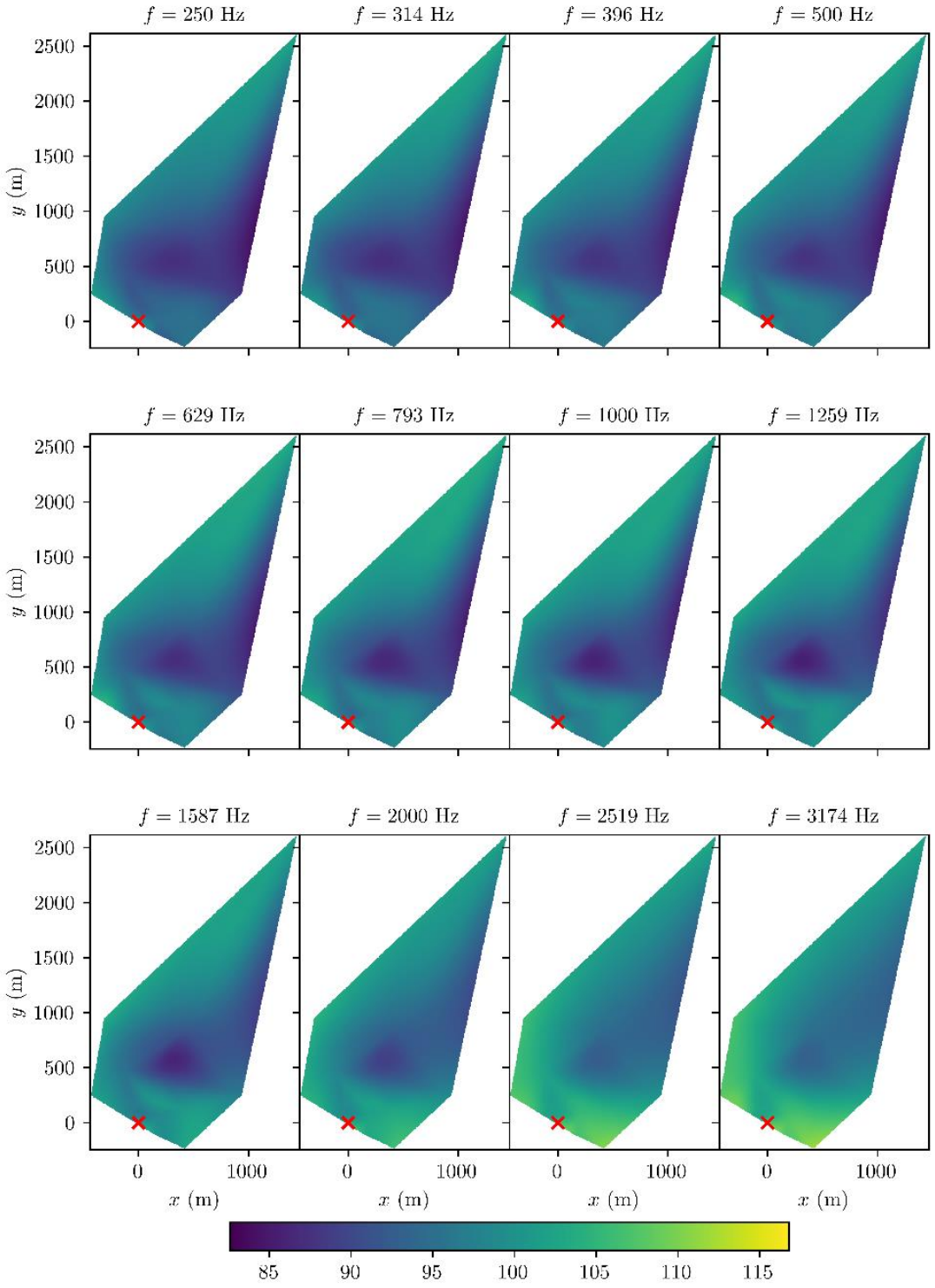


Figure 82. Maps from recordings made in the 07-05-2019 for frequencies from 250 to 3174 Hz.

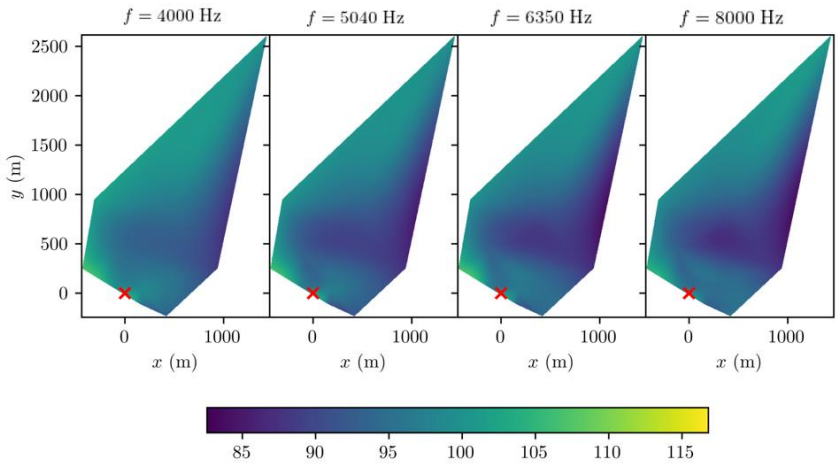


**Figure 83.** Last set of frequencies for the maps made from the recordings in 07-05-2019.

We also calculate the dependence of sound pressure levels on distance from the converter by taking concentric semi-annuli (since Mutriku is onshore) of increasing radio centred on the middle of the Mutriku power plant and calculating the average SPL inside those annuli. The result is shown in Figure 84.

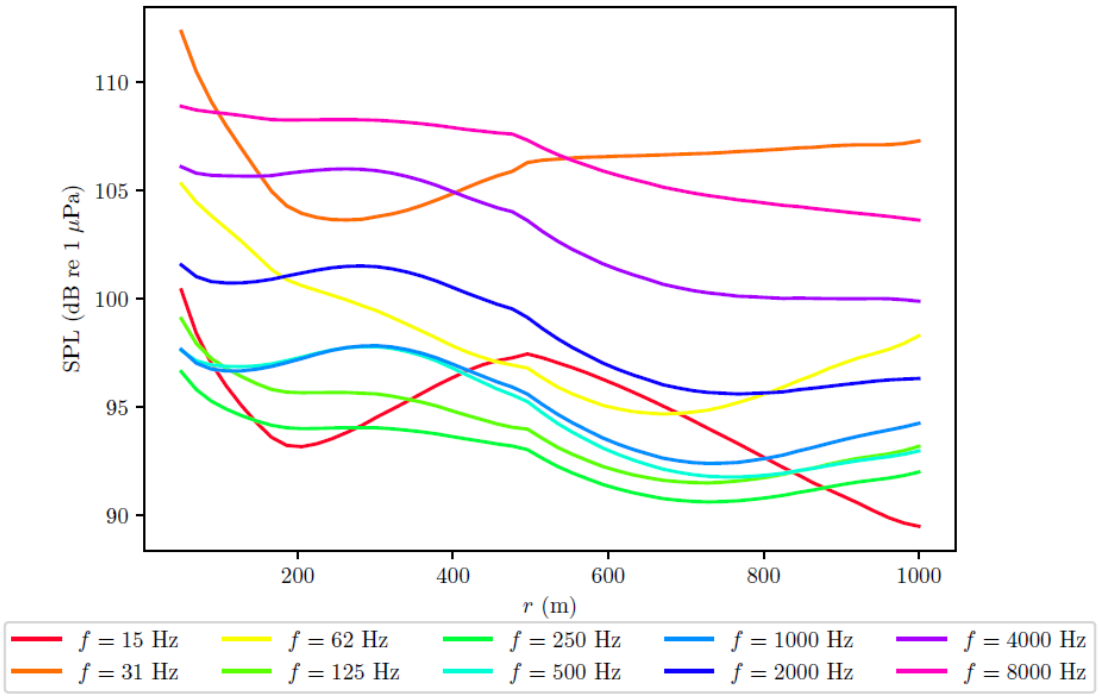


**Figure 84.** Average SPL in concentric annuli of increasing radii for MARMOK-A-5 for the bands of frequency centred in the octaves between 15 and 8000 Hz.

#### 6.3.2.1 Conclusions

For Mutriku, since the conditions were much calmer (recall Table 6), the sound pressure levels were much lower than for MARMOK-A-5, having the maxima (around 115 dB re 1 μPa) in the same frequencies as before. There is not a clear radial dependence of SPL from the power plant as seen from the interpolated maps, even though the curves of Figure 84 show some decrease in the spatially averaged values of this variable, most striking at the higher frequencies (almost monotonically decreasing).

## 6.4 Airborne measurements

### 6.4.1 Mutriku

It should be noted that the wave height for each measurement is shorter than 1m, specifically, wave height is 0.4m. Then, all airborne acoustic measurement were done under good and same weather conditions.

In this sense, the SPL of the acoustic measurements of Mutriku in the second day of campaign is shown in Figure 85.

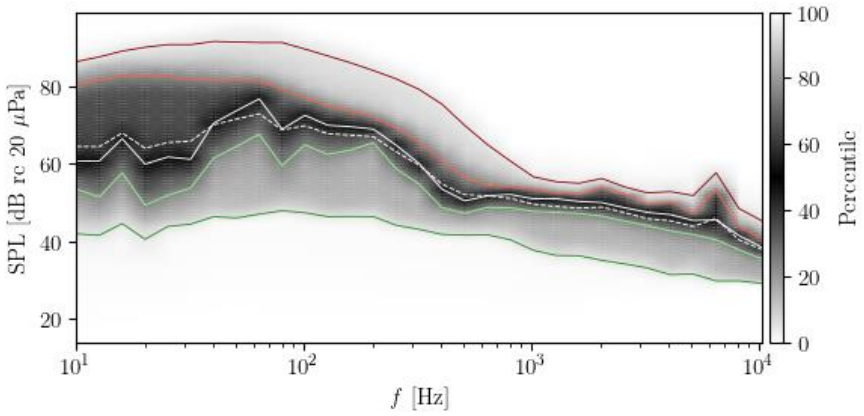


**Figure 85.** Percentile distribution as a colour graph for airborne noise for the overall turbine power in Mutriku. In red (darker) SPL95; (lighter) SPL75. In green (darker) SPL5; (lighter) SPL25. In white (solid) the median SPL50; (dashed) mean SPL.

In addition, in the following figure, the FFT is presented (Figure 86).

Considering different overall turbine power, the airborne noise level is shown in the Figure 87. In this figure, it can be appreciated that for lower frequencies, percentiles present higher differences than for higher frequencies, where the distance between them are narrower. Specially for power between 0 to 1 and 2 to 5 kW.

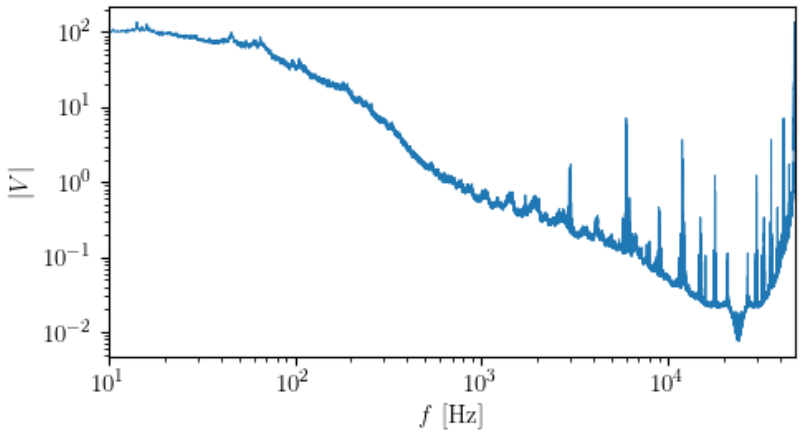


Figure 86. FFT of the airborne noise for the overall turbine power in Mutriku.

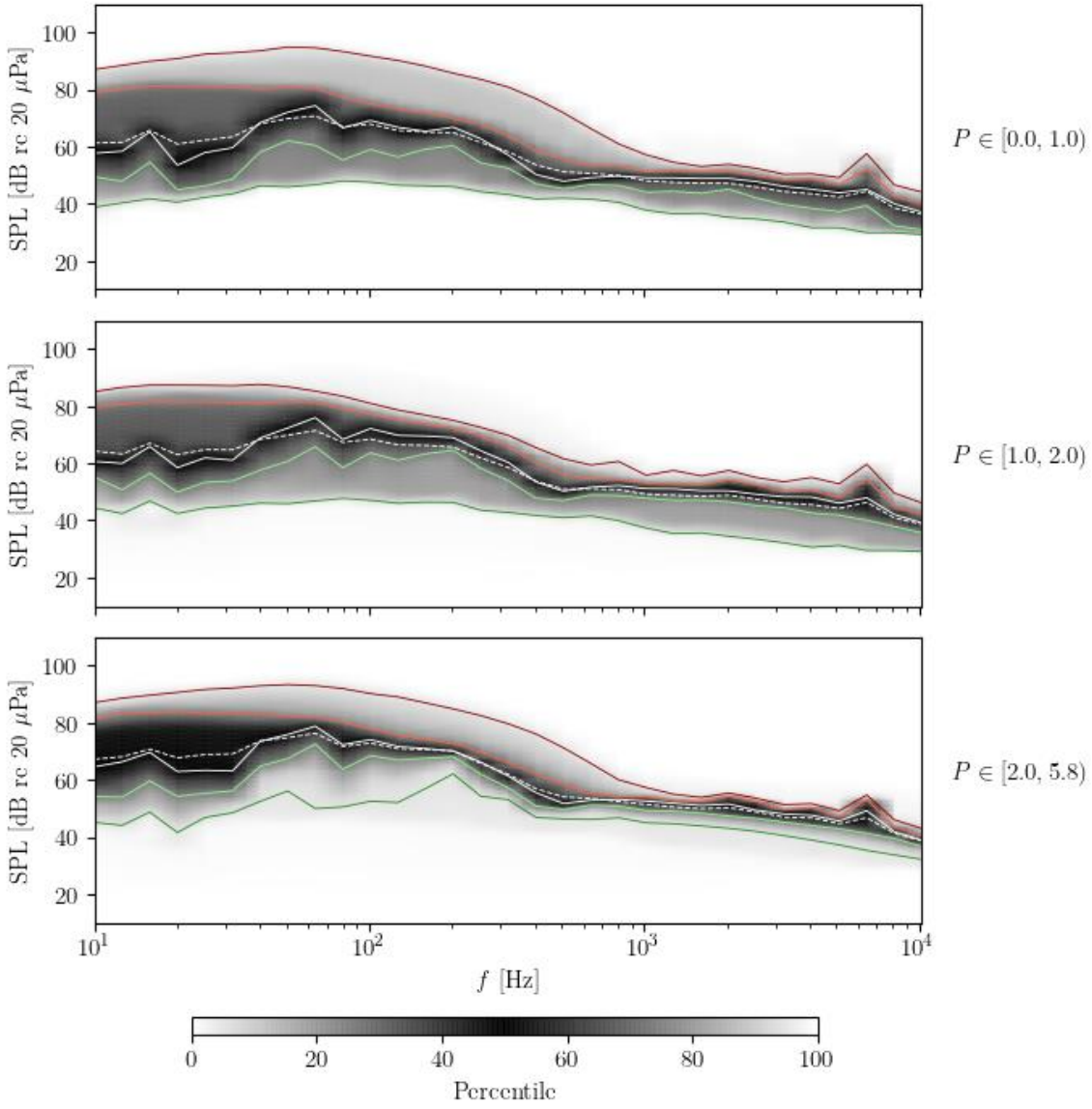


Figure 87. Percentile distribution as a colour graph for airborne noise classified by power [kW], for Mutriku. In red (darker) $SPL_{95}$; (lighter) $SPL_{75}$. In green (darker) $SPL_5$; (lighter) $SPL_{25}$. In white (solid) the median $SPL_{50}$; (dashed) mean SPL.

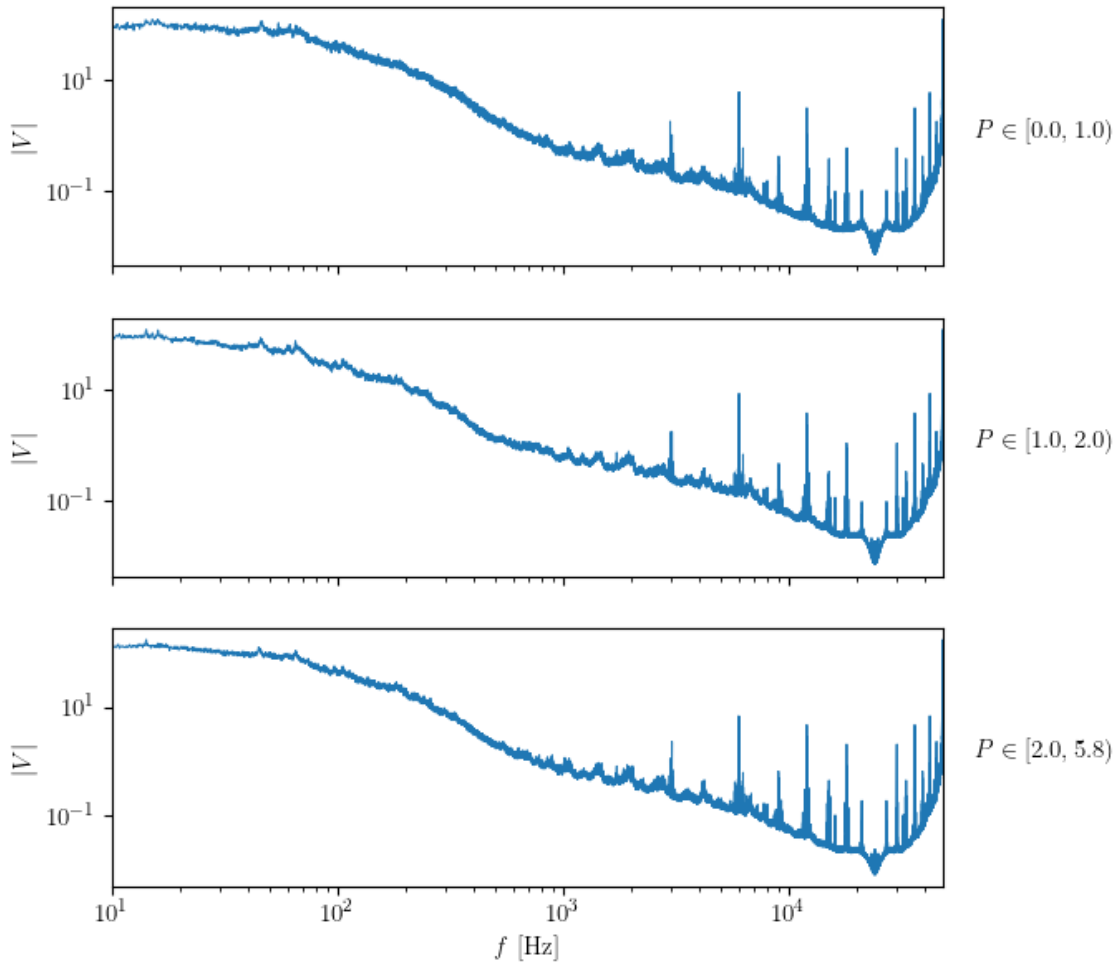


Figure 88. FFT of the airborne noise classified by power.

# 7. Conclusions

Lastly, here we shall remark the fundamental results deduced from the work undertaken in this task, as well as some comments on further improvements and lessons learnt.

First of all, we should recall the high variability of sound pressure levels in all cases, reflected on the relatively high uncertainties regarding results. With this in mind, the acoustic disturbance produced by the devices was, at most, of little magnitude.

Another consideration which should be accounted for following projects is the importance of adequate sampling of underwater noise in different (combinations of) sea conditions and operating conditions. This is a crucial point, as there must be a minimum of samples in each scenario to extract insightful metrics.

Concerning the acquisition of audio recordings, the sampling frequency of the measuring system should be adjusted depending on the spectra considered in the posterior processing. This consideration would improve the monitoring time interval and reduce the otherwise hefty storage requirements, just as lighten the computational demands on the processing.

## 7.1 MARMOK-A-5

### 7.1.1 Temporal monitorization

This device shows the clearest acoustic signature of all converters of this study, an effect probably boosted by the short distance between it and the fixed hydrophone.

Conclusion remarks:

- The higher levels correspond to the noise of the mooring chains beyond 2500 Hz.
- With the device off, avoiding the noise of chains, there are SPL between 90 and 102 dB re 1 $\mu$Pa, increasing with the height of the sea waves.
- With the device on, SPL peaks appears between 40 and 120 Hz with increments between device on respect to device off of: $+14$ dB ($H_w < 1$ m), $+13$ dB ($1\ \mathrm{m} \leq H_w < 2\ \mathrm{m}$) and $+6$ dB ($2\ \mathrm{m} \leq H_w < 5\ \mathrm{m}$).

### 7.1.2 Spatial monitorization

As to the spatial monitoring campaign, the results obtained from the sampling carried out the 06-05-2019 show a slight dependence on radial distance from the converter, especially for the lower frequencies (ranging from 15 to 63 Hz), and from 700 meters and beyond. The values themselves are quite high, reaching 150 dB re 1 µPa for the band centred in 30 Hz. On the other hand, sound levels decrease as we approach the

end of the considered spectrum, with values around 95 dB re 1 μPa. With all, sound pressure levels decrease up to 5 dB re 1 μPa in 1000 m.

These values will be contrasted with the results of underwater acoustic propagation models, which will be seen in deliverable D.3.2.

## 7.2 Mutriku

### 7.2.1 Temporal monitorization

The analysis for this case shows no significant noise emission from the power plant. As opposed to the MARMOK-A-5 scenario, the larger distance between the power plant and the hydrophone in this case is one possible reason of this fact. In any way, the results indicate that, (at least) at the location of the fixed hydrophone, there is no distinguishable noise signature from the power plant, when the involved uncertainties are considered.

Conclusion remarks:

- With the device off, there is an anomaly, as in SPL increases below 200 Hz for $1\ \mathrm{m} \leq H_w < 2\ \mathrm{m}$ with respect to device-on regime corresponding values.
- With the device on, SPL increase up to 5 dB below 200 Hz.

### 7.2.2 Spatial monitorization

The analysis for the spatial campaign data does not seem to reveal any significant noise emission coming from the power plant, except perhaps for the bands centred in the higher frequencies. Sound pressure levels are lower than those corresponding to the MARMOK-A-5 scenario, in accordance with the calmer sea state, having a maximum not higher than 115 dB re 1 μPa. In agreement with the results of the temporal monitorization, the end part of the spectrum is where higher values of SPL are found. In any case, the difference between near field and far field SPL values is not higher than 10 dB re 1 μPa.

In subsequent deliverables, specifically in D.3.2, this acoustic spatial issue will be further developed, considering the implementation of underwater noise propagation models.

# 8. Bibliography

Bald, J., Uriarte, A., Ruiz, P., Cervantes, P., & Ortega, N. (2017). Acoustic characterization of Mutriku OWC Plant. *III Marine Energy Week*. Bilbao.

Boehlert, G. W., & Gill, A. B. (2010). Environmental and ecological effects of ocean renewable energy development - A current synthesis. *Oceanography*, 68-81.

Khan, N., Kalair, A., Abas, N., & Haider, A. (2017). Review of ocean tidal, wave and thermal energy technologies. *Renewable and Sustainable Energy Reviews*, 590-604.

Melikoglu, M. (2018). Current status and future of ocean energy sources: a global review. *Ocean Engineering*, 563-573.

Urick, R. J. (1983). *Principles of underwater sound*. McGraw-Hill.

Weilgart, L. S. (2007). The impacts of anthropogenic ocean noise on cetaceans and implications for management. *Canadian Journal of Zoology*, 1091-1116.

This project has been funded by the European Commission under the European Maritime and Fisheries Fund (EMFF), Call for Proposals EASME/EMFF/2017/1.2.1.1 – "Environmental monitoring of wave and tidal devices". This communication reflects only the author's view. EASME is not responsible for any use that may be made of the information it contains.